HUMAN BRAIN METABOLIC IMAGING BY ^{1}H MR SPECTROSCOPY AT 3T AND 7T: APPLICATION IN CANCERS

APPROVED BY SUPERVISORY COMMITTEE

Changho Choi, Ph.D.

Ralph Deberardinis, M.D., Ph.D.

Elizabeth Maher, M.D., Ph.D.

Matthew Merritt, Ph.D.

Jimin Ren, Ph.D.

DEDICATION

To my family and friends.

The present work would not have been possible without the support, inspiration and encouragement from a great number of people in my life and it gives me immense pleasure to thank them.

First and foremost, I would like to thank my supervisor and mentor, Dr. Changho Choi, for his continuous support, advice and patience throughout the course of my graduate studies. I am really grateful to him for giving me an opportunity to be his student and learn from him. The countless hours of productive discussions with him have taught me to look beyond the obvious, ask the important questions and confirm the results with scientific rigor. He helped me grow academically and professionally in the field of *in vivo* spectroscopy.

I wish to thank my dissertation committee members, Drs. Elizabeth Maher, Ralph DeBerardinis, Matthew Merritt and Jimin Ren for their time and patience. I also thank Sarah McNeil and Christie Sheppard, for their help in recruiting the clinical volunteers, without

whom this thesis would not have been possible. Thank you to Janet Jerrow and Jeannie Baxter for helping me in recruiting healthy volunteers. I express my sincere gratitude to the glioma patients, who participated in the MRS scans. Without their volunteering, the MRS development in this study would not have been possible.

I thank past and present students of the lab, Aditya Patel, Akshya Madan, Abhishek Banerjee, Keith Hulsey, Katherine Borner, and Sang-Young Kim, for making my time in the lab more enjoyable, productive and rewarding. A special thanks to Zhongxu An, who has provided support by taking over the day-to-day activities of the lab.

I am grateful to Drs. Dean Sherry and Craig Malloy, for creating and nurturing Advanced Imaging Research Center (AIRC), which provided the cutting edge research environment with so many exceptional scientists and students. I also like to thank Ivan Dimitrov for helping me with the scanner programming environment and troubleshooting. I would like to thank the supporting staff at AIRC, who helped me navigate administrative processes. A particular thanks to the MR technologists of the center, Rani Varghese, Salvador Pena, Debbie Douglas and Jing Yang for their patient help with the experiments and accommodating my time schedules on the scanner. Additionally, I thank Drs. Richard Briggs, Sergey Cheskov and Kaundinya Gopinath, who supported me during my first year of graduate studies.

I would like to thank all of the fellow graduate students at AIRC who were a constant source of motivation and knowledge. My gratitude to good friends: Dilip Challa, Sairam Geethanath, Sarath Chandra, and Praveen Gulaka, Virendra Mishra who made my stay here in United States so enjoyable. In particular, I would like to thank Ramraj Velmurugan, for

the lengthy discussions and unique insights on almost everything about life that helped me grow as a person more than graduate studies alone ever would have. I thank Minhui Ouyang, for the friendship and many pleasant breaks from work. Additionally, I am in debt to my best friends Praveen Dorna and Renuka Dupati, for their continued encouragement, support during the tough days and for having faith in me to finish.

I thank my parents for their unconditional love and encouragement to pursue my passion. I am grateful to my elder sister, Dr. Sandhya Kalantri, for always being there when I needed support and providing a watchful eye to guide me on the right path. Thanks to my lovely younger sister, Dr. Shwetha Ganji who always believed in me. I thank my brother-in-law, Shailendra Kalantri, who provided immense support to my family over the last six years of my absence. A special acknowledgement goes to my six-year-old nephew, Shubhan, whose innocence has been a source of vast joy for me.

HUMAN BRAIN METABOLIC IMAGING BY 1H MR SPECTROSCOPY AT 3T AND 7T: APPLICATION IN CANCERS

by

SANDEEP KUMAR GANJI

DISSERTATION / THESIS

Presented to the Faculty of the Graduate School of Biomedical Sciences

The University of Texas Southwestern Medical Center at Dallas

In Partial Fulfillment of the Requirements

For the Degree of

DOCTOR OF PHILOSOPHY

The University of Texas Southwestern Medical Center at Dallas

Dallas, Texas

December, 2014

HUMAN BRAIN METABOLIC IMAGING BY 1H MR SPECTROSCOPY AT 3T AND 7T: APPLICATION IN CANCERS

Publication No. _____

Sandeep Kumar Ganji, B.E.

The University of Texas Southwestern Medical Center at Dallas, Graduation Year

Supervising Professor: Changho Choi, Ph.D.

Proton MR spectroscopy (MRS) provides an effective tool for measuring metabolites in human brain noninvasively. Precise measurement of several clinically important metabolites such as glycine (Gly), 2-hyroxyglutarate (2HG), γ-aminobutyric acid (GABA), and glutamate (Glu) remains challenging primarily due to their relatively small signal strengths and spectral overlap with adjacent large signals. The present study aims to develop new MRS techniques for reliable imaging of these metabolites and apply in glioma patients at 3T and 7T. The transverse relaxation times (T_2) of brain metabolites are needed for absolute quantitation. As the first topic, the T_2s of metabolites in healthy brain were measured using point-resolved spectroscopy (PRESS) at 3T. The T_2s of Glu, myo-inositol, NAA-aspartate,

and N-acetyl-aspartyl-glutamate were evaluated in addition to large singlet signals. The second topic was to measure Gly in human brain with MRS imaging at 3T. An optimized PRESS TE=160 ms scheme was used to measure Gly in healthy brain and gliomas. The data indicated the presence of a regional variation of Gly in healthy brain, with estimates ~1 mM and ~0.3 mM in gray and white matter dominant regions, respectively. The Gly level was significantly increased in tumors compared to the contralateral brain. Gly elevation was more extensive with higher tumor grade. Mutations in isocitrate dehydrogenase (IDH) 1 and 2 result in production of 2HG and as a result, 2HG is elevated by orders of magnitude in IDH-mutated gliomas. As the third topic, 2HG was estimated in subjects with IDH-mutated gliomas using MRS imaging. PRESS TE=97 ms and 78 ms were used for detection of 2HG at 3T and 7T, respectively. The reproducibility of 2HG MRS was evaluated at 3T. The MRS measurement of 2HG was reliable and highly reproducible, suggesting that the methods can be used as a noninvasive diagnostic/prognostic tool in gliomas. GABA, a primary inhibitory neurotransmitter, is implicated in a variety of neuropsychiatric disorders. As the fourth topic, GABA level in healthy brain was evaluated using PRESS TE=92 ms at 7T, which was optimized for separating the GABA and Glu signals between 2.2 and 2.4 ppm. The data from multiple brain regions indicated that GABA is higher by 7 - 8 fold in gray matter regions than in white matter regions.

TABLE OF CONTENTS

PRIOR PUBLICATIONS

1. **Ganji SK**, Maher A, Choi C. *In vivo* ^{1}H MR spectroscopic imaging of glycine in brain tumors at 3T. Magn Reson Med 2014. (Accepted)

2. **Ganji SK**, An Z, Banerjee A, Madan A, Hulsey KM, Choi C. Measurement of regional variation of GABA in the human brain by optimized point-resolved spectroscopy at 7 T *in vivo*. NMR Biomed 2014;27:1167-1175.

3. Madan A, **Ganji SK**, An Z, Choe KS, Pinho MC, Bachoo RM, Maher EM, Choi C. Proton T_2 measurement and quantification of lactate in brain tumors by MRS at 3 Tesla *in vivo*. Magn Reson Med 2014 (Early View).

4. Choi C, **Ganji SK**, Madan A, Hulsey KM, An Z, Zhang S, Pinho MC, DeBerardinis RJ, Bachoo RM, Maher EA. *In vivo* detection of citrate in brain tumors by ^{1}H magnetic resonance spectroscopy at 3T. Magn Reson Med 2014;72(2):316-323.

5. Choi C, **Ganji SK**, Hulsey K, Madan A, Kovacs Z, Dimitrov I, Zhang S, Pichumani K, Mendelsohn D, Mickey B, Malloy C, Bachoo R, DeBerardinis R, Maher E. A comparative study of short- and long-TE ^{1}H MRS at 3 T for *in vivo* detection of 2-hydroxyglutarate in brain tumors. NMR Biomed 2013;26:1242-1250.

6. **Ganji SK**, Banerjee A, Patel AM, Zhao YD, Dimitrov IE, Browning JD, Sherwood Brown E, Maher EA, Choi C. T_2 measurement of J-coupled metabolites in the human brain at 3T. NMR Biomed 2012;25:523-529.

7. Choi C, **Ganji SK**, DeBerardinis RJ, Hatanpaa KJ, Rakheja D, Kovacs Z, Yang XL, Mashimo T, Raisanen JM, Marin-Valencia I, Pascual JM, Madden CJ, Mickey BE, Malloy CR, Bachoo RM, Maher EA. 2-hydroxyglutarate detection by magnetic resonance spectroscopy in IDH-mutated patients with gliomas. Nat Med 2012;18:624-629.

8. Banerjee A, **Ganji SK**, Hulsey K, Dimitrov I, Maher E, Ghose S, Tamminga C, Choi C. Measurement of glycine in gray and white matter in the human brain *in vivo* by ^{1}H MRS at 7.0 T. Magn Reson Med 2012;68:325-331.

9. Geethanath S, Baek H-M, **Ganji SK**, Ding Y, Maher EA, Sims RD, Choi C, Lewis MA, Kodibagkar VD. Compressive Sensing Could Accelerate ^{1}H MR Metabolic Imaging in the Clinic. Radiology 2012;262:985-994.

10. Choi C, **Ganji SK**, DeBerardinis RJ, Dimitrov IE, Pascual JM, Bachoo R, Mickey BE, Malloy CR, Maher EA. Measurement of glycine in the human brain *in vivo* by ^{1}H-MRS at 3 T: application in brain tumors. Magn Reson Med 2011;66:609-618.

11. Choi C, Ghose S, Uh J, Patel A, Dimitrov IE, Lu H, Douglas D, **Ganji SK**. Measurement of N-acetylaspartylglutamate in the human frontal brain by ^{1}H-MRS at 7 T. Magn Reson Med 2010;64:1247-1251.

LIST OF FIGURES

LIST OF TABLES

LIST OF APPENDICES

LIST OF DEFINITIONS

^{1}H	Proton
2HG	2-Hydroxyglutarate
Asp	Aspartate
B_0	Static magnetic field
B_1	External RF field
CSI	Chemical-shift imaging
Cr	Creatine
CRLB	Cramer-Rao lower bound
f_{GM}	fractional gray matter
FID	Free induction decay
FLAIR	Fluid attenuation inversion recovery
FWHM	Linewidth (full width half maximum)
GABA	γ-aminobutyric acid
Gln	Glutamine
Glu	Glutamate
Glx	Glutamate + gluatamine
Glycine	Glycine
GM	Gray matter
GPC	Glycerophosphorylcholine
GPCPC	Glycerophosphorylcholine + Phosphorylcholine
GSH	Glutathione

Lac	Lactate
mIns	Myo-inositol
MPRAGE	Magnetization prepared rapid gradient echo
MRI	Magnetic resonance imaging
MRS	Magnetic resonance spectroscopy
MRSI	Magnetic resonance spectroscopy imaging
NAA	N-Acetylaspartate
NAAasp	Aspartate moiety of N-Acetylaspartate
NAAG	N-Acetylaspartylglutamate
NMR	Nuclear magnetic resonance
PC	Phosphorylcholine
PRESS	Point resolved spectroscopy
RF	Radio frequency
SI	Spectroscopic imaging
STEAM	Stimulated echo acquisition mode
SVS	Single-voxel spectroscopy
SNR	Signal-to-noise ratio
tCr	Creatine + phosphocreatine
tCho	Phosphocholine + glycerophosphocholine + free choline
tNAA	N-acetylaspartate + N-acetylaspartylglutamate
WM	White matter

CHAPTER ONE
Background and introduction

1.1 INTRODUCTION TO THESIS

Proton (^{1}H) magnetic resonance spectroscopy (^{1}H-MRS) confers an effective tool for detecting biochemicals in the human brain noninvasively. Both single-voxel spectroscopy (SVS) and multi-voxel spectroscopy imaging (MRSI or CSI or SI) have been extensively used for studying potential alterations of metabolite concentrations in the human brain in disease conditions such as neuropsychiatric disorders and tumors (1-6). Although these techniques have been around for more than three decades (7-11) their utility in the clinic remains in the province of detecting large signals from metabolites such as N-acetylaspartate (NAA), creatine (Cr), and choline (Cho). The present work aims to develop new SVS and MRSI techniques for reliable imaging of the technically-challenging but clinically-important brain metabolites such as glycine (Gly), glutamate (Glu), glutamine (Gln), 2-hydroxyglurate (2HG), and γ-aminobutyric acid (GABA) and apply in various clinical studies at 3T and 7T.

1.2 BASICS PHYSICS OF MAGNETIC RESONANCE

1.2.1 Origin of the NMR signal

Atomic nuclei have the fundamental particles called protons and neutrons (12,13). These fundamental particles have a quantum mechanical property named “spin” (14). The spin imparts several distinctive properties to the atoms or molecules. An isolated spin-1/2

nuclues can be in exactly two discrete spin states: + ½ or - ½. Based on the atomic and mass number of an atom the spin of the nucleus is determined. Nuclei with odd atomic or odd mass number show special properties under the influence of an external magnetic field (12). Under certain experimental conditions these properties provide us with a tool to probe the physical and chemical properties of materials. When protons are placed in a strong homogeneous magnetic field, the individual spins creates an angular magnetic moment. This moment precesses along the axis of the applied magnetic field (15). The precession frequency, called as Larmor frequency (ω_0), is determined by the applied external homogenous magnetic field (B_0) and the gyromagnetic ratio (γ), which is constant for a given atom and is given by (12,13)

$$\omega_0 = \gamma B_0 \qquad \text{Equation 1.1}$$

In a sample with collection of nuclei, an effective magnetic moment is created which is oriented along the applied external field (conventionally denoted as z-direction) (12,13). Under such conditions there is small abundance of spins oriented along the direction of the applied field compared to the anti-parallel of the applied field. This population difference creates a thermal equilibrium magnetization (M_0) along the z-direction (longitudinal magnetization) and is given by

$$M_0 = \left(\frac{\gamma \hbar^2}{2\pi}\right)\frac{NB_0}{4\kappa T} \qquad \text{Equation 1.2}$$

where N is the total spin population difference, κ is the Boltzmann's constant and T is the absolute temperature. For spin ½ nuclei, the population difference is given by

$$\frac{n\left(+\frac{1}{2}\right)}{n\left(-\frac{1}{2}\right)} = e^{-\frac{\Delta E}{\kappa T}} \qquad \text{Equation 1.2}$$

where n is the number of spins in the particular energy state, ΔE is the energy difference between the spin states. If one perturbs a spin system with a radio-frequency (RF) pulse (B_1, external field), the magnetization is decomposed into longitudinal magnetization (M_z) and transverse magnetization (M_{xy}) and are given by

$$M_z = M_0 \cos\theta \quad \text{and} \quad M_{xy} = M_0 \sin\theta \qquad \text{Equation 1.3}$$

where θ is the angle between applied external (RF pulse or B_1) and static (B_0) magnetic fields, termed a flip angle.

1.2.2 Chemical shifts

Protons in a molecule are surrounded by electrons and protons within the molecule. The electron cloud surrounding the proton modifies the Larmor frequency by

$$\omega_o = \gamma(1-\sigma)B_0 \qquad \text{Equation 1.4}$$

where σ is the effective magnetic shielding that the environment has over the proton. The value of σ depends on the electron density could surrounding the proton. As a result, the peaks from different metabolites appear at different frequency locations. This shift is called a chemical shift and is given by

$$\delta = \frac{\omega - \omega_{ref}}{\omega_{ref}} \times 10^6 \qquad \text{Equation 1.5}$$

where δ is the chemical shift of nucleus under study with Larmor frequency of υ and υ_{ref} is resonant Larmor frequency of a reference nucleus. Chemical shifts are usually presented in parts per million (ppm) (16). For ^{1}H-NMR, tetramethylsilane (TMS) is used as a reference at 0 ppm. The non-exchangeable protons, which can be detected in *in vivo* MRS, produce NMR signals in a relatively small frequency range (i.e., 1 – 5 ppm).

1.2.3 Scalar coupling (J-coupling)

A single proton may interact with one or more protons, which is mediated through bonding electrons between the spins. These surrounding protons cause a small shift in the resonance frequency of the proton under study and this effect is termed indirect or scalar (J) coupling. The strength of J-coupling usually presented in frequency units, Hz (12,13). The coupling constants are characteristics of given molecule under specific environment and are independent of field strength (B_0) (12,13). The magnitude of the coupling constants depends on the molecular geometry and number of intervening bonds. Due to the J-coupling effects, most metabolites exhibit complex spectral patterns (multiplets), thereby leading to overlapping of signals. For example, the signals of Glu, Gln, GABA, and 2HG are extensively overlapped between 2 and 2.5 ppm, as shown in the Figure 1-1.

1.3 RELAXATION MECHANISMS

Relaxation processes bring the perturbed NMR system back to its equilibrium state ($M_z = M_0$ and $M_{xy} = 0$). This happens by two processes, namely transverse and longitudinal relaxation (17).

1.3.1 Transverse Relaxation

Transverse relaxation is a process by which the transverse magnetization (M_{xy}) decays to the equilibrium value of zero. This relaxation process can be modeled as an exponential function of time,

$$M_{xy} = M_0 \sin\theta \left(e^{\frac{-t}{T_2}} \right) \qquad \text{Equation 1.6}$$

where T_2 is the time during which the transverse magnetization reduces to 1/e of the M_{xy} at zero TE, as shown in Figure 1-2. The proton transverse relaxation is primarily caused by the effects of direct spin-spin coupling (i.e., dipole-dipole interaction) and diffusion of the molecules under the inhomogeneous magnetic fields. The transverse relaxation times are very important for quantification when metabolites signals are measured at long echo times.

1.3.2 Longitudinal Relaxation

Longitudinal relaxation is a process of longitudinal magnetization (M_z) recovery to the thermal equilibrium magnetization (M_0). It is often referred to as spin-lattice relaxation and its recovery from zero M_z may be given by the equation

$$M_z = M_0 \left(1 - e^{\frac{-t}{T_1}} \right) \qquad \text{Equation 1.7}$$

where the T_1 is the time during which the longitudinal magnetization recovers to approximately 0.63 ($= 1 - e^{-1}$) times the thermal equilibrium magnetization (M_0), as shown in Figure 1-3.

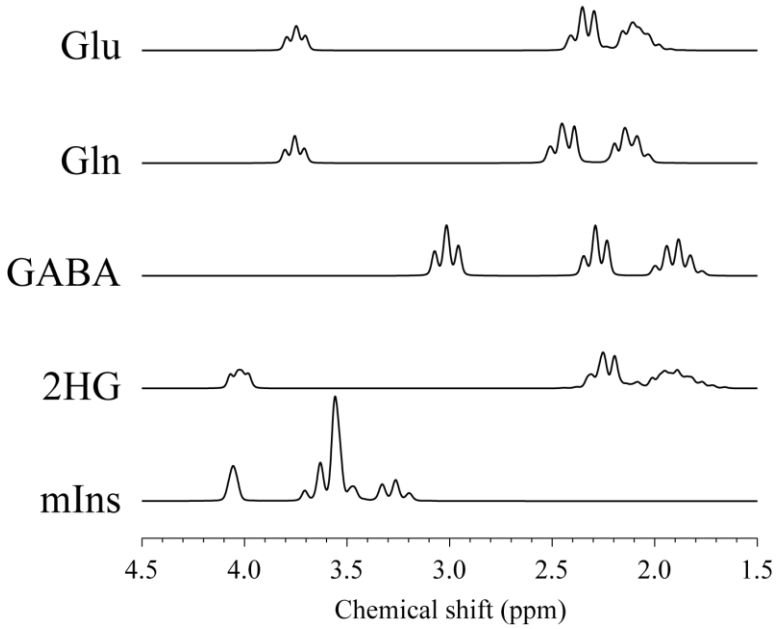

Figure 1-1 Example of signal overlap of J-coupled metabolites.
Signals of Glu, Gln, GABA, and 2HG at equal concentrations, numerically calculated for 90º-acquisition. Linewidth is broadened to singlet linewidth of 0.03 ppm.

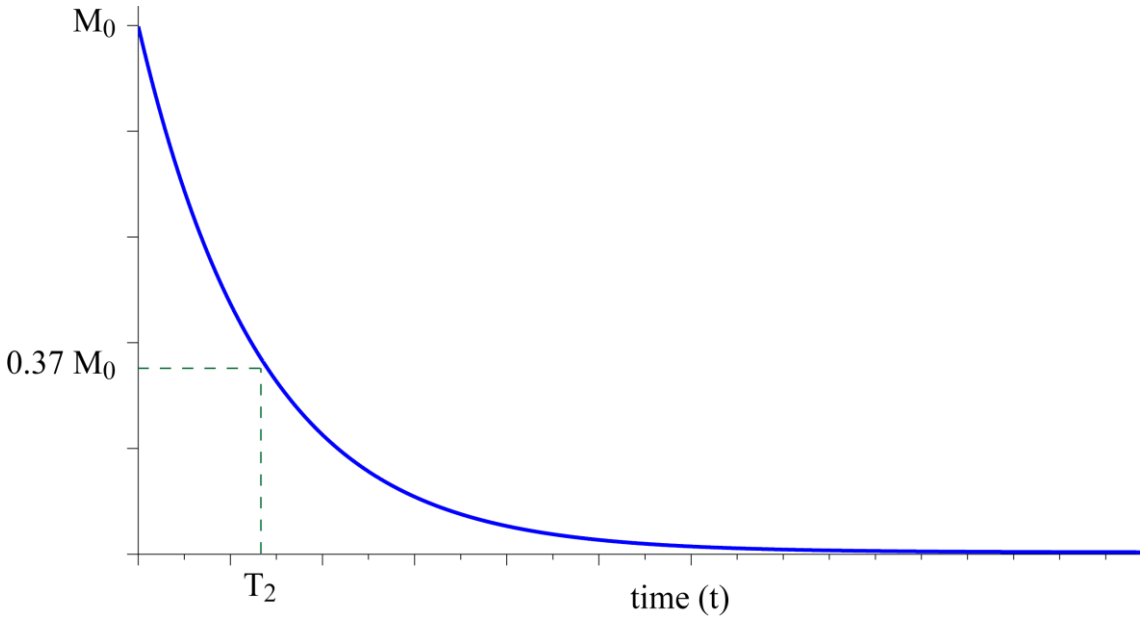

Figure 1-2 Transverse relaxation (T_2) time curve after 90º RF pulse excitation.
The transverse magnetization (M_{xy}) decays exponentially towards its equilibrium value of zero at a rate of $1/T_2$. T_2 is the time for the M_{xy} to reduce to 37% of M_0.

1.3.3 Bloembergen, Purcell, Pound (BPP) theory

Bloembergen, Purcell, Pound (BPP) theory is a way to explain the proton relaxation times (T_1 and T_2) based on the correlation times (τ_c, the average time it takes a molecule to rotate over one radian) and the proton-proton distance (r) (17). According to the BPP theory T_2 is given by

$$\frac{1}{T_2} = \frac{K}{2}\left[3\tau_c + \frac{5\tau_c}{1+\omega_0^2\tau_c^2} + \frac{2\tau_c}{1+4\omega_0^4\tau_c^4}\right] \qquad \text{Equation 1.8}$$

where

$$K = \frac{3\mu^2\hbar^2\gamma^4}{160\pi^2 r^6} \qquad \text{Equation 1.9}$$

As molecular radius increases the correlation time increases and thus rate of relaxation rate ($1/T_2$) increases. Large molecules usually show shorter T_2 than small molecules. Figure 1-4 shows the effect of τ_c on T_2 and T_1. In liquids T_2s are nearly equal to T_1s, while in solids T_2s are much shorter compared to T_1s.

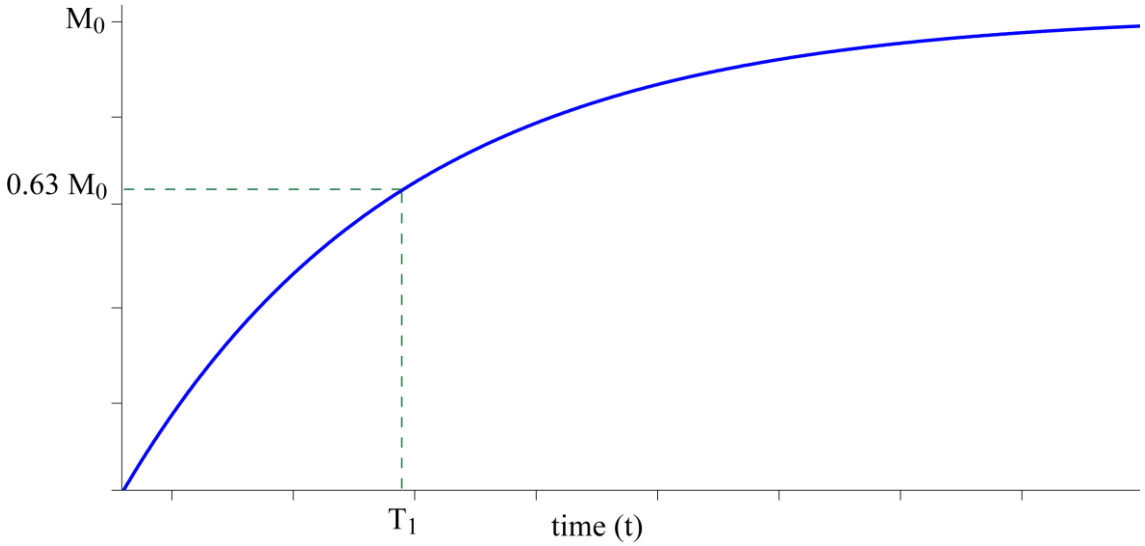

Figure 1-3 Longitudinal relaxation curve. The longitudinal magnetization (M_z) recovers at a rate of $1/T_1$. T_1 is the time by which M_z recovers to 63% of M_0.

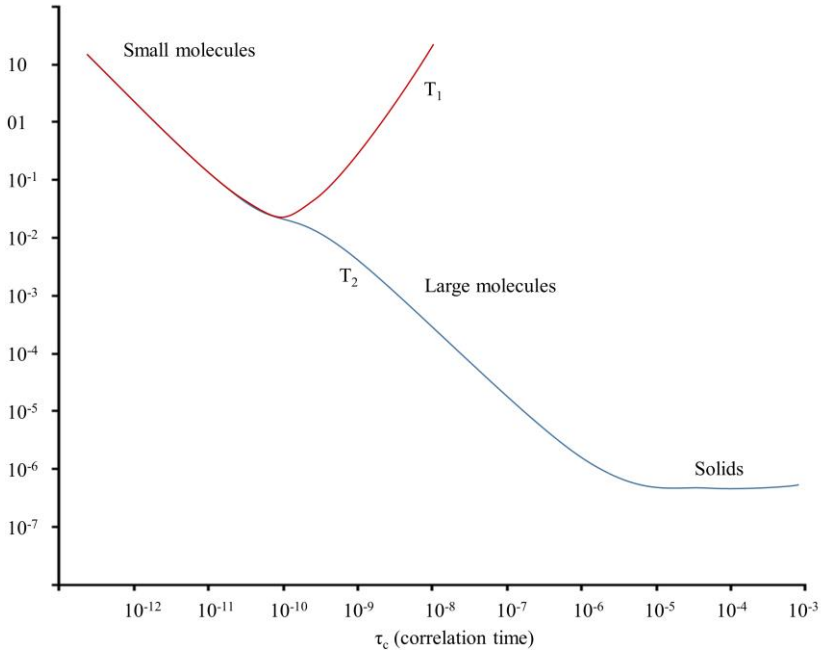

Figure 1-4 A plot of transverse and longitudinal relaxation times versus correlation time (τ_c).

1.4 TECHNIQUES OF ^{1}H-MRS

1.4.1 Slice selection and localization

When a linear magnetic field gradient is applied along a direction to a sample under homogenous B_0, a linear distribution of magnetic field (B) is created along that direction. When a frequency selective RF pulse is applied with a gradient pulse at the same time, a portion of the sample (a slice), within which the precession frequencies are within the excitation bandwidth of the RF pulse, is excited. This process is termed localization or slice selection. The position of the slice is determined by the carrier frequency of the RF pulse and applied linear magnetic field gradient strength. The bandwidth of the RF pulse and the applied magnetic field gradient strength determine the thickness of the slice (Figure 1-5)

(16). The slice thickness (Δz) is determined by gradient strength (G) and RF pulse bandwidth (Δω), as shown in Eq. 1.10.

$$\Delta z = \frac{\Delta \omega}{\gamma G} \qquad \text{Equation 1.10}$$

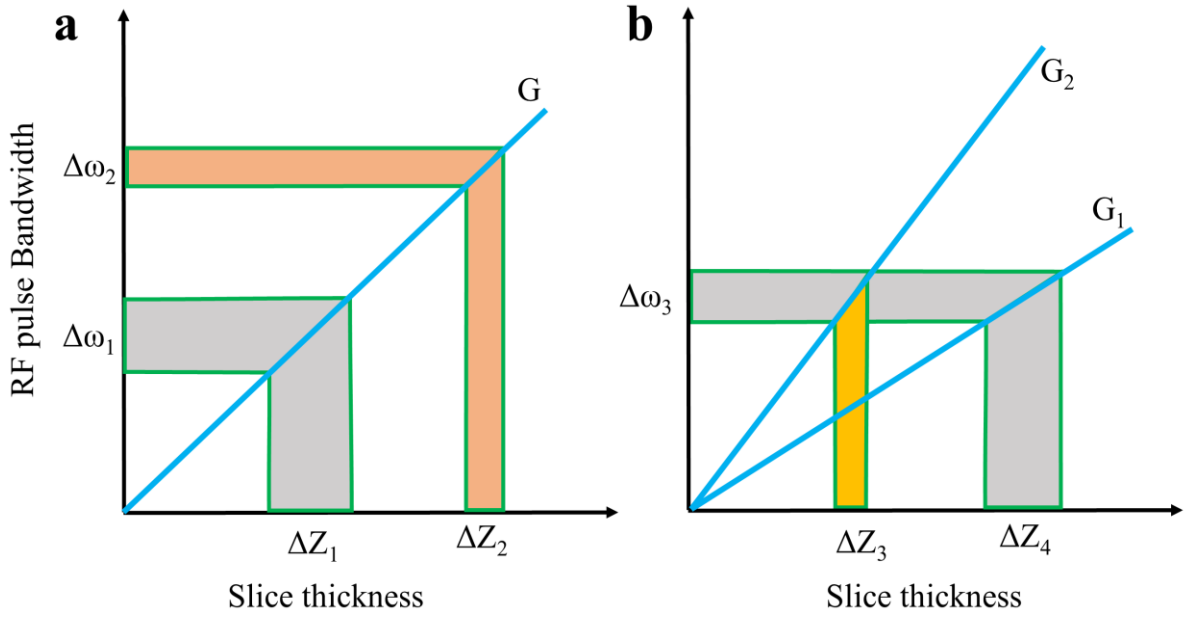

Figure 1-5 A schematic diagram for slice selection by an RF pulse and linear gradient. (a) For a gradient strength (G) and an RF pulse with bandwidths $\Delta\omega_1$ or $\Delta\omega_2$, the spins within the slice of thickness ΔZ_1 or ΔZ_2 are excited, respectively. (b) For a given RF bandwidth ($\Delta\omega_3$), the thickness of the slice thickness can be adjusted by changing the strength of the applied linear gradient.

1.4.2 Single-voxel ^{1}H-MRS sequences

Proton MRS methods include single-voxel spectroscopy (SVS) and multi-voxel imaging (MRSI or SI or CSI) (1). SVS and many MRSI sequences include volume-selective schemes that are based on either the SE (Spin Echo), point resolved spectroscopy (PRESS), or the Stimulated Echo Acquisition Mode (STEAM) techniques (1). In SVS signals are obtained from a volume in the brain using three slice-selective RF pulses. The two most

commonly used techniques for single-voxel localized *in vivo* ^{1}H-MRS are PRESS and STEAM. Both sequences have three slice selection RF pulses with additional gradients to modulate the transverse magnetization. The basic components of PRESS and STEAM sequence are shown in Figure 1-6. The volume and orientation of the desired region can be adjusted with changing the strength and directions of the slice select gradients. A PRESS sequence induces full refocusing and consequently yields larger signal compared with STEAM sequence, for same TE and TR. PRESS sequence is less sensitivity to motion artifacts when compared to STEAM (18,19). The major characteristics of each sequence are tabulated in Table 1-1.

	PRESS	STEAM
Number of RF pulses	3	3
Type of the signal	Spin echo	Stimulated echo
Signal	Fully refocused	Half refocused
Sensitivity to motion artifacts	Relatively small	Large
Chemical shift displacement errors	Large	Small
Minimum echo time	Longer	Shorter
SAR	Relatively large	Small

Table 1-1 Comparison of PRESS and STEAM sequences

1.4.3 Basic sequence of multi-voxel ^{1}H-MRS

MRSI allows to acquire the spatial distribution of metabolites levels. MRSI generates spectra from an array of locations. This can be achieved by means of phase-encoding

gradients, similar to the encoding in magnetic resonance imaging (MRI). Table 1-2 highlights major differences between SVS and MRSI methods.

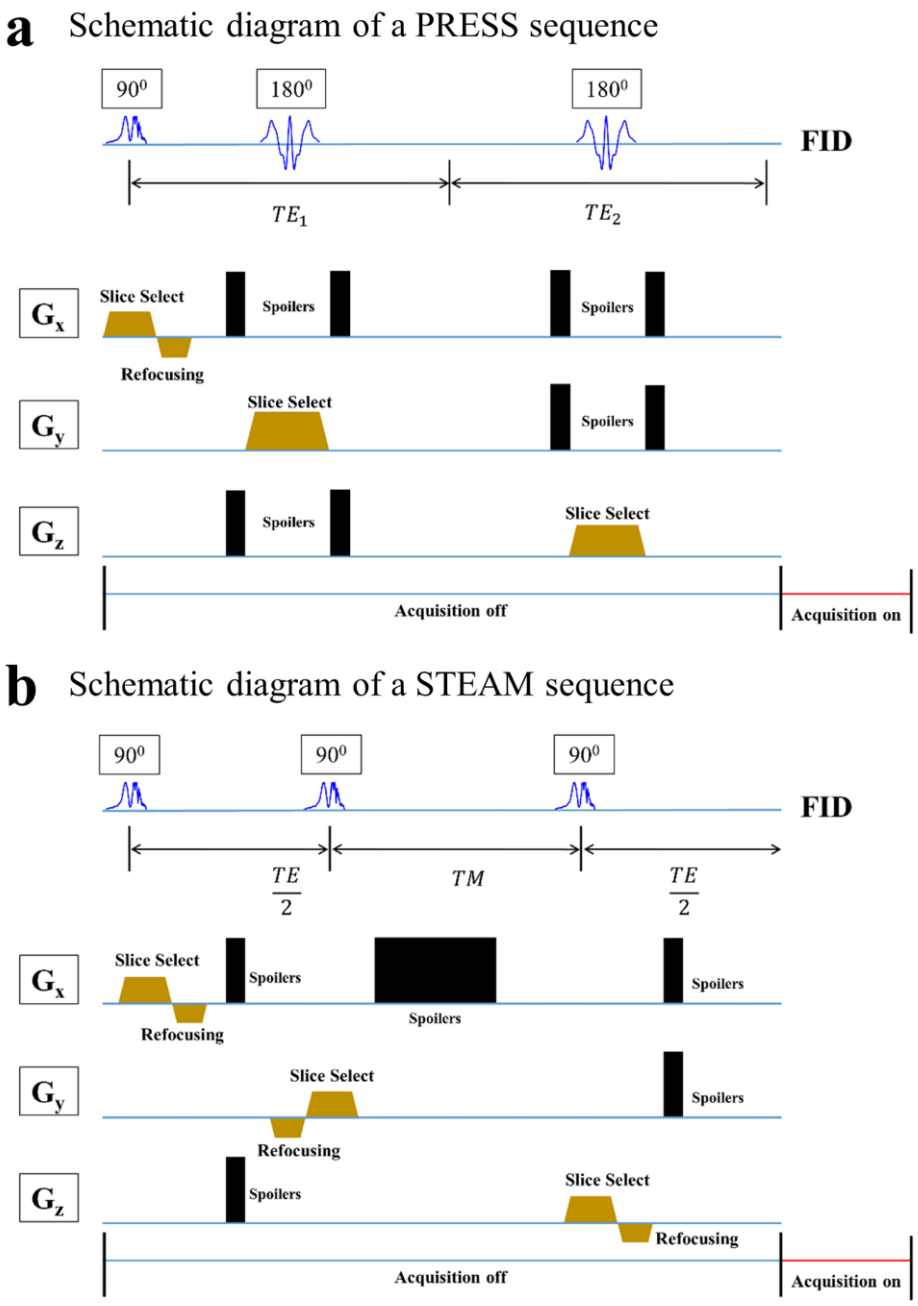

Figure 1-6 Schematic diagrams of single-voxel localized PRESS and STEAM sequences.

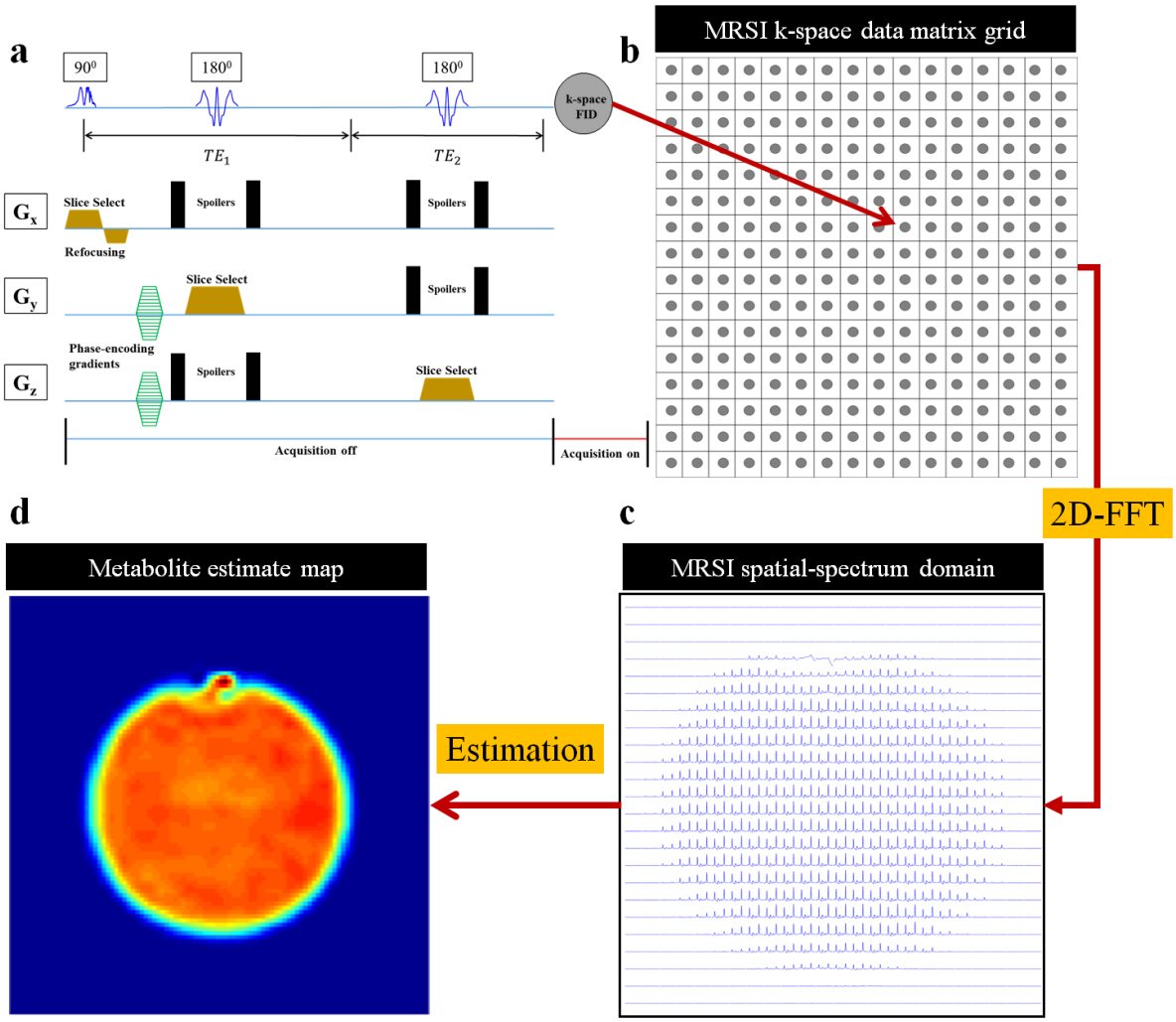

Figure 1-7 Illustration of PRESS-based MRSI.
The volume-of-interest (VOI) is selected by 90°-180°-180° RF pulses (PRESS sequence). Phase-encoding gradients are applied along the x and y directions for imaging of metabolites. Each acquisition forms a point in the k-space. The k-space data are Fourier transformed to obtain the spectra in Cartesian coordinates and subsequently the metabolite maps.

For example, basic components of a 2D-PRESS MRSI sequence is presented in Figure 1-7. The volume of interest (VOI) is prescribed by the three slice select RF pulses of the PRESS sequence, whereas field of view (FOV) is selected by phase encoding gradients whose strength is varied during the acquisition for spatial localization. For each gradient

increment, phase-encoded FID is placed in the k-space according to the gradient strength applied. A two-dimensional Fourier transformation converts the k-space to spatial-domain localized FIDs.

	NAA	Cr	Cho	Glu	Gln	GABA	Gly	mIns	2HG	Lac
Low grade gliomas	↓	↓	↑	↑	↑	---		↓	↑	↑
High grade gliomas	↓	↓	↑	↑	↑	---	↑	↓	↑	↑
Schizophrenia	↓	↓	---	↑	---	↑	---	---	---	---
Seizure disorders	↓	---	---	↑	↑	---	---	↑	---	---
Dementia	↓	---	---	---	---	---	---	↑	---	---

Figure 1-8 Reported alterations of brain metabolites in disease conditions (20).

	SVS	MRSI
Acquisition time	Short	Long
Coverage	Small coverage	Larger coverage
SAR	Low	High
Quantification	Relatively simple	Time consuming
Motion susceptibility	Relatively small	Large
Effects of inhomogeneous B_0 distribution	Small	Large

Table 1-2 SVS and MRSI comparison.

1.5 APPLICATION OF ^{1}H MRS IN HUMAN BRAIN

Metabolites in the human brain performs several specific roles to maintain normal functioning. For example GABA is a dominant inhibitory neurotransmitter in the human brain, with high concentrations in presynaptic terminals of neuronal cells and maintains neural activity (21-25). Table 1-3 describes commonly measured brain metabolites and their role under normal brain function. The metabolite level is altered in disease conditions such as neuropsychiatric disorders and tumors (1,4-6,26-28). Figure 1-8 indicates changes observed in metabolite levels in various diseases (20).

Metabolite	**Role in the brain**
NAA	Neuronal cell marker
N-acetylaspartylglutamate (NAAG)	Excitatory neurotransmission
Cho	Membrane component
Lactate (Lac)	Anaerobic glucose metabolism indicator
Cr	Energy metabolism of cells
Glu	Excitatory neurotransmitter
Gln	Glutamate metabolism
Gly	Inhibitory neurotransmitter
myo-inositol (mIns)	Present only in glial cells
GABA	Inhibitory neurotransmitter

Table 1-3 Brain metabolites and clinical significance.
Commonly measured human brain metabolites and their role.

1.6 NUMERICAL SIMULATIONS OF METABOLITE SPECTRA

Numerical simulations of metabolite spectra provides a tool for optimizing experimental parameters and generating modeled spectra for spectral fitting analysis (6,29,30).

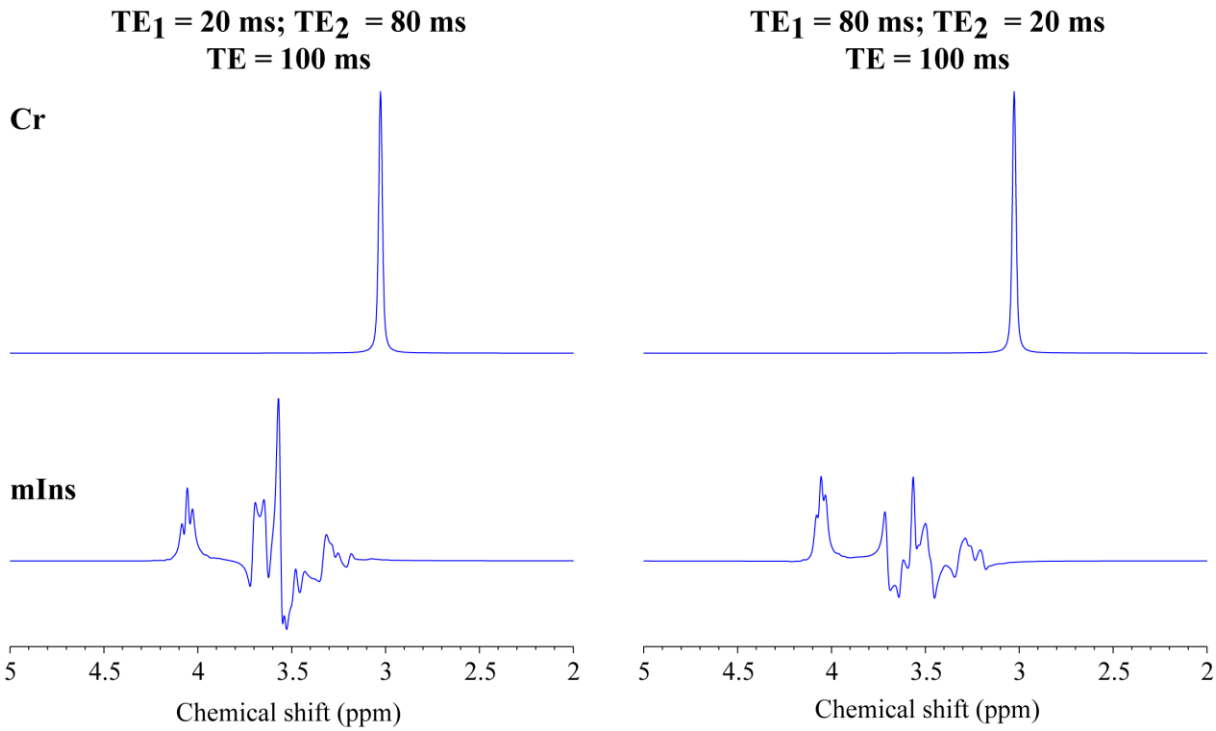

Figure 1-9 Spectral pattern of mIns and Cr with PRESS at two subecho time sets with same total TE.
Spectral pattern of mIns at (TE_1 = 20 ms and TE_2 = 80 ms) and (TE_1 = 80 ms and TE_2 = 20 ms). The Cr singlet peak is shown for comparison.

1.6.1 Effects of PRESS subecho times on spectra of J-coupled metabolites

PRESS, a double spin-echo sequence, has two sub-echo times (i.e., TE_1 and TE_2) and allows high variability for evolution of the J-coupled metabolites signals (7,8). A PRESS

sequence is shown in Figure 1-6. The total echo time (TE) is the sum TE_1 (twice the time between 90° and first slice–selective 180° RF pulses) and TE_2 (twice the time between second slice–selective 180° RF pulse and the onset of FID acquisition). The subecho times of the PRESS sequence modulate the evolution of J-coupled-spin metabolite spectra, allowing an opportunity to simplify the spectral complexities arising from signal overlaps and consequently to improve the detectability of relatively small signals (6,29,31-33). For example, for the same total echo time of 100 ms, mIns exhibits different spectral patterns at (TE_1 = 20 ms and TE_2 = 80 ms) and (TE_1 = 80 ms and TE_2 = 20 ms), as shown in Figure 1-9. Using the variation of the spectral pattern in J-coupled-spin metabolites, we optimized PRESS subecho times to achieve good selectivity for difficult-to-detect metabolites at 3T and 7T. A detailed description of optimization performed for the metabolites of interest is provided in later chapters and in appendix A.

1.7 METABOLITE'S OF SPECIFIC INTEREST IN THE THESIS

1.7.1 Glycine (Gly)

Gly, a non-essential amino acid, is a inhibitory neurotransmitter and acts as co-agonist of glutamate on N-methyl D-aspartate receptors (34,35). Also, Gly is a precursor for the synthesis of proteins and a primary source of one-carbon units in cellular metabolism (36). Several recent studies indicated elevation in Gly levels in several brain disorders, in particular, high grade tumors (5,37-44), indicating a potential use of Gly as a biomarker for detecting high grade gliomas. Noninvasive analysis of Gly levels may therefore be vital for clinical management of gliomas (5,45).

1.7.2 Glutamate (Glu) and Glutamine (Gln)

Gln is the most abundant amino acid in plasma, essential for several metabolic activities such as cell growth, protein synthesis and energy production (46-52). It is catabolized into Glu, which is a precursor for production of GABA (47,49,51,52). Radioactive labeled glutamine and glutamate analogs are currently under clinical development (53,54) and may provide better understanding of cancer metabolism. Prior studies indicated alterations in Gln and Glu levels in a variety of neurological diseases (52,55,56). Although several MRS techniques for noninvasive measurement of Glu and Gln were reported, precise measurement of these metabolites remains challenging due to the extensive spectral overlaps between the signals, particularly at 3T. Therefore it is important to develop new Glu and Gln imaging methods with improved precision.

1.7.3 γ-aminobutyric acid (GABA)

GABA is a primary inhibitory neurotransmitter in the human brain, with high concentrations in presynaptic terminals of neuronal cells (21-25,57). Alterations in GABA levels may be implicated in several psychiatric and neurological disorders such as schizophrenia, anxiety disorders, epilepsy (58). In brain tumors it is suggested that insufficient levels of GABA may potentially cause seizures (59,60). Also several pharmacological medications target the GABAergic pathways changing the GABA levels. Given its significant role in the human brain, the ability of measuring GABA precisely is of high significance.

1.7.4 2-Hydroxyglutarate (2HG)

Recently mutations were identified in isocitrate dehydrogenase (IDH) in >70% of low grade gliomas and secondary glioblastomas (61-64). The IDH mutation is associated with increased overall survival compared to wild type tumors (64). IDH mutations result in the production of 2HG from α-ketoglutarate (61). Though the metabolic and oncogenic role of 2HG remain unclear, recent studies showed that the IDH mutational status of lesions can be assessed noninvasively using *in vivo* ^{1}H-MRS techniques (6,27,30).

1.8 THESIS AIM

The primary focus of the present thesis will be on precise measurement of several clinically-important metabolites such as Gly, GABA, and 2-hydroxyglutarate (2HG). Detecting these metabolites is challenging mainly due to their relatively small signal strengths, which arise largely from the effects of Jcoupling between the proton spins and due to the spectral overlaps with adjacent large signals. The reliability of the metabolite measurements may be governed by signal specificity, signal-to-noise ratio (SNR), and spatial resolution (in case of spectroscopic imaging). The thesis presents new ^{1}H-MRS methods for *in vivo* measurement of Gly, 2HG, Glu, Gln, and GABA in human brain at 3T and 7T.

CHAPTER TWO
T_2 measurement of J-coupled metabolites in the human brain at 3T

2.1 INTRODUCTION

2.1.1 Literature review

Proton MRS offers a noninvasive tool for measuring metabolites in the human brain *in vivo*. While measurement with short TE benefits from minimum T_2 signal loss, long-TE approaches are often employed as an alternative (65-67), with advantages that TE optimization can improve the spectral resolution and the uncertainties of metabolite measures due to broad baseline signals from macromolecules are reduced. The detected signals are, however, T_2 weighted and thus may not reflect the metabolite concentrations directly. T_2 relaxation may reflect the cellular and molecular environments of metabolites in the brain; e.g., viscosity of the cellular fluids and microscopic susceptibility distribution within cells (68,69). Increased T_2 relaxation could occur due to reduced cell volumes and altered micromolecule structures in bipolar disorder and schizophrenia (70). A reasonable estimate of metabolite T2 may therefore be valuable not only for quantification of the metabolite levels but also for understanding the physiological and pathological changes in disease conditions.

Most of prior studies of T_2 measurements for metabolites in the human brain focused on prominent singlet signals, such as N-acetylaspartate (NAA), total creatine (tCr), and total choline (71-79). While the TE dependence of a singlet is described by T_2 relaxation only, the time evolution of scalar coupled metabolite signals is affected by the effects of the J

evolution as well as T_2 relaxation. Measurements of relaxation times of coupled resonances therefore require proper evaluation of the J evolution on the signals (80,81). The primary excitatory neurotransmitter glutamate (Glu) and the glial marker myo-inositol (mIns) are measured in many clinical studies (82). The complex behavior of the multiplets with changing TE, which occurs due to strong coupling effects, makes it difficult to measure the T_2 relaxation times *in vivo*. Moreover, when the bandwidth of the spatially localizing RF pulses are not much greater than the spectral distance between coupled resonances, non-uniform coherence distribution within the localized volume arises from chemical shift localization errors (83), resulting in complicated behavior of the multiplets with changing TE. Due to these spectral complexities, there is paucity in reports of T_2 relaxation times of coupled-spin metabolites.

Due to its single-shot volume-localization full-refocusing capability, point-resolved spectroscopy (PRESS) is widely used in clinical studies. The *in vivo* evaluation of brain metabolite T_2 may depends on MRS sequence. As shown by Michaeli *et al.* (75), signal reduction due to the molecular diffusion effects may result in reduced T_2 estimates ($T_2^{\dagger}$) when measured with PRESS, compared to Carr Purcell-type sequences. Thus, signal reduction with increasing TE may be greater in PRESS than in sequences with increased number of 180° RF pulses. Thus, the Glu T_2 values obtained using a triple-refocusing method (80) may not be directly applicable to PRESS measures of Glu at intermediate or long TEs. Given the field dependence of metabolite T_2 measures (75) and the utility of long-TE approaches for measurements of J-coupled metabolites at 3T, a field strength increasingly

available for *in vivo* spectroscopy, measurement of $T_2^{\dagger}$ of coupled metabolites by PRESS at 3T is of high significance.

2.1.2 Aim of the project

To measure apparent proton T_2 relaxation times ($T_2^{\dagger}$) of metabolites in the human brain at 3T, using a PRESS sequence. The metabolites measured include Glu, mIns, NAA aspartate (Asp) moiety, and N-acetylaspartylglutamate (NAAG), in addition to tCr, NAA and choline singlets.

2.2 MATERIALS AND METHODS

2.2.1 Experimental setup

Experiments were carried out on a 3.0 T whole-body Philips scanner with actively shielded gradient coils (maximum gradient strength 80 mT/m; slew rate 200 mT/m/ms) (Philips Medical Systems, Best, The Netherlands). An integrated body coil was used for RF transmission and an eight-channel phased-array head coil for signal reception.

2.2.2 MR Spectroscopy acquisition details

A PRESS sequence was used for measurement of apparent T_2 ($T_2^{\dagger}$) of brain metabolites. Single-voxel localization was obtained with a 9.8-ms amplitude/frequency-modulated 90° RF pulse (bandwidth = 4.25 kHz) and 13.2-ms amplitude-modulated 180° RF pulses (bandwidth = 1.27 kHz), the same RF envelopes used as in a prior study (84). A vendor-set maximum allowed RF field intensity (B_1 = 13.5 μT) was used for the RF pulses. The slice selection was obtained along the anterior-posterior, left-right, and foot-head

directions using the 90° and the first and second 180° RF pulses, respectively, for which the gradient strength was 4.0 and 1.0 mT/m for slice thickness of 25 and 30 mm, respectively. A pair of spoiling gradients (3.5 ms long; 20 mT/m) was applied in the same direction as that of the slice selective gradient for each 180° pulse.

Four pairs of PRESS subecho times were used for $T_2^{\dagger}$ measurement; (TE_1, TE_2) = (32, 22), (32, 80), (32, 214), and (36, 338) ms. Here, the echo time pair (32, 22) ms was the shortest possible for the chosen RF and gradient pulses. The other three TE_1-TE_2 pairs were obtained from density-matrix simulations, largely focusing on Glu. The C4-proton multiplet of glutamate was varied with changing TE due to the J coupling effects, giving relatively large and positive signals at TE = ~110, ~250, and ~370 ms, for which the subecho times were asymmetric ($TE_1 \neq TE_2$). We chose subecho time pairs with $TE_1 < TE_2$ because residual eddy current artifacts may be less in these pairs than in $TE_1 > TE_2$. The simulations were performed including the effects of the shaped RF and gradient pulses as well as the Zeeman, chemical shift and J coupling effects, thus the effects of the finite bandwidth of volume selective RF pulses are accounted for precisely. Published chemical shift and coupling constants were used in the simulation (82). The simulations were programmed with Matlab (The MathWorks Inc., Natick, MA, USA).

2.2.3 Phantom studies

The optimized PRESS echo times were tested in an aqueous solution (pH = 7.2) with Cr (8 mM), Glu (20 mM), and Gln (20 mM). Phantom spectra were obtained from a $25\times25\times25$ mm^3 voxel, using a TR of 10 s ($> 5T_1$), and compared with numerically-calculated spectra.

2.2.4 *In vivo* studies

In vivo measurement of brain metabolite $T_2^{\dagger}$ was conducted in five healthy volunteers (2 female and 3 male; age 27±7 years). The protocol was approved by the Institutional Review Board of the University of Texas Southwestern Medical Center. Written informed consent was obtained prior to the scans. Following survey scans, T_1-weighted images (MP-RAGE) were acquired (TR/TE/TI = 2500/3.7/1300 ms; flip angle = 8°; field of view = 240 × 240 × 150 mm; 150 slices; resolution = 1 × 1 × 1 mm^3). Spectroscopic data were obtained from the medial occipital and left occipital regions (voxel size 25 × 30 × 30 mm^3), which are predominantly gray- and white-matter, respectively. The number of averages was 16, 32, 64, and 128 for the four TEs, respectively, to compensate for the SNR loss at longer TEs, similarly to the prior study (76). First- and second-order shimming for the selected volume was carried out using the fast automatic shimming technique by mapping along projections (FASTMAP) (85). The linewidth of the water signal was ~7 Hz at TE = 54 ms. Data acquisition parameters included; TR = 3 s, sweep width = 2.5 kHz, and sampling points = 2048. Following 6 dummy scans, signals were recorded in multiple blocks, each with 4 averages. A 64-step phase cycling scheme was used for the PRESS data acquisition. The carriers of slice-selective RF pulses were set at 3 ppm. A four-pulse variable-flip-angle scheme was used for water suppression. Unsuppressed brain water signals were acquired at the four TEs with the same gradient schemes as those of water-suppressed acquisitions. The total MR scan time was ~1 hour including the shimming, power calibration, and water imaging.

2.2.5 Analysis and quantification of MRS data

The multi-block data were processed individually for correction of eddy current artifacts and frequency drifts using an in-house written Matlab® program. Residual eddy current effects were minimized using the unsuppressed brain water signal. The frequency drifts were corrected using the NAA singlet as a reference. Data were apodized with a 1-Hz exponential function for enhancing SNR and removing potential artifacts in the later part of FID. Spectral fitting was performed using the LCModel software (86). 3D volume localized model spectra of brain metabolites were numerically calculated and used as a basis function for the fitting. The basis function included 18 metabolites; tCr, NAA, Glu, mIns, GABA, NAAG, GPCPC (glycerophosphocholine + phosphocholine), Gln (glutamine), GSH (glutathione), glycine, taurine, scyllo-inositol, acetate, aspartate, phosphoethanolamine, ethanolamine, lactate, and threonine. Given the potential differences in relaxation times between resonances within a metabolite, model spectra were created individually for subgroups of the metabolite according to their coupling connections. These metabolites included tCr (methyl and methylene groups), NAA (acetyl and aspartate moieties), NAAG (acetyl, aspartyl, and glutamate moieties), and GSH (glycine, cysteine, and glutamate moieties). The spectral fitting range was set to 0.5 – 4.1 ppm. Cramér-Rao lower bounds (CRLB), which represent the lower bound of precision, were returned as a percentage standard deviation (%SD) with respect to the signal estimates. The LCModel estimates of signal strengths at the four echo times were fitted with a monoexponential function, $exp(-TE/T_2^{\dagger})$. The fitting was performed on LCModel estimates with CRLB less than 20% at all the four TEs. The T_1-weighted images were segmented, using Statistical Parametric

Mapping software (SPM5), to obtain the fractions of gray matter (GM), white matter (WM), and cerebrospinal fluids (CSF) within the voxels.

2.3 RESULTS

2.3.1 Phantom studies

Figure 2-1 presents comparison between numerically calculated (sum) and phantom spectra of Glu, Cr3 (Cr-CH_3) and Cr2 (Cr-CH_2) for the four pairs of PRESS subecho times, together with a calculated spectra of individual metabolites. The signal strength and spectral pattern of Glu and Gln varied with changing echo time due to the J evolution of the coupled resonances. The echo time dependence of the multiplets was in good agreement between calculation and experiment for both Glu and Gln. The Glu multiplet pattern was well preserved at the optimized echo times (except for (TE_1, TE_2) = (32, 22) ms). These simulation results were reproduced in phantom spectra, with phantom T_2†s of Glu, Gln, Cr-CH_3 and Cr-CH_2 at 720, 660, 1190 and 890 ms, respectively.

2.3.2 *In vivo* studies

Figure 2-2 presents *in vivo* spectra from medial occipital and left occipital cortices of 5 subjects enrolled in the study, obtained at the four pairs of PRESS subecho times, together with voxel positioning (voxel size 25×30×30 mm^3). The spectra from the 5 subjects showed similar pattern for each voxel, indicating consistent voxel positioning between the subjects. The spectral patterns in the 2.2 – 2.5 ppm and 3.4 – 3.65 ppm regions, which were largely attributed to Glu and mIns, respectively, showed good agreement between the subjects. The

GPCPC singlet intensity was quite different between the regions, likely due to differences in gray and white matter contents within the voxels. The GPCPC singlet at 3.2 ppm was about 50% the tCr-CH_3 singlet at TE = 54 ms. This signal ratio increased with TE and their signal strengths were similar at TE = 374 ms, indicating a long T_2† of GPCPC compared to that of tCr.

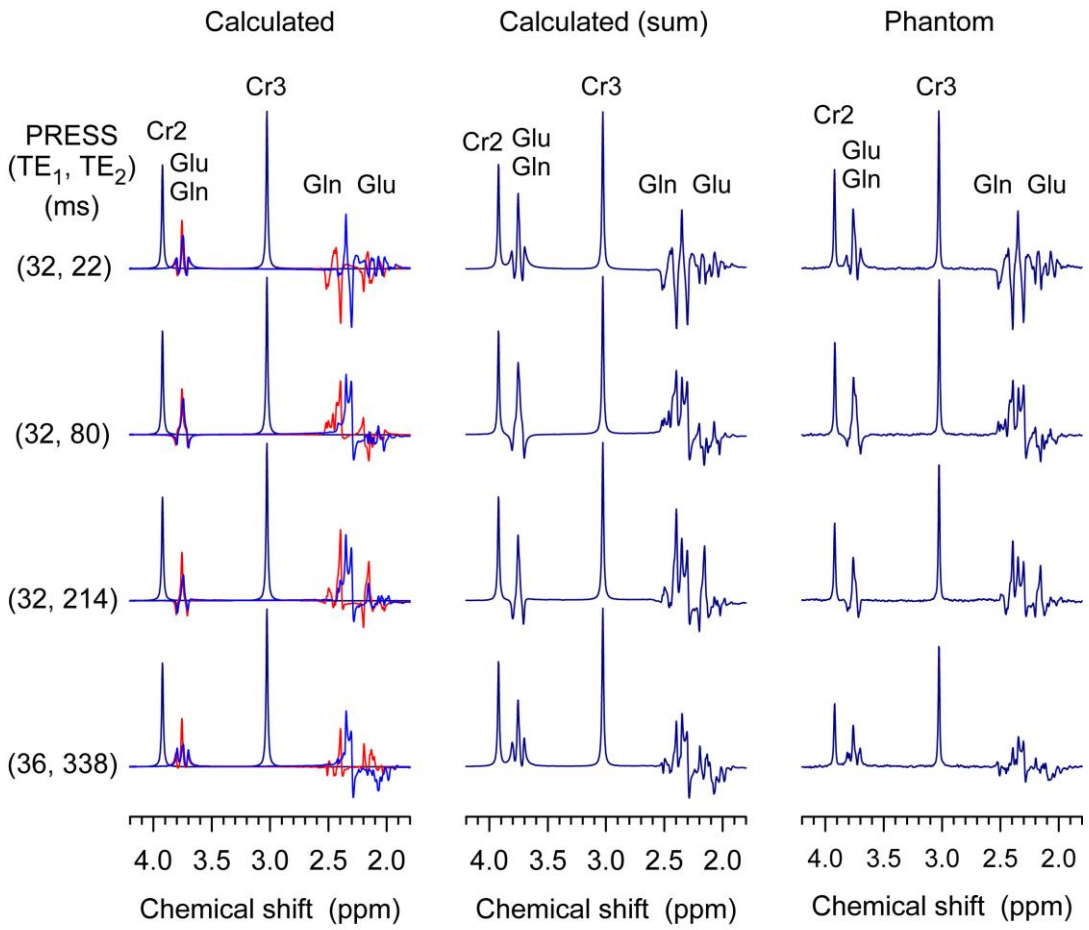

Figure 2-1 Phantom data at the four (TE_1, TE_2) pairs of PRESS
Comparison between numerically calculated and phantom spectra of Glu (20 mM), Gln (20 mM), and Cr (8 mM) for the four pairs of PRESS subecho times (TE_1, TE_2) used for *in vivo* T_2 measurements. Spectra were broadened to 2.5 Hz. Spectra were calculated ignoring the signal reduction due to T_2 effects.

Segmentation of T_1-weighted images gave mean fractions of GM, WM and CSF as 60±3, 25±2 and 15±1% for medial occipital, and 16±2, 74±4 and 10±2% for left occipital, respectively. Figure 2-3 displays *in vivo* spectra at the four PRESS TEs from the medial and left occipital cortices of a healthy subject (subject 1 in Fig. 2-2), together with LCModel fits and residuals. The spectra were all well reproduced by the fits, resulting in residuals without considerable dependence on chemical shift resonance. Due to the increased number of signal averages at the longer TEs (16, 32, 64 and 128 for TE = 54, 112, 246 and 374 ms, respectively), the residuals were progressively smaller with increasing TE.

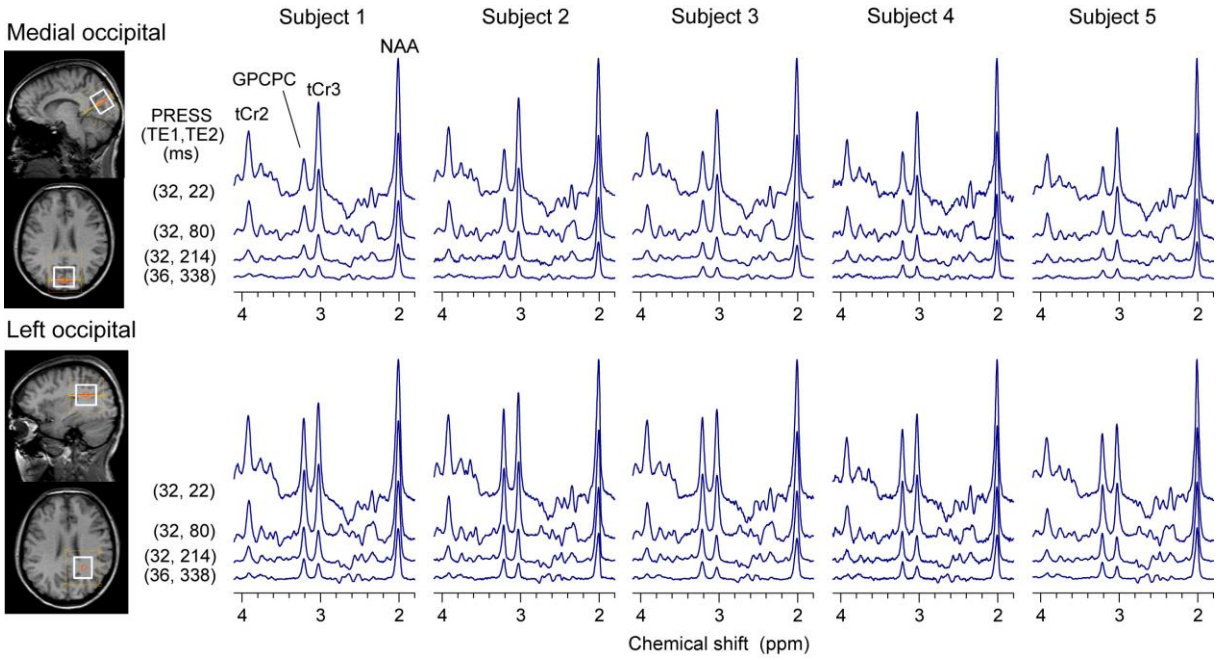

Figure 2-2 *In vivo* spectra from five subjects.
In vivo spectra, at the four (TE_1, TE_2) pairs of PRESS, from medial occipital and left occipital cortices of five healthy volunteers are presented together with voxel positioning (size 25×30×30 mm^3). Spectra are normalized with respect to the NAA singlet at TE = 54 ms for each brain region. FIDs were filtered with a 1-Hz exponential function prior to the Fourier transformation. The number of signal averages was 16, 32, 64, and 128 for TE = 54, 112, 246, and 374 ms, respectively (TR = 3 s).

Monoexponential fitting for metabolite $T_2^{\dagger}$ estimation was performed for LCModel estimates at the four TEs that had CRLBs less than 20%. The fitting included the multiplets of Glu, mIns, the NAA-Asp moiety, and the NAAG singlet, in addition to the three prominent signals, *i.e.*, the singlets of tCr (3.03 ppm), NAA (2.01 ppm) and GPCPC (3.2 ppm). The CRLB of Glu was 2 - 4% at TE = 54, 112 and 246 ms, and 4 - 5% at TE = 374 ms for both brain regions, as shown in Fig. 4a. The mIns CRLBs were somewhat larger, the mean values being 4, 4, 6 and 9% at TE = 54, 112, 246 and 374 ms, respectively (Fig. 2-4). The mean CRLBs of NAA-Asp were 3, 4, 4 and 5% at the four TEs, respectively. For the NAAG singlet, only the data from the left occipital region gave CRLBs less than 20% at the four TEs (*i.e.*, mean values were 6, 7, 7 and 8, respectively). Compared to left occipital, the data from medial occipital gave much greater CRLBs. The CRLBs were less than 20% only at TEs shorter than 374 ms, at which NAAG estimates were not reliable (CRLB > 50). The NAAG $T_2^{\dagger}$ fitting was therefore performed for left occipital only. The methyl group proton signals of tCr, NAA and GPCPC were all well-defined, giving CRLBs less than 3% at all TEs. Figure 2-4b presents the correlation coefficients between the estimates of Glu and several metabolites having resonances adjacent to the Glu signals. While Glu and Gln showed more or less negative correlations at TE = 246 and 374 ms, the two short TEs gave positive correlations between the metabolites, implying that the Glu and Gln estimation could be influenced by other metabolites, which may include GABA, GSH and macromolecules. At TE = 54 ms, the macromolecule signals may not be attenuated completely, but since the Glu and Gln C4-proton multiplets were not extensively overlapped as indicated in Fig. 1, the covariance between Glu and Gln were similar at TE = 54 and 112 ms. The correlation

coefficients of Glu with respect to other resonances were more or less within ±0.5 at the four TEs, indicating that the Glu signals were estimated without substantial uncertainties due to the neighboring interferences, which may provide Glu T_2 estimation with acceptable precision.

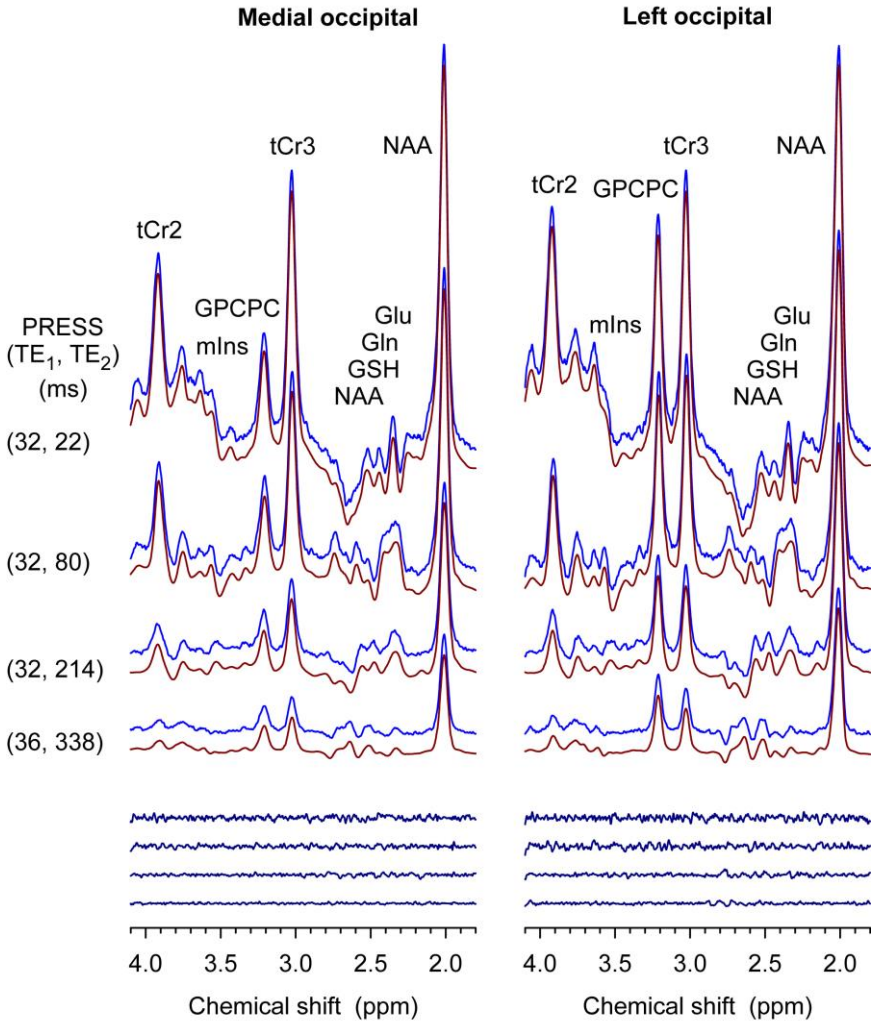

Figure 2-3 LCModel fitting results at the four (TE_1, TE_2) pairs of PRESS.
In vivo spectra at the four (TE_1, TE_2) pairs of PRESS from medial occipital and left occipital cortices of a healthy volunteer (subject 1 in Fig. 2) are shown together with LCModel fits and residuals. The decreasing residual levels with increasing TE are due to the different number of signal averages (16, 32, 64, and 128, top to bottom). Spectra are normalized with respect to the NAA singlet at TE = 54 ms for each voxel.

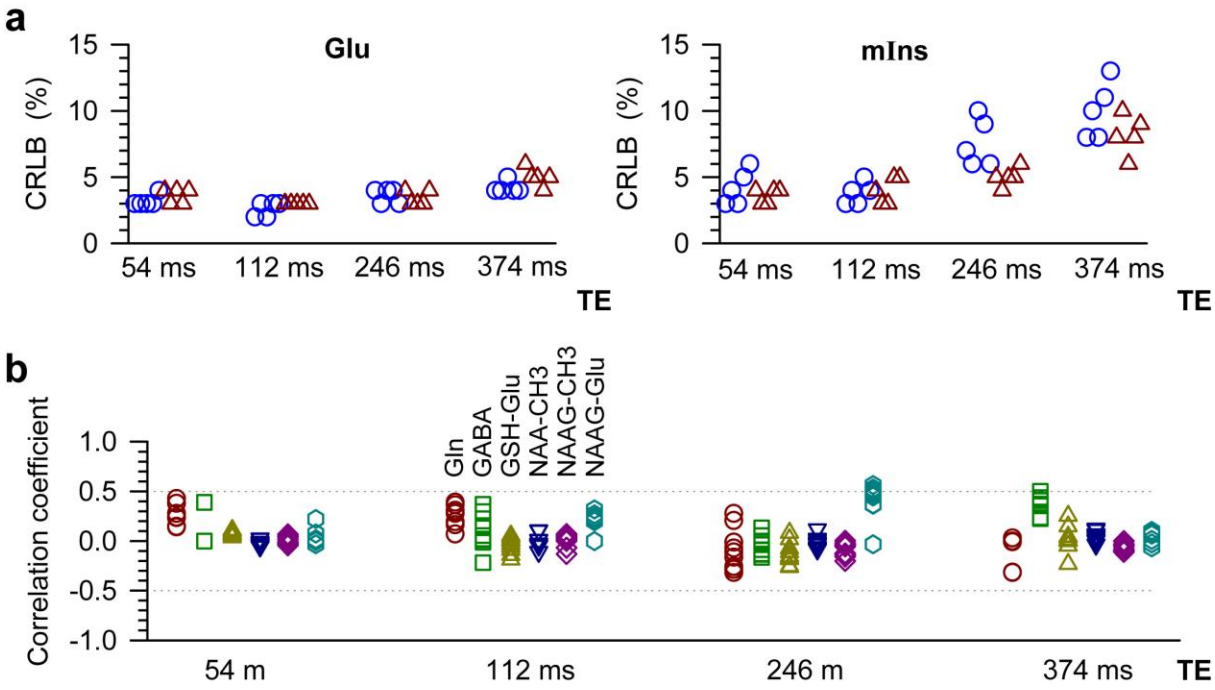

Figure 2-4 CRLBS and Correlation-coefficients of five subjects at four TE's.
(**a**) The CRLBs of Glu and mIns are shown for the four TEs used for $T_2^{\dagger}$ measurement. For each TE, five data points on left (circle) represent CRLBs in spectra from medial occipital, and five data points on right (triangle) from left occipital. (**b**) The correlation coefficients, returned by LCModel, between Glu and metabolites having resonances in the proximity of the Glu signals. The metabolites include Gln (circle), GABA (square), GSH Glu moiety (triangle up), NAA-CH_3 (triangle down), NAAG-CH_3 (diamond), and NAAG Glu moiety (hexagon).

Figure 2-5 illustrates monoexponential fittings for several metabolite signals for the spectra from subject 1 shown in Fig. 2. The upper panel shows fits of major singlet signals (*i.e.*, tCr-CH_3, tCr-CH_2, NAA and GPCPC) and the lower panel shows Glu, mIns, NAA-Asp, and NAAG. The signal decay *vs.* TE was well represented by a monoexponential function, giving coefficients of determination (R^2) of monoexponential fitting close to unity. Table 1 shows mean $T_2^{\dagger}$ and R^2 of the metabolites and *p* values from paired t-tests (uncorrected and Bonferroni corrected) for the $T_2^{\dagger}$ values between the medial occipital and left occipital

regions. The $T_2^\dagger$ of Glu was measured to be 181±16 and 180±12 ms (mean±SD, N = 5) for medial occipital and left occipital, respectively. The mIns $T_2^\dagger$ was estimated as 197±14 and 196±17 ms, respectively. For these coupled-spin metabolites, the $T_2^\dagger$ was measured to be very similar between the two regions ($p > 0.8$). The Glu and mIns data were well fitted with a monoexponential function for both regions, with $R^2 \approx 0.99$ and 0.97, respectively. The $T_2^\dagger$s of tCr-CH_3, tCr-CH_2 and GPCPC were measured to be ~150, ~120 and ~230 ms for both regions, respectively. The $T_2^\dagger$ of the NAA singlet was observed to be ~260 and ~310 ms for medial occipital and left occipital, respectively. The difference was statistically significant ($p = 0.008$; paired t-test). The $T_2^\dagger$ of the NAA-Asp CH_2 resonances was also observed to be quite different between the regions (~220 and ~280 ms, respectively; $p = 0.009$). The reliability of the $T_2^\dagger$ fitting of this NAA multiplet was low, as indicated by large standard deviations and relatively small R^2 values. The *p*-values from Bonferroni correction for NAA and NAA-Asp were close to 0.05, indicating statistical evidence for the presence of relaxation time differences between the two regions. The $T_2^\dagger$ of the NAAG singlet was measured as ~290 ms for the left occipital region, with mean R^2 of 0.934. In addition, the brain water $T_2^\dagger$ was estimated using the unsuppressed water signals acquired with PRESS. The water signals did not exhibit a monoexponential TE dependence consistently, primarily due to the long T_2 effects of the CSF water. Thus, the water signals at TE = 54, 112, and 246 ms only were used for $T_2^\dagger$ estimation, giving $T_2^\dagger$ of ~83 ms for both medial and left occipital, as shown in Table 2-1.

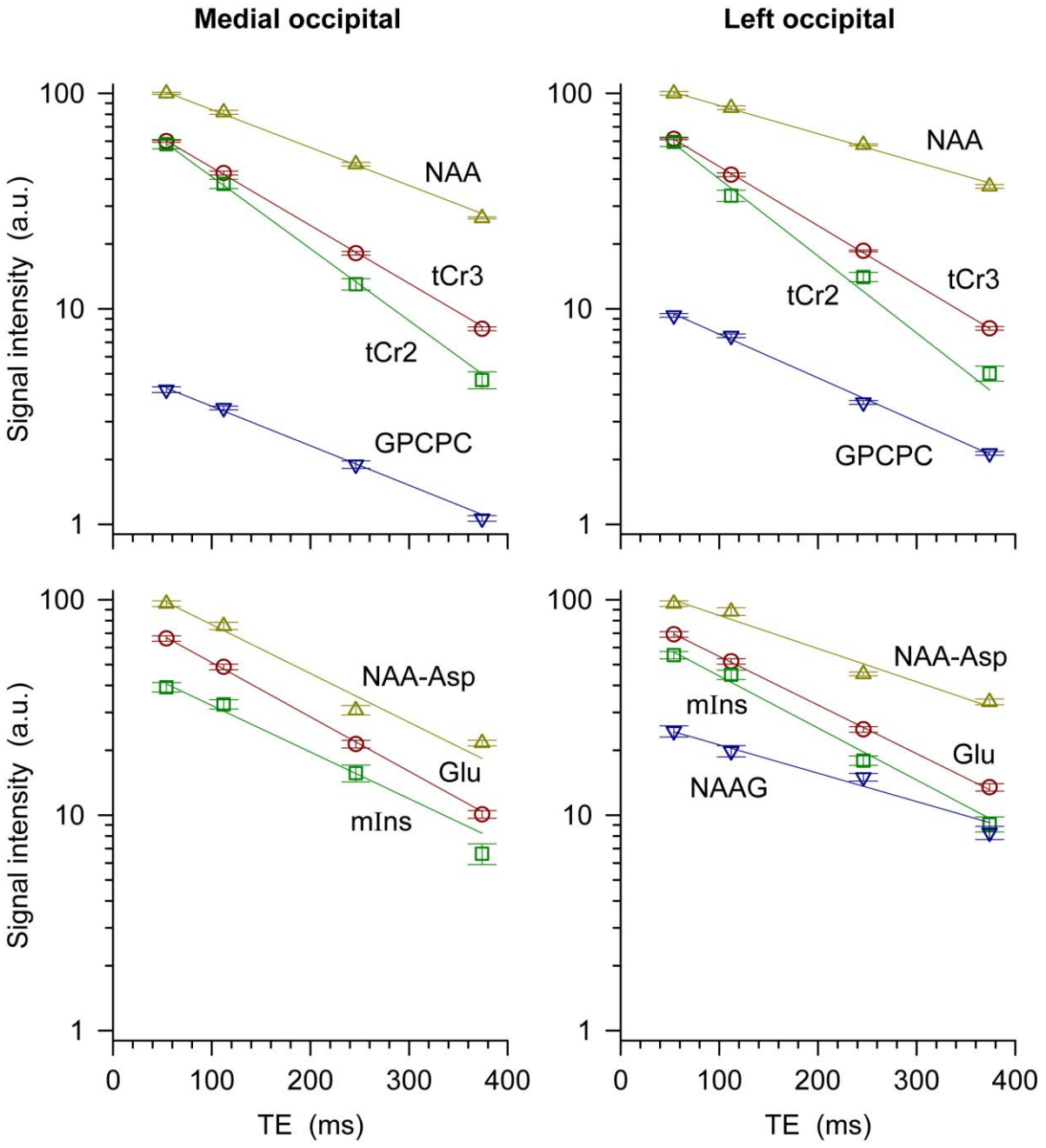

Figure 2-5 Monoexponential fitting of LCModel estimates *vs.* four TE's.
Monoexponential fitting of LCModel estimates *vs.* TE (= TE_1 + TE_2) for the medial occipital and left occipital lobes. The upper panel shows fits of major singlet signals (tCr-CH_3, tCr-CH_2, NAA and GPCPC) and the lower panel shows fits of major multiplets (Glu, mIns and the NAA aspartate moiety) and the NAAG singlet (left occipital only). Error bars indicate the standard deviation of the LCModel estimates.

	Medial occipital		Left occipital		Paired t-test	Bonferroni corrected
	$T_2^\dagger$ (ms)	R^2	$T_2^\dagger$ (ms)	R^2	*p*	*p*
tCr-CH_3	147±10	0.998	156±7	0.998	0.0839	0.5873
tCr-CH_2	124±6	0.998	123±11	0.998	0.8730	1
NAA	258±11	0.995	309±16	0.989	0.0078	0.0545
GPCPC	241±13	0.981	224±15	0.993	0.2169	1
Glu	181±16	0.996	180±12	0.994	0.8809	1
mIns	197±14	0.977	196±17	0.983	0.9342	1
NAA-Asp	222±33	0.986	284±23	0.963	0.0094	0.0657
NAAG	-	-	292±35	0.934	-	-
Water	83±7	0.998	83±5	0.999	0.9884	-

Table 2-1 Apparent T_2 (T_2†) values and the coefficients of determination (R^2).
Apparent T_2 ($T_2^\dagger$) values and the coefficients of determination (R^2) of monoexponential fitting of metabolites and water data from the medial occipital and left occipital cortices are shown together with *p*-values for $T_2^\dagger$ differences between the two brain regions. The Bonferroni-corrected *p*-values were obtained by multiplying the uncorrected *p*-values by the number of metabolites (*i.e.*, 7, excluding NAAG). When the Bonferroni-corrected *p*-value was greater than one, the *p* value was set to 1. The water $T_2^\dagger$ was estimated from the signals at TE = 54, 112, and 246 ms. $T_2^\dagger$ and R^2 are mean±SD (N=5).

2.4 DISCUSSION

The present study reports apparent T_2 values of brain metabolites, including Glu, mIns, NAA-Asp, and NAAG, in addition to the major singlets. The signal intensity and

spectral pattern of coupled-spin metabolites vary with changing TE due to the effects of J evolution as well as the transverse relaxation. Therefore, when basis spectra that include the J evolution effects are used for spectral fitting on multi-TE data, the relaxation time constant can be obtained directly from the TE dependence of the spectral fitting estimates. Moreover, for spectra obtained with PRESS volume localization, the signals of coupled resonances are largely affected by the 180° pulses. The effects of the finite bandwidth and imperfect refocusing profile have to be taken into account to evaluate the scalar coupling effects on the signals. This was accomplished incorporating the actual RF pulse waveforms in calculating the basis spectra in the present study.

The four TEs used in this study appear to be reasonably optimal for $T_2^{\dagger}$ estimation of Glu and mIns in the human brain. Although the shortest TE (54 ms) may not be sufficiently long for complete suppression of macromolecule signals, spectral fitting using precisely-calculated basis spectra differentiated effectively the metabolite signals from the residual macromolecule signals, leading to Glu and mIns CRLBs smaller than those at short TEs in prior studies at the same field strength (87,88). At long TEs, the metabolite signals were attenuated substantively, but using the proper basis spectra the CRLBs of Glu and mIns of the present study were comparable to those of the prior short-TE studies ($\leq$ 10%). The resonances of Gln are proximate to the Glu resonances, but the Gln signals were resolvable with CRLB < 20% at TEs 54, 112, and 264 ms (mean CRLB = 12±4%, 11±4%, and 8±3% (n = 10), respectively). The Gln signal at TE = 374 was not properly measurable (CRLB > 100%) likely due to the insufficient SNR. Given that the precision of signal estimates is governed by SNR and critical for relaxation time estimation, measurements at the four TEs

with various number of averages allowed us to achieve acceptable precision of LCModel estimates and $T_2^{\dagger}$ values for several J-coupled metabolites, as indicated by the R^2 values comparable to those in recent T_2 studies with greater number of TEs (76,78,81). Despite the increased number of signal averaging at the long TE (128 averages), the CRLBs of mIns at TE = 374 ms were relatively large (9.1±2.0%, N=10) due to the extensive signal degradation arising from the J coupling effects (Figure 2-4).

The estimated $T_2^{\dagger}$ values of the present study may well be apparent relaxation time constants, presumably specific to the PRESS sequence used. With the changing inter-RF pulse delays for multi-TE measurements, the relaxation estimates may include the effects of spin-spin relaxation (T_2) and molecular diffusion under the field gradients created by magnetic susceptibility distribution, thereby resulting in $T_2^{\dagger} < T_2$. The T_2 of brain metabolites may be measured employing constant, short inter-RF pulse delays in multi-TE scans *in vivo* (75). In the present study, signal reduction due to diffusion under spoiling gradient pulses may be minimal and equal at all TEs since the diffusivity of metabolites in the human brain is low ($< 0.3\times10^{-7}$ m^2/s) (89) and and the inter-gradient pulse intervals were relatively short (~17 ms) and kept constant in the multi-TE scans. The molecular diffusion effects associated with the pulsed field gradient pulses may therefore be negligible in our relaxation estimates. In addition, the use of constant TR of 3 s for the multi-TE scans may lead to relaxation estimates shorter than the T_2. However, this effect does not seem substantial. The trajectory of the longitudinal magnetization in the steady-state condition ($TR < 5\times T_1$) is varied with changing TE, resulting in unequal initial longitudinal magnetization prior to the 90° excitation in multi-TE scans (90). Assuming that for a PRESS

sequence the ratio of the steady-state initial longitudinal magnetization to the thermal equilibrium magnetization is given by $1 - E_{TR} + 2E_{TR}E_1 - 2E_{TR}E_2$, where $E_{TR} = exp(-TR/T_1)$, $E_1 = exp((TE_1/2)/T_1)$, and $E_2 = exp((TE_1 + TE_2/2)/T_1)$, the $T_2^\dagger$ estimates can be corrected for constant-TR effects using known T_1 values. For published T_1 of ~1.2 s for Glu and mIns at 3T (74,76), the steady-state constant-TR effect on the $T_2^\dagger$ estimates of the present study is predicted to be only 1.5% compared to $T_2^\dagger$ estimates from TR » T_1. For tCr and NAA with T_1 of ~1.4 s, the discrepancy may be 1.6%.

Prior studies of relaxation time measurements for brain metabolites indicated consistently that $T_2^\dagger$ of the NAA singlet differs between gray and white matter (74,76,78,79). The $T_2^\dagger$s of the NAA singlet from the medial occipital and left occipital regions in the present study were similar to those of the prior studies for occipital GM and WM (74,76), indicating that GM and WM were dominant in the voxels positioned in the medial occipital and left occipital cortices in the present study, respectively, in agreement with the GM, WM and CSF estimates shown earlier. The NAA-Asp CH_2 multiplet also showed $T_2^\dagger$ longer in left occipital than in medial occipital, most likely due to the different fractions of GM and WM within the voxels. The NAA-Asp $T_2^\dagger$ was measured separately from the NAA singlet. While it is necessary to individually fit the subgroups of metabolites to take into account possible differences in relaxation times between resonances within a metabolite, this approach may decrease the precision of spectral fitting. The NAAG signals from the left occipital region were measurable with CRLB < 20% at the four TEs, most likely because of its relatively high concentration in WM compared to that in GM, as indicated by prior studies (91,92). For the medial occipital cortex, CRLB of NAAG was less than 20% at TEs other than the longest TE

in 4 subjects. Monoexponential fitting of the data at the three TEs gave an NAAG $T_2^\dagger$ of 252±49 ms, implying that the NAAG relaxation time may differ between GM and WM, similarly to NAA.

The $T_2^\dagger$ of Glu in the GM and WM dominant regions in the human brain was estimated to be about the same in the present study (180 ms), similarly to a prior study (80), but somewhat shorter than the previously reported value (200 ms). Although the investigated brain regions differ (occipital *vs.* frontal), given that the metabolite $T_2^\dagger$ estimation depends on the number of refocusing RF pulses (75), the difference in Glu $T_2^\dagger$s from the two studies may be in part due to the difference in the effects of inter-RF pulse molecular diffusion during the sequences (dual refocusing *vs.* triple refocusing). Presumably for a similar reason, the tCr-CH_3 $T_2^\dagger$ was shorter in the present study (~150 ms) than in the prior triple-refocusing study (~165 ms). In the present study, Glu $T_2^\dagger$ was measured to be much shorter than NAA-CH_3 $T_2^\dagger$ (~290 ms). The large $T_2^\dagger$ difference between Glu and NAA was also the case in phantom solutions (~700 *vs.* 1200 ms). These *in vivo* and phantom results may be as expected given that the CH_2 protons (Glu) are most likely less mobile than the CH_3 protons (NAA) and consequently the motional averaging of the dipole-dipole interaction occurs less in Glu than in NAA. In the brain, Glu and NAA are largely present within neuronal cells and the intra-molecular dipolar interaction may be a dominant mechanism for T_2 relaxation in both Glu and NAA. However, for tCr, the $T_2^\dagger$ (3.02 ppm) was shorter than the NAA-CH_3 $T_2^\dagger$ in many prior studies (71-79) and in the present study. This may not be due to the difference in the diffusion-induced dynamic dephasing since the diffusion constants of tCr and NAA are similar (93-95). The relatively short $T_2^\dagger$ of tCr may be a result of tCr-to-water magnetization

transfer occurring *via* immobile proton pools (96,97). Since in all prior and present T_2 studies the data were acquired following water suppression (*i.e.*, creation of large magnetization difference between the tCr and water proton pools with respect to their thermal equilibrium values), the tCr signals may undergo further relaxation with increasing TE in addition to the relaxation caused by the intra-molecular dipolar interaction, thereby leading to reduced $T_2^{\dagger}$, shorter than that of Glu $T_2^{\dagger}$, as in the present and prior Glu T_2 studies. The tCr $T_2^{\dagger}$ may become longer when measured without water suppression. In phantom solutions, in which the magnetization transfer is not present, the Cr-CH_3 and NAA-CH_3 $T_2^{\dagger}$s are similar due to the similarity in their dipolar interaction strength. For the brain water (excluding CSF), the $T_2^{\dagger}$ was measured to be short (~80 ms) compared to metabolite $T_2^{\dagger}$ because of the strong intra-molecular interactions and the high diffusivity in water (93-95).

In conclusion, we have demonstrated measurement of apparent proton T_2 of coupled-spin metabolites in the human brain using a PRESS sequence at 3T *in vivo*. The signals of brain metabolites, including Glu, mIns and NAAG, were resolved, for the GM-dominant medial occipital and WM-dominant left occipital regions, at four selected echo times using spectral fitting with numerically calculated basis spectra. Further studies will be required to determine variations in relaxation times across brain regions and in disease conditions.

CHAPTER THREE
In vivo ^{1}H MR Spectroscopic Imaging of Glycine in Healthy Brain and Gliomas at 3T

3.1 INTRODUCTION

3.1.1 Literature review

Glycine (Gly), a non-essential amino acid, is a post-synaptic inhibitory neurotransmitter and acts as co-agonist of glutamate on N-methyl D-aspartate receptors (34,98). It is a precursor for the synthesis of proteins and is a primary source of one-carbon units in cellular metabolism (36). Gly is derived from serine, as a product of the Gly, serine and threonine metabolism pathway, and is hypothesized to reside in two separate pools, i.e., metabolic and transmitter pools (36,99). Recent studies indicate abnormal Gly levels in a wide range of brain tumor subtypes (5,41,43-45,100-102) including gliomas, as well as a variety of cancer cell lines (103). Thus Gly may be a biomarker for primary as well as metastatic brain tumors. Given the cellular heterogeneity as well as regional variations in metabolic alterations (104-106) in brain tumors, imaging of Gly may have important clinical application in the management of patients with brain tumors.

Gly has two uncoupled co-resonating protons, giving rise to a singlet at 3.55 ppm (82). *In vivo* detection of Gly using ^{1}H MRS in the human brain is challenging primarily due to the presence of the overlapping multiplets of myo-inositol (mIns), whose concentration is much higher (5 - 7 fold) than the Gly concentration in normal physiological conditions (5,40,44,107). Thus good suppression of the mIns multiplet in the proximity of the Gly resonance is essential for reliable detection of Gly. Several single-voxel localized MRS

approaches were proposed to overcome the spectral complexity in Gly measurement, which include TE averaging (107) and triple refocusing (108) at 3T, and short-TE single-spin echo (40) and long-TE PRESS (point-resolved spectroscopy) methods (44) at 7T. Prior *in vivo* studies for Gly elevation in brain tumors used single-voxel localized MRS (5,100) and multi-voxel MRS imaging (41,45). While single-voxel MRS is technically simple and may be preferable for precise measurement of Gly, given the high heterogeneity of brain tumors (104-106) and the presence of regional variation of Gly levels in the normal human brain (44), applicability of Gly spectroscopic imaging is very high.

3.1.2 Aim of the project

To measure Gly in the human brain at 3T with ^{1}H MR spectroscopic imaging, using Gly-optimized PRESS TE = 160 ms scheme (5). To investigate the regional variations of Gly in healthy brain with linear regression analysis, effect of linewidth, and signal-to-noise on reliable estimation of Gly. To study potential variations of Gly levels in human gliomas.

3.2 MATERIALS AND METHODS

3.2.1 Experimental setup

MR experiments were carried out on a 3.0 T whole-body scanner (Philips Medical Systems, Best, The Netherlands), equipped with an integrated body coil for radio-frequency (RF) transmission and an 8-channel phased-array coil for signal reception.

3.2.2 MR Spectroscopy acquisition details

^{1}H MR spectroscopic imaging (SI) data were obtained using phase encoding gradients within a PRESS sequence for spatial localization. The volume of interest (VOI) was prescribed by the PRESS sequence with TE = 160 ms (TE_1 = 60 ms and TE_2 = 100 ms). The PRESS sequence included 9.8 ms 90° (along the anterior-posterior direction) and 13.2 ms 180° (along the left-right and head-foot directions) RF pulses, with bandwidths of 4.2 and 1.3 kHz, respectively, at an RF field intensity of 13.5 μT.

3.2.3 Phantom experiments

Validation experiments were performed on a 10 cm diameter spherical phantom that contained Gly, mIns and creatine (Cr) at 1.1 mM, 10 mM and 8 mM, respectively. Phantom SI data were obtained with a 32 × 32 data matrix with a field of view (FOV) of 160 × 160 mm^2, VOI of 50 × 50 mm^2, using a TR of 3000 ms and four signal averages. For comparison with SI data, single-voxel spectroscopy (SVS) data were obtained from a voxel size of 10x10x10 mm^3, using a TR of 3000 ms and 256 signal averages.

3.2.4 *In vivo* studies

For *in vivo* experiments in healthy volunteers, the MR protocol included survey imaging followed by a T_1-weighted high-resolution sagittal Magnetization Prepared RApid Gradient Echo (MPRAGE, TE/TI/TR= 3.8/875/1360 ms, 160 slices with 1 mm thickness, 256×256×160 mm^3 field of view) sequence. For gliomas, the MR protocol included survey imaging followed by T_2-weighted fluid attenuated inversion recovery (T_2w-FLAIR) imaging (TR/TE/TI = 11000/125/2800 ms, FOV = 230 × 230 mm^2, slice thickness of 5 mm, 28 slices along each of transverse and sagittal directions) for tumor identification.

For SI data acquisitions, a PRESS-prescribed transverse slice was positioned to cover the region of interest with spatial resolution of 10 × 10 mm^2 and slice thickness of 15 mm. In each SI scan, a 20 × 16 data matrix was obtained from a 200 × 160 mm^2 FOV. A vendor-supplied 2D elliptical k-space sampling scheme was used (109), to reduce the acquisition time by ~30%. Each k-space point with 1024 complex points was acquired with two averages at TR = 1.2 s and spectral width = 2000 Hz. The SI data were reconstructed with 2D Fourier transformation of the k-space data, after zero filling the non-acquired k-space points and zero-padding the data matrix to two fold along each phase encoding direction (*i.e.*, 40 × 32) to obtain spatial resolution of 5 × 5 mm^2. The PRESS RF pulses were tuned to 3 ppm which is halfway between the N-acetylaspartylglutamate 4.6 ppm and lactate 1.3 ppm resonances. Water suppression was performed using a four RF-pulse scheme (110). In healthy brain a VOI of 80 × 80 mm^2 was positioned to cover the central brain region above the corpus callosum and for tumor scans the VOI included the tumor mass as well as normal-appearing brain regions. Four outer volume suppression bands were placed in the periphery of the VOI to minimize potential contamination from extracranial lipids and water outside the VOI. First- and second-order shimming was carried out on VOI using FASTMAP (85). To minimize motion artifacts, foam pads were placed to restrict head motions inside the reception coil. The scan time of a single SI acquisition was approximately 10 minutes.

3.2.5 Post-processing, analysis and quantification of SI data

During post-processing, residual water signals were further minimized using a singular value decomposition algorithm in jMRUI (5,6,41,111). A 1-Hz exponential function

was multiplied to FIDs prior to Fourier transformation, in order to suppress potential distortions in the later part of the FIDs. Correction for spatial B_0 was performed using in-house programs written in MATLAB® (MathWorks Inc., Natick, MA, USA). The FIDs were zero filled to 4096 points and spectra were analyzed with LCModel (Version 6.3) (86,112) using numerically simulated basis sets, which were calculated according to a published method (6). The basis function included simulated spectra of sixteen brain metabolites; Gly, mIns, tCr (creatine + phophocreatine), tNAA (N-acetylaspartate + N-acetylaspartylglutamate), tCho (phosphocholine + glycerophosphocholine + free choline), glutamate, glutamine, γ-aminobutyric acid, glutathione, lactate, alanine, taurine, scyllo-inositol, aspartate, phosphoethanolamine, and serine. Spectral fitting was undertaken between 0.5 - 4.1 ppm. For validation purpose, additional LCModel fitting was performed without Gly in the basis sets. For estimation of mIns, tCr, and tCho concentrations, the transverse relaxation effects were corrected using published T_2 values of 200, 150, and 230 ms, respectively (5,113). The T_2 of Gly was assumed to be equal to the mIns T_2. Metabolite estimates in molar concentrations (mM) were then obtained with reference to tCr in white matter regions at 6.4 mM (114-118), ignoring potential difference in T_1 saturation effects between metabolites in healthy brain and tumors. The linewidth (FWHM) estimates were obtained from the LCModel output. Maps of metabolite estimates and Cramér-Rao lower bounds (CRLB) for the VOI were generated. The maps (e.g. matrix of size 16 × 16) were then interpolated 10 fold (e.g. 160 × 160) using the nearest neighbor method. The correction for the chemical shift displacement effects was performed by shifting the metabolite matrix grid according to the ratio of the chemical shift difference of metabolite resonances from the

PRESS RF carrier frequency (3.03 ppm) with respect to the PRESS RF pulse bandwidths. For this, a major resonance was chosen for each metabolite based on the highest signal selectivity. The major resonance used was 3.55, 3.62, 3.21, and 3.03 ppm for Gly, mIns, tCho, and tCr, respectively. For Gly, the chemical shift displacement of the VOI was 2% and 5% along the anterior-posterior (selected by the 90° pulse) and left-right directions (selected by the 180° pulse), respectively. After the shift, the matrix grid was reduced to the original matrix size by averaging over 10 × 10 pixels. In case of healthy brain data, the central 13 × 13 grid was selected for analysis of GM and WM linear regression and to generate average metabolite maps.

For healthy brain data only, gray and white matter (GM and WM) segmentation was performed on MPRAGE images using SPM 5. Fifteen slices of MPRAGE corresponding to an SI slab were selected from the segmented images and averaged to obtain the GM, WM and CSF contents within each of the SI voxels. Metabolite concentrations from healthy brain data were corrected for cerebrospinal fluid contamination (119). To obtain the metabolite concentrations in pure GM and WM, the tissue concentration of metabolite was fitted with a linear function of fractional GM content, f_{GM} = GM/(GM+WM), individually for each of the subjects, and subsequently the intercepts at f_{GM} = 0 and 1 were averaged over the 8 subjects.. Paired two tailed t-tests were conducted for comparing the metabolite concentrations and CRLBs between pure GM and WM in the healthy brain. For tumor data, paired and unpaired two-tailed t-tests were used to compare the metabolite levels between tumors and normal-appearing brain and between tumor grades. Statistical significance was declared for p-value ≤

0.05. All statistical analyses were conducted using software SAS 9.3 (SAS Institute, Gary, NC).

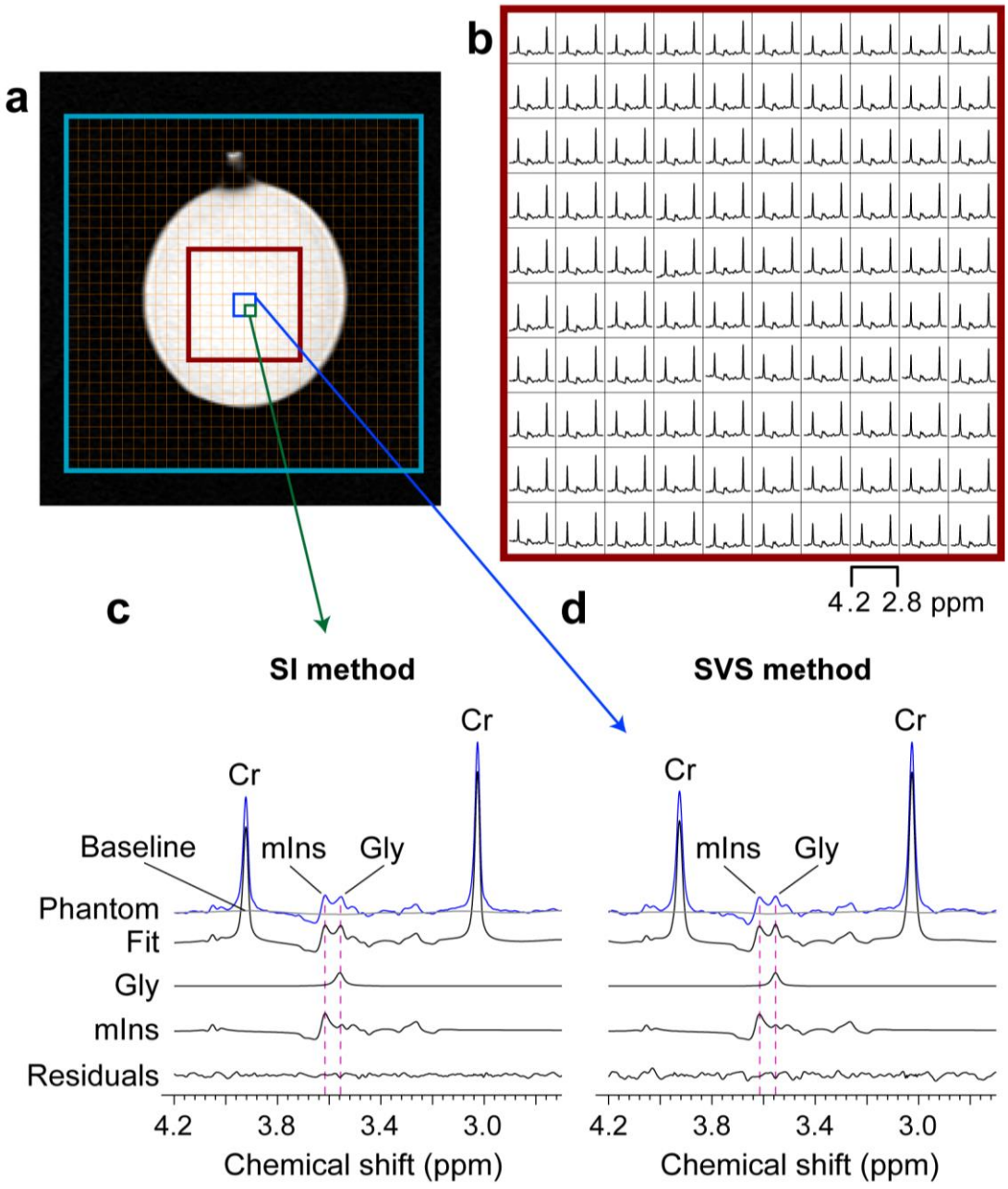

Figure 3-1 SI and SVS data were acquired with PRESS TE = 160 ms from a phantom containing Gly (1.1 mM), mIns (10 mM) and Cr (10.0 mM).
(a) The FOV (blue line; 160 × 160 mm^2) and VOI (brown line; 50 × 50 mm^2) are shown in a gradient echo image. Fine grids indicate the individual voxels of the SI. (b) Spectra from the

VOI are presented between 2.7 and 4.2 ppm. (c,d) SI and SVS spectra and LCModel fitting results. Vertical dashed lines are drawn at 3.55 and 3.62 ppm. Data were acquired using a TR of 3000 ms. The SI data were acquired with a single average for each k-space point, while the SVS spectrum was acquired with 256 signal averages. The spectra are broadened to singlet linewidth of ~3 Hz.

3.3 RESULTS

3.3.1 Phantom experiments

The PRESS (TE_1, TE_2) = (60, 100) ms method was tested in a phantom solution with Gly and mIns for both SI and SVS acquisitions. The multiplet of mIns at ~3.55 ppm was substantially attenuated, affording good separation of the Gly singlet from the mIns background signal (Figure 3-1c and 3-1d). For a prepared mIns-to-Gly concentration ratio of 10/1.1 and a singlet linewidth (FWHM) of 3 Hz, a computer simulation of 90°-acquisition indicated that the largest peak of mIns at ~3.55 ppm is 9.5 fold greater than the Glysignal. The peak amplitude of mIns in the phantom was decreased by 17 fold at TE = 160 ms when compared to 90°-acquisition and consequently the mIns-to-Gly peak amplitude ratio at 3.55 ppm was 0.57. This mIns signal suppression occurred similarly in SI and SVS data, and the Gly+mIns composite signal pattern was about the same between SI and SVS. The Gly and mIns signals were well reproduced by LCModel fitting, with uniform residuals between 2.7 and 4.2 ppm in both SI and SVS. Following the correction for transverse relaxation effects using measured phantom T_2's of Gly (1.5 s) and mIns (0.75 s), the Gly and mIns concentrations were estimated as 1.1 and 10.2 mM, respectively. T_2 of mIns was obtained by fitting phantom data with the simulated signal of mIns at various echo times.

3.3.2 Healthy Brain Studies

The PRESS TE = 160 ms SI method was evaluated for imaging of Gly in healthy brain. Figure 2 shows representative data from a healthy subject. For an SI slab positioned above the corpus callosum (Figures 3-2a and 3-2b, blue line), the spectra within a 65×65 mm^2 volume (Figure 3-2b, brown line) showed well defined metabolite signals without substantial baseline distortions (Figure 3-2c). Two spectra from GM and WM dominant regions were analyzed using basis sets with and without Gly (Figures 3-2d and 3-2e). In the spectral fitting with a basis set with Gly the *in vivo* spectra were closely reproduced by the fit. In the spectrum from the GM dominant region (Figure 3-2d), the signals of Gly (3.55 ppm) and mIns (3.62 ppm) were readily discernible, similarly as in the phantom data (Fig. 1c). The Gly level was estimated to be 0.8 mM with CRLB of 9%, and the mIns was 9.2 mM with CRLB of 4%, after CSF correction and normalization of tCr in white matter region to 6.4 mM. When Gly was excluded from the basis set, residual signals were clearly present at ~3.55 ppm, indicating that the signal at 3.55 ppm was primarily attributed to Gly. The absence of Gly in the basis set influenced mIns estimation, resulting in higher estimate (11.0 mM). In contrast, spectra from WM dominant region (Fig. 2e) gave lower estimate of Gly (0.3 mM) and mIns (6.2 mM), with larger CRLBs compared to the data from the GM dominant region. The residual difference between the fittings with and without Gly was relatively small in spectrum from WM region. The linewidth of the spectra from GM and WM dominant regions were 5.7 and 5.6 Hz, respectively. The LCModel returned SNRs of the spectra were very similar between the fittings with and without Gly (*i.e.*, 50 *vs*. 49 for GM and 45 *vs*. 45 for WM).

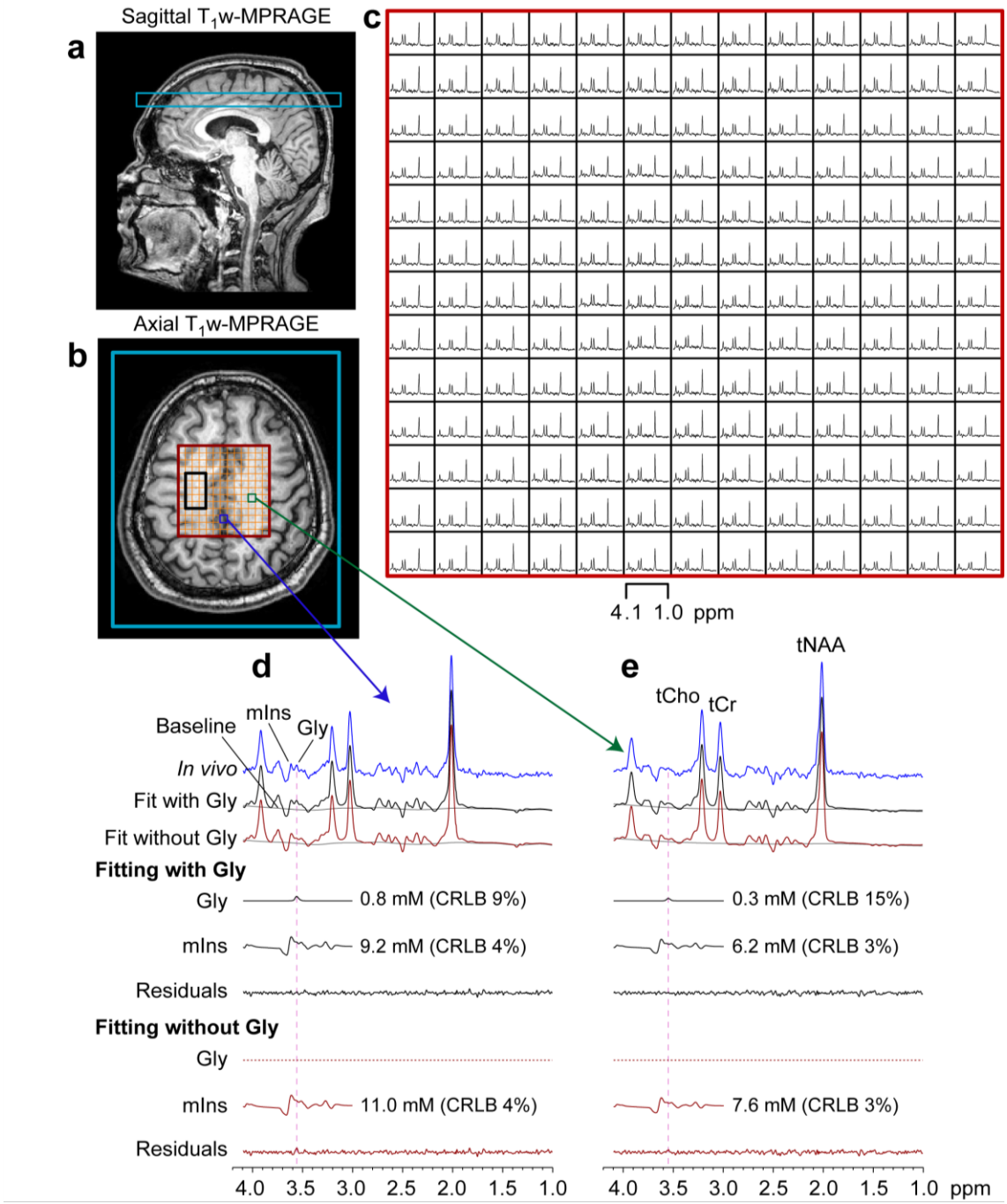

Figure 3-2 Representative 1H SI data from a healthy volunteer.
(a, b) The FOV (blue line) and VOI (brown line) of the SI are shown in T_1w-MPRAGE images. The VOI was prescribed by PRESS localization (TE = 160 ms). Fine grids indicate the individual voxels of the SI. The mean tCr estimate over the voxels within a red line was set to 6.4 mM after CSF correction and used as reference for metabolite quantification. (c) Spectra from voxels within the VOI are shown between 4.1 to 1.0 ppm. (d, e) Spectra from a

voxel in the gray matter (blue box) and from a voxel in the white matter (green box) dominant regions are shown together with LCModel fits, baseline, and residuals that were obtained using basis sets with and without Gly. The Gly and mIns signals, returned by LCModel, are shown with the concentration estimates and CRLBs. Vertical lines are drawn at 3.55 ppm.

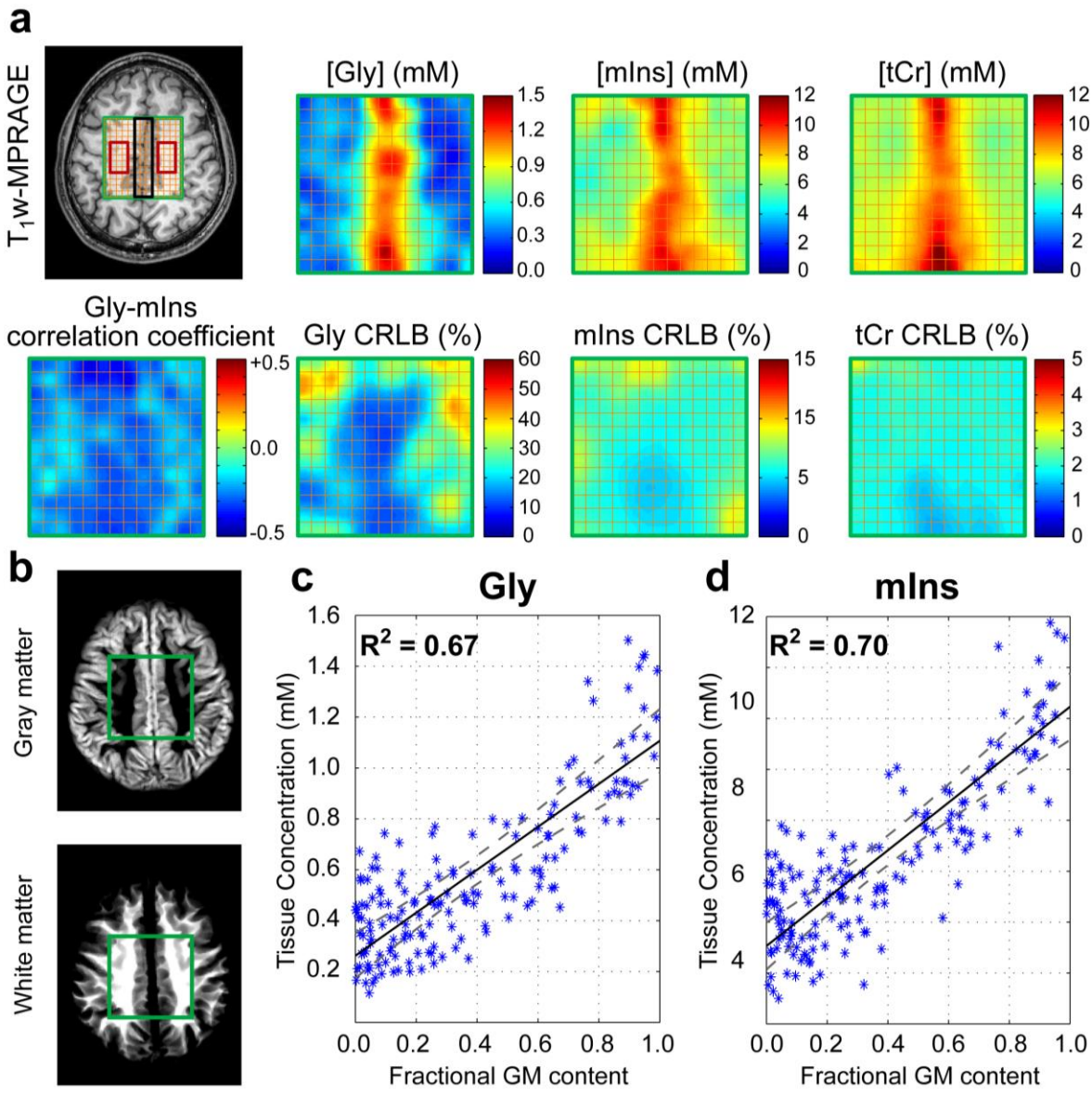

Figure 3-3 Averaged metabolite concentration and CRLB maps.
a) Concentration and CRLB maps of Gly, mIns, and tCr for the VOI (green box in a T_1w-MPRAGE image), averaged over eight healthy volunteers. The maps were smoothened by eight fold using a bi-cubic polynomial function, after the corrections for theCSF contamination and chemical-shift displacement effects. Averaged Gly-mIns correlation

coefficients (returned by LCModel) are mapped on linear scale between –0.5 and 0.5. (b) Gray matter and white matter segmented brain images are shown with the SI VOI. (c, d) Linear regression of Gly and mIns tissue concentrations with respect to fractional GM contents from a single subject. Dashed lines indicate 95% confidence intervals of the linear fit.

Concentration and CRLB maps were averaged over the eight healthy subjects, using axial T_1w-MPRAGE images as anatomical reference. The averaged concentration map of Gly showed regional variations of Gly levels in the brain (Figures 3-3a). The Gly concentration was constantly high in the GM dominant regions along the anterior-posterior midline, whereas the left and right parietal WM-rich regions showed markedly low concentrations of Gly. The Gly concentration was estimated to be 1.0 ± 0.4 mM (mean ± SD, n = 8) for the GM dominant regions (as indicated by a black line Figure 3-3a, regions with GM/(GM+WM) > 80%) and 0.4 ± 0.2 mM for the WM rich regions (red line in Figure 3-3a, regions with WM/(GM+WM) > 95%). The mean CRLBs of Gly and mIns were 16 ± 17% and 9 ± 3% for GM regions, and 24 ± 16% and 6 ± 1% for WM regions, respectively. The Gly CRLBs showed significant difference between GM and WM ($p < 0.001$), while the mIns CRLB difference between the regions was not significant ($p > 0.05$). The mean correlation coefficient between Gly and mIns, returned by LCModel, was –0.31 ± 0.10 and –0.19 ± 0.09 in GM and WM dominant regions, respectively. The negative value of the correlation coefficient was as expected given the equal polarity of the Gly and mIns signals at the echo time used. Figures 3-3c and 3-3d show the linear regression of the Gly and mIns concentrations versus fractional GM content. The Gly and mIns concentrations both increased with fractional GM content. From the y-intercepts at unity and zero fractional GM contents, the concentrations in pure GM and WM were estimated to be 1.1 ± 0.2 and 0.3 ±

0.1 mM for Gly, and 10.2 ± 1.1 and 5.7 ± 1.2 mM for mIns, respectively. The difference of Gly level between pure GM and WM was statistically significant ($p < 0.001$). Similar regional variation was observed in mIns and tCr, with significantly higher concentrations in GM than in WM ($p < 0.001$ for both).

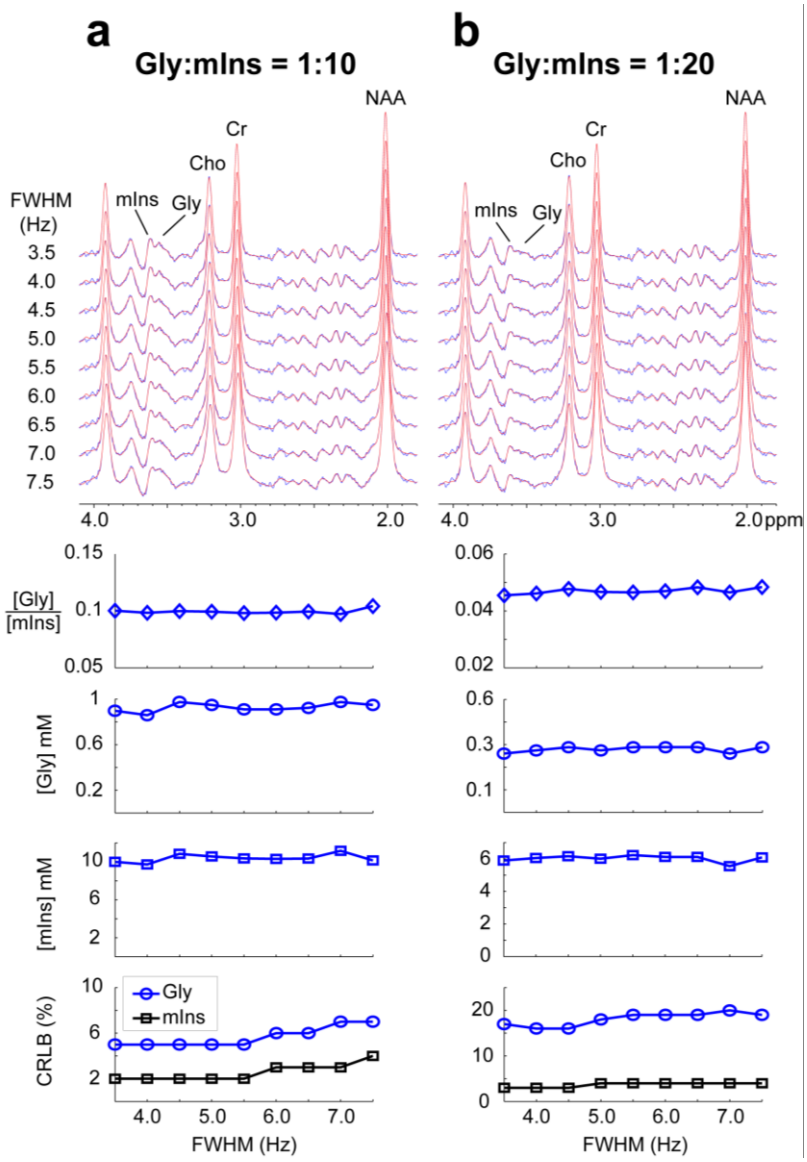

Figure 3-4 Numerically-calculated spectra and LCModel fitting results are shown for Gly-to-mIns = 1:10 (a) and 1:20 (b).
Spectra were broadened to singlet linewidth of 3.5 - 7.5 Hz and random noise was added to the spectra such that the ratio of the NAA singlet amplitude to the noise standard deviation

was 50 for all the linewidths. The metabolites include Gly (1 and 0.3 in (a) and (b) respectively), mIns (10 and 6 in (a) and (b) respectively), NAA (10), Cr (8), Cho (2), Glu (9), and Gln (2), where the numbers in brackets are the concentrations.

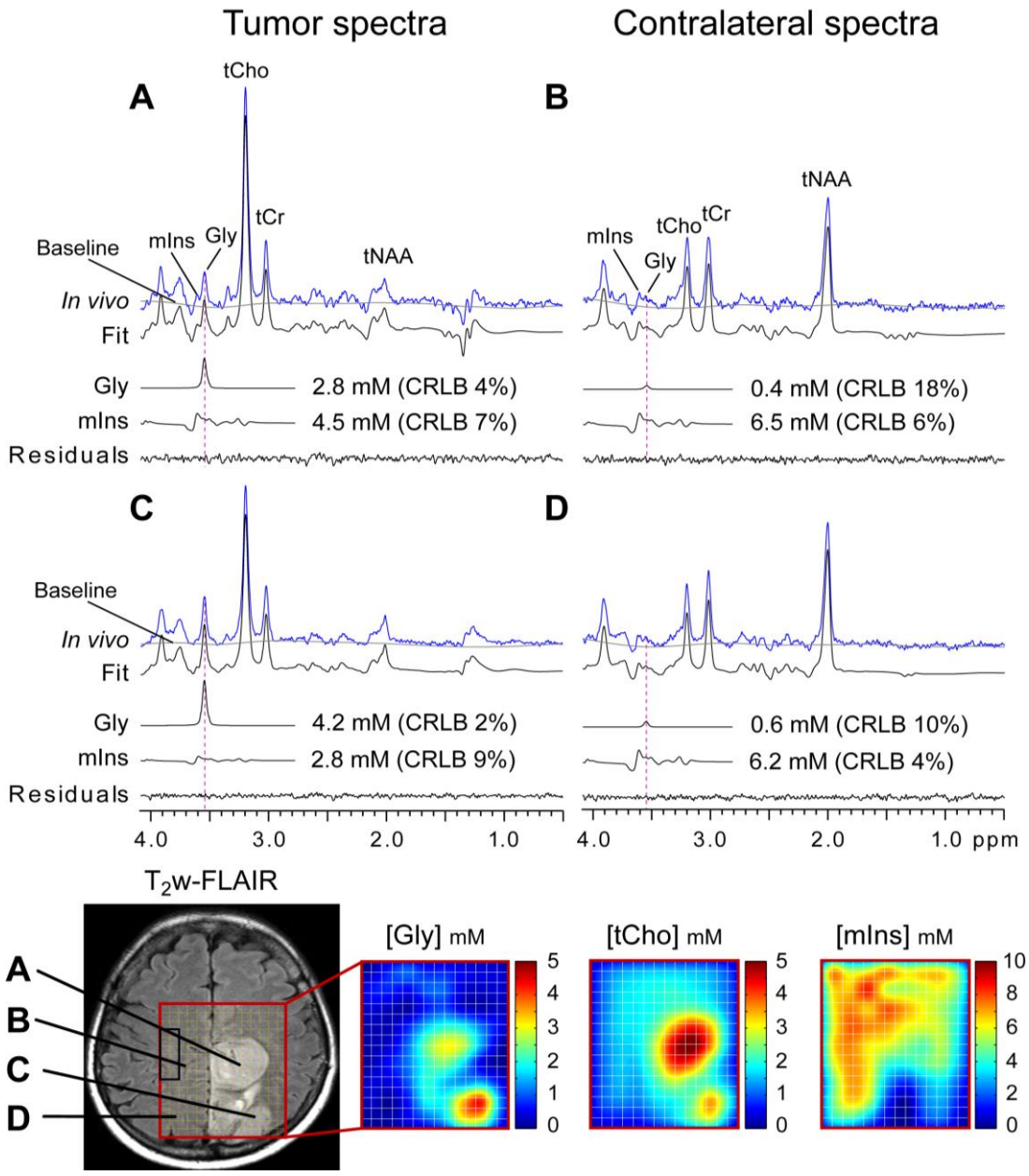

Figure 3-5 SI data from a subject with multi-focal glioblastoma.
Spectra from tumors (labeled A and C) and the corresponding contralateral locations (labeled B and D) are shown together with spectral analysis results. The concentrations of Gly and mIns were estimated with reference to the mean tCr estimate within a black box in the T_2w-FLAIR image at 6.4 mM.

Due to the small spectral distance between the Gly singlet (3.55 ppm) and the largest peak of mIns at (3.62 ppm), detection of the small Gly signal in healthy brain may depend on linewidth. The effect of linewidth on Gly detection was investigated with spectral fitting on simulated spectra with various linewidths (Figure 3-4). Simulation included Gly, mIns, NAA, Cr, Cho, Glu and Gln spectra. With the linewidth of 4 - 7 Hz in our *in vivo* data, spectra were generated for singlet linewidths of 3.5 - 7.5 Hz. Based on our estimated Gly-to-mIns ratios in GM and WM dominant regions, the simulations were performed with Gly-to-mIns concentration ratios of 1:10 and 1:20 for GM and WM, respectively. The spectral pattern of the Gly+mIns composite signal was well preserved across the linewidth and the Gly signal was constantly discernible. LCModel fitting of the calculated spectra with *in vivo* noise level reproduced the Gly and mIns concentrations used for generating the spectra. The Gly-to-mIns estimated ratio was 0.099 ± 0.002 and 0.047 ± 0.001 for simulated Gly-to-mIns concentration ratios of 1:10 and 1:20, respectively. Gly and mIns estimates were within 5% of the true values. The Gly CRLBs were 6 ± 1 and 18 ± 2 for Gly-to-mIns ratio of 1:10 and 1:20, respectively.

3.3.3 Glioma studies

The PRESS SI method was used to acquire data from fourteen subjects with gliomas. Figure 3-5 shows data from a subject with glioblastoma (grade IV), in which T_2w-FLAIR imaging identified two distinct lesions in the left mid-to-posterior brain. Spectra from the two lesions (labeled A and C in Figure 3-5) showed a large singlet like signal at 3.55 ppm with a much smaller signal at 3.62 ppm, compared to the contralateral normal brain (labeled B and D). Spectral analyses of the data showed that Gly was higher in the posterior lesion (labeled

C; 4.2 mM) than in the other lesion (labeled A; 2.8 mM). The ratio of the elevated Gly to the contralateral normal Gly level was 9.3 and 7.0 for the posterior and mid brain lesions, respectively. In contrast, tCho was extensively elevated (~5 mM) in the mid brain tumor (labeled A) compared to the other lesion (labeled C; ~3 mM). The variations in the Gly and tCho levels between the lesions were clearly contrasted in the concentration maps.

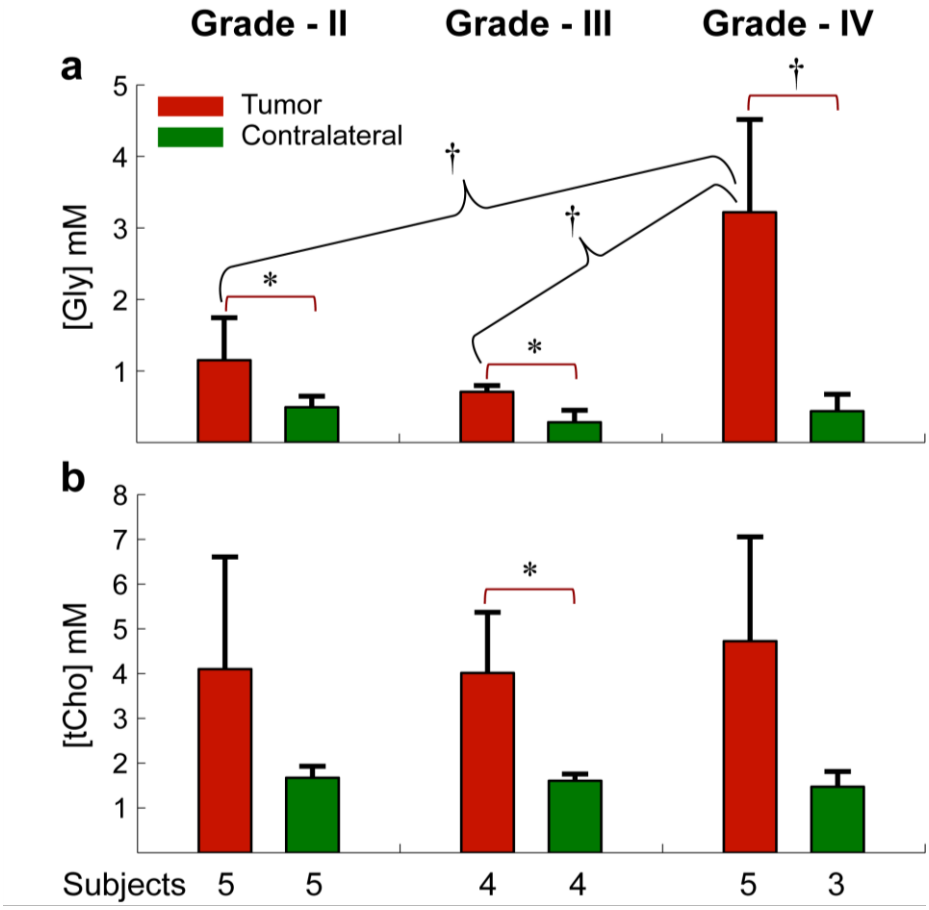

Figure 3-6 Mean Gly and tCho concentrations in the tumor and contralateral brain regions.

The mean Gly and tCho concentrations in the tumor and contralateral brain regions in 5 grade II, 4 grade III, and 5 grade IV gliomas are bar graphed with standard deviations. The contralateral estimates in grade IV were calculated from 3 patients, excluding 2 patients in whom the tumor was located in brainstem. Statistical significance is shown for $p < 0.05$, with an asterisk (*) for paired t-test and a dagger (†) for unpaired t-test.

For the 14 tumor patients, the Gly level was evaluated by averaging the estimate over ~4 voxels for each of the tumors and each of the contralateral normal appearing brain. Necrotic regions were not present in the tumors and no significant lipid or macromolecule signals were observed. The mean concentration of Gly in 14 patients was 1.8 ± 1.4 mM (CRLB of 11 ± 7 %) and 0.4 ± 0.2 mM (CRLB of 18 ± 10 %) for tumor and contralateral regions, respectively. Figure 3-6 presents the group comparison of the metabolite estimates. For grade II, III and IV gliomas, the mean Gly level in tumors was estimated to be 1.2 ± 0.6 (N = 5 subjects), 0.7 ± 0.1 (N = 4), and 3.3 ± 1.5 (N = 5) mM respectively, which were all significantly higher than the normal levels in the contralateral brain (0.5 ± 0.2, 0.3 ± 0.2, and 0.5 ± 0.3 mM respectively). Here the contralateral Gly level in glioblastoma patients was calculated from 3 patients, excluding 2 cases in which the tumor was located in brainstem. The mean Gly level was lower in grade III than in grade II tumors (0.7 *vs.* 1.2), but the ratio of the elevated Gly in tumors with respect to the contralateral brain was higher in grade III than in grade II (3.0 *vs.* 2.3). This was largely because the contralateral Gly estimate was very low in the grade III patients in whom the tumors were located mostly in WM dominant regions. Glioblastoma (grade IV) showed significantly higher Gly level compared to grade II and III tumors ($p < 0.05$ and 0.01 respectively). Excluding the 2 glioblastomas in brainstem, the mean tumor-to-contralateral Gly ratio in glioblastoma was calculated to be 10.5, significantly higher than those in grade II and III ($p < 0.01$and $p < 0.02$ respectively). Taken together, the Gly elevation was significantly higher in grade IV than in grade II and III, indicating that elevated Gly may be a marker of tumor malignancy. For tCho, the mean concentration in tumors was higher than the contralateral value for all three grades, but the

difference between the tumor and contralateral regions was significant only in grade III. The mean tCho level or the tumor-to-contralateral tCho ratio was not significantly different between the grades. The Gly-to-tCho ratio in tumors was significantly larger in grade IV compared to grade II and grade III ($p < 0.05$ and $p < 0.01$, respectively) and significant difference was not observed between grade II and grade III tumors.

3.4 DISCUSSION AND CONCLUSION

The study reports *in vivo* ^{1}H MR spectroscopy imaging of Gly in healthy brain and gliomas at 3T. The use of an optimal PRESS TE (160 ms) gave an effective suppression of the mIns signal in the proximity of the Gly resonance and consequently allowed Gly measurement with minimal contamination from the mIns background signals. The data indicated the presence of a regional variation of Gly in the healthy brain. The Gly concentration was estimated to be higher by > 2 fold in GM than in WM from a linear regression analysis, in good agreement with a recent single-voxel MRS study at 7T (44). The mean Gly CRLB was much smaller in GM voxels than in WM voxels (16% *vs*. 24%), which may be largely due to the regional difference of Gly. The Gly level was significantly increased in tumors. Compared to the contralateral normal appearing brain, Gly elevation in tumors was more extensive with increasing tumor grade, suggesting Gly as a potential biomarker of tumor malignancy. The observation of elevated Gly in all tumors in the current study is contrasted with the result from a prior study (5), which reported that Gly was elevated only in a subset of glioblastomas as measured using a single-voxel localized PRESS TE = 160 ms method. Given that in this prior study abnormal Gly levels in tumors were

evaluated with respect to the normal level (~0.6 mM) in the GM dominant region (medial occipital brain), it is most likely that elevated Gly in some tumors in WM dominant regions (*e.g.*, Fig. 4c in reference 10) was interpreted as normal. Of note, for the location of the tumor in the left-hemisphere WM dominant region, the normal Gly level was estimated to be approximately 0.3 mM in the present study.

The capability to discriminate Gly singlet from mIns signals could be affected by shimming. The *in vivo* linewidth was 4 - 7 Hz in healthy brain and 4 - 6 Hz in tumors in our data set. LCModel analysis of simulated spectra indicated that Gly estimate was not substantially influenced by increase in linewidth up to 7.5 Hz (see Figure 3-4). Also, Gly detection may depend on SNR. In the present study we observed a mean NAA SNR (calculated as ratio of peak amplitude of NAA and standard deviation of noise from signal-free region) of 74 ± 15 in the voxels with GM/(GM+WM) > 70% and 84 ± 12 in the voxels with WM/(GM+WM) > 80% in healthy brain data. The mean NAA SNR was 78 ± 12 for an estimated Gly concentration of 0.3 mM or more. LCModel analysis on *in vivo* healthy brain SVS data at TE = 160 ms indicated reliable Gly detection at NAA SNR of 70 or greater (Figure 3-7). The voxel size of the SI was set at 1.5 mL at acquisition and reconstructed at 0.375 mL, to achieve a sufficient SNR for Gly detection within an acceptable time frame. The spatial resolution of 1.5 mL is lower than those in some prior SI studies (~0.8 mL) (41,120-122). The spatial resolution of SI may be possibly enhanced without substantial loss of spectral information using echo-planar spectroscopic imaging (123), parallel imaging (120,121), and compressed sensing (124,125) techniques.

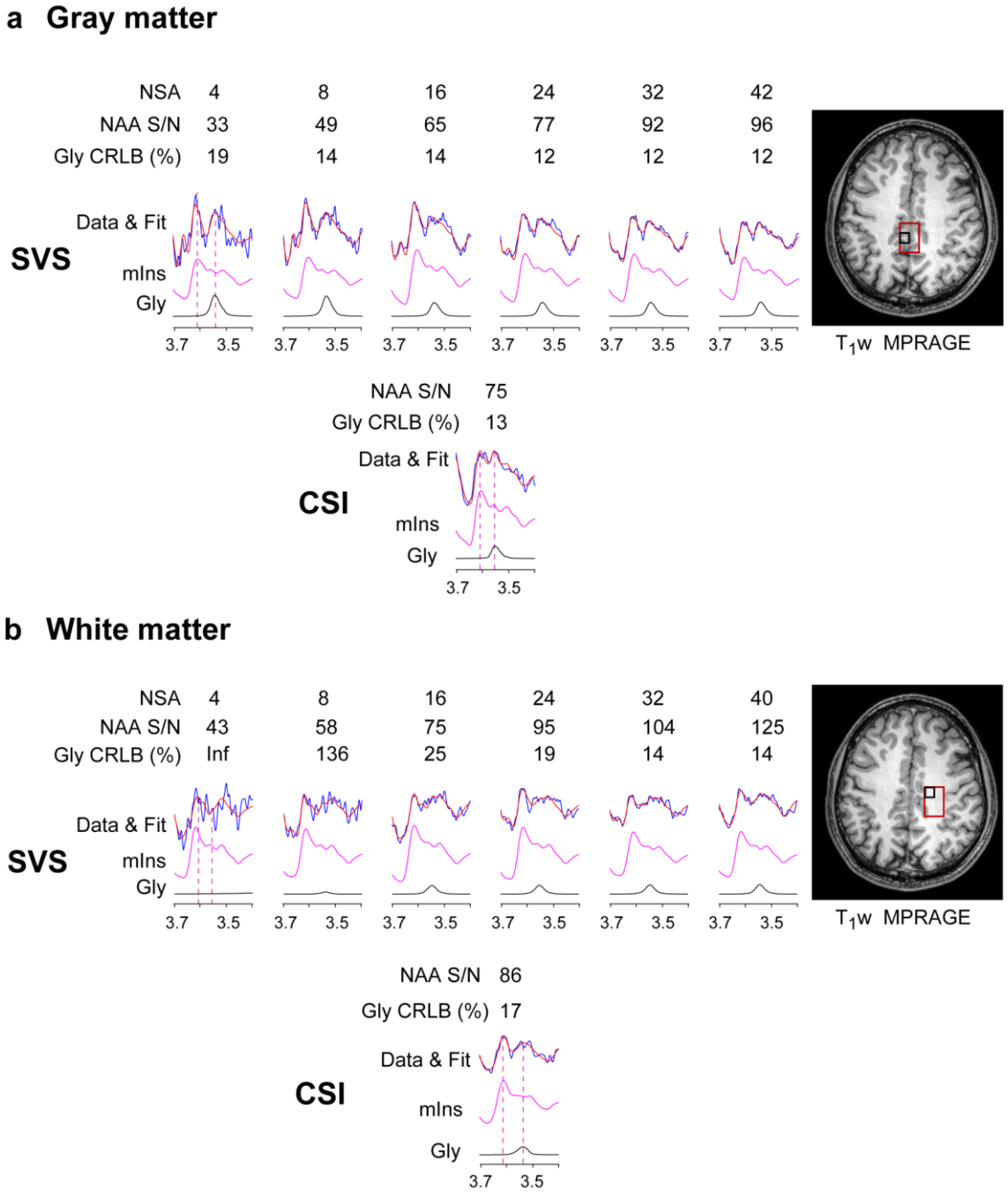

Figure 3-7 SNR dependence of Gly detectability.
In vivo SVS and MRSI spectra of Gly and mIns in (a) GM-dominant and (b) WM-dominant regions. SVS spectra are shown for various NSA (number of signal average). The SVS voxel (red line; 9 mL) and MRSI voxel (green line; 0.375 mL) are shown in T_1w-MPRAGE images. For both GM- and WM-regions, the Gly signals were successfully resolved with acceptable CRLBs when NAA SNR of ~70 or higher.

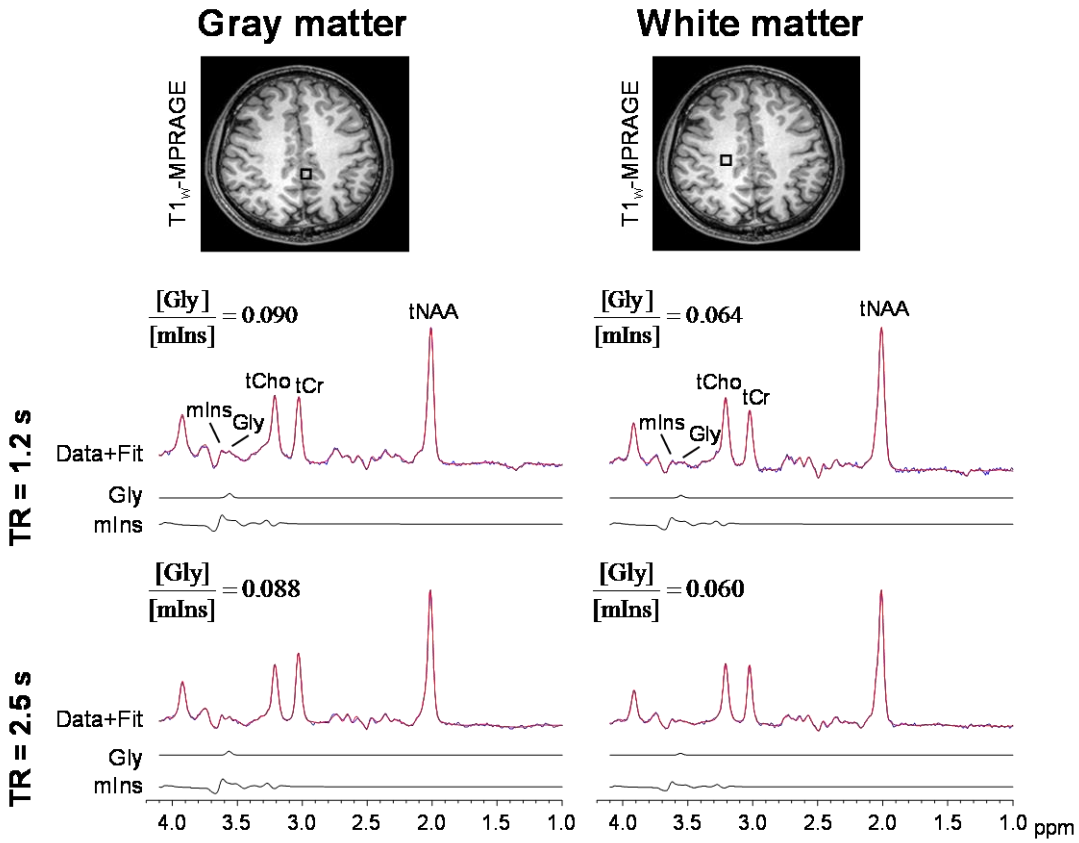

Figure 3-8 Comparison of spectroscopic imaging data obtained with TR = 1.2 and 2.5 s. Each of the spectra is normalized to the tNAA (2.01 ppm) peak amplitude. The CRLBs of Gly and mIns in gray matter region spectra were 10% and 4% for TR = 1.2 s and 9% and 3% for TR = 2.5 s, respectively. The CRLBs of Gly and mIns in white matter region spectra were 16% and 5% for TR = 1.2 s and 16% and 6% for TR = 2.5 s, respectively. The Gly and mIns composite signal pattern was similar between the TRs. Significant differences were not observed in the CRLBs of Gly and mIns between the TRs. The Gly-to-mIns estimate ratio was also similar between the TRs (0.090 vs. 0.088 in GM and 0.064 vs. 0.060 in WM, respectively)

The T_2 of Gly was assumed to be identical to T_2 of mIns (200 ms), and this assumption may introduce small error in estimation of Gly, depending on the difference in Gly and mIns T_2s. In phantom studies Gly T_2 was measured to be long compared to T_2 of

mIns (1.5 s *vs.* 0.75 s). However, the phantom T_2 data may not be directly applicable to the *in vivo* situation since T_2 may differ between aqueous solutions and brain tissue. For instance, the *in vivo* T_2 values of the CH_3 group protons of Cr and NAA are quite different in human brain (*i.e.*, 150 vs. 300 ms) while their T_2 values in phantom solutions are very similar. Also, the mIns T_2 may be longer than the Cr CH_3 T_2 in brain (81,113), but it is the opposite in an aqueous solution. Given the small molecular size of Gly, the Gly molecules may be very mobile *in vitro* and consequently the Gly CH_2 proton T_2 is measured to be long (*i.e.*, much longer than the Cr CH_2 T_2 and similar to the Cr and NAA CH_3 T_2s). For proton NMR, although the intra-molecular dipole-dipole interaction is a dominant mechanism for T_2 relaxation in most cases, there may be several other factors that affect the TE dependence of PRESS signals (namely, apparent T_2), which may include molecular diffusion, magnetization transfer (96), and the environments in which the molecules reside. In addition, the T_1 saturation effects of metabolites in healthy brain and tumors were assumed to be equal, based on our *in vivo* experiment (Figure 3-8), in which the Gly and mIns composite signal pattern and estimate ratios from GM and WM dominant regions were very similar between TR = 1.2 and 2.5 s.

Spectroscopy imaging of Gly may provide a clinically useful tool compared to single-voxel MRS. The brain Gly level appears to be quite different between GM and WM, as shown in a prior study (44) and in the current study. The Gly elevation may be regionally different between many brain lesions, as shown in Figure 3-5. Our data indicated ~2 fold difference in Gly levels between the lesions and more than 4 fold elevations when compared to contralateral normal brain regions. To date, noninvasive *in vivo* detection of elevated Gly

in malignant tumors has been achieved largely using single-voxel MRS (5,100). Gly spectroscopic imaging may provide a unique opportunity to study multiple lesions and to investigate the disease infiltration into surrounding normal tissue. In a prior Gly imaging study at 3T by Hattingen et al., data were acquired at both short (~30 ms) and long echo times (~140 ms) and the spectral difference between the two TEs was analyzed to obtain the Gly portion of the composite signal (41). As demonstrated in the current study and in a prior study (45), imaging of Gly and mIns can be achieved using a single refined optimized TE, which simplifies the spectral analysis without need of additional data analysis. A major drawback of our SI method is extensive T_2 signal loss due to the use of long TE (160 ms), but selected signals are often better resolved at optimized long TE, benefiting from attenuated macromolecule signals (44,65). With its improved ability for Gly detection, the proposed Gly SI method may have extended applications for which alterations of Gly levels are relatively small.

The ability to image Gly in the human brain may have important applications in the diagnosis and management of malignant gliomas. Tumors reprogram their metabolism to meet the needs of rapid cell growth and survival in harsh environments (126). Thus, changes in metabolite abundance relative to normal tissue may serve as a biomarker of malignancy. Evidence suggests that production of Gly is under oncogenic control, emphasizing its importance in tumor biology (127). A recent mass spectrometry study in a wide range of cancer cell lines (NCI-60) (103) indicates that Gly may play a critical role in rapid cell proliferation. Elevation of Gly in tumors relative to contralateral is distinctly pronounced in GBM compared to lower grade tumors (~10 fold vs. ~3 fold). Thus longitudinal monitoring

of Gly in serial measurements in patients may provide a noninvasive tool for early detection of malignant transformation. A recent study indicated correlation of Gly elevation with increase in tCho, cerebral blood flow, and enhancement of contrast in MR imaging (45). Hence the capability to monitor the changes in Gly levels noninvasively by means of spectroscopic imaging would help to identify diffuse infiltration into normal brain and/or metabolically active regions in the periphery of the tumor mass.

CHAPTER FOUR
2-hydroxyglutarate (2HG) detection in gliomas by ^{1}H-MRS imaging

4.1 INTRODUCTION

4.1.1 Literature review

Gliomas are the most common primary brain tumors (128). Gliomas can be classified into three WHO grades i.e. grade II – low grade, grade III – anaplastic, and grade IV – glioblastoma, gliosarcoma, glioblastoma with oligodendroglial (129). Each of these gliomas shows several specific mutations in their genetic maps. Several studies have associated IDH mutations with longer life expectancy compared to IDH wild type gliomas (62,64). These mutations occur > 70% in low grade gliomas and secondary glioblastomas (62-64). In oligodendrogliomas IDH mutations precede the 1p/19q codeletion, while in astrocytomas they precede tumor protein p53 mutations (130). While the wild type IDH converts isocitrate to α-ketoglutarate, the mutated IDH converts α-ketoglutarate to 2-hydroxyglutarate (2HG) (61) (Figure 4-1). Both wild type IDH and mutated IDH enzymes were observed in IDH mutated tumors (131). Some studies have suggested that the mutations may represent an early step in gliomagenesis i.e. tumor progression (130).

In the healthy brain 2HG levels are extremely low, virtually undetectable using noninvasive techniques. In contrast, 2HG levels are elevated orders of magnitude in gliomas with IDH mutations (61). Recently, several *in vivo* studies have reported detection of 2HG in IDH-mutated gliomas using ^{1}H-MRS (6,27,30,132). Noninvasive detection of 2HG may

become an important biomarker for predicting tumor genetics, and monitoring therapeutic response.

4.1.2 Aim of the project

To develop new ^{1}H-MRS techniques for reliable detection of 2HG in human gliomas at 3T and 7T. To measure the reproducibility of the 2HG measures. To evaluate the utility of 2HG as a prognostic and diagnostic biomarker in gliomas. To assess the feasibility and utility of 3D 2HG imaging.

4.2 MATERIALS AND METHODS

4.2.1 Experimental setup

MR experiments were carried out in a 3T and 7T whole-body scanner (Philips Medical Systems). The 3T scanner was equipped with an integrated body coil for RF transmission and an 8-channel phased-array coil for signal reception. The 7T scanner was equipped with quadrature birdcage RF transmission and 16-channel signal reception.

4.2.2 Numerical simulations

Numerical density-matrix quantum mechanical simulations were carried out to optimize the subecho times of a PRESS sequence to improve the spectral resolution between the 2HG (2.25 ppm) and Glu (2.35 ppm), and Gln (2.45 ppm) resonances. 3D-volume localized spectra were calculated for various subecho times incorporating the experimental RF and gradient pulse waveforms, according to a product-operator based transformation-

matrix method described in a prior study (6,30,133). The simulations were programmed with Matlab® (The MathWorks, Inc.).

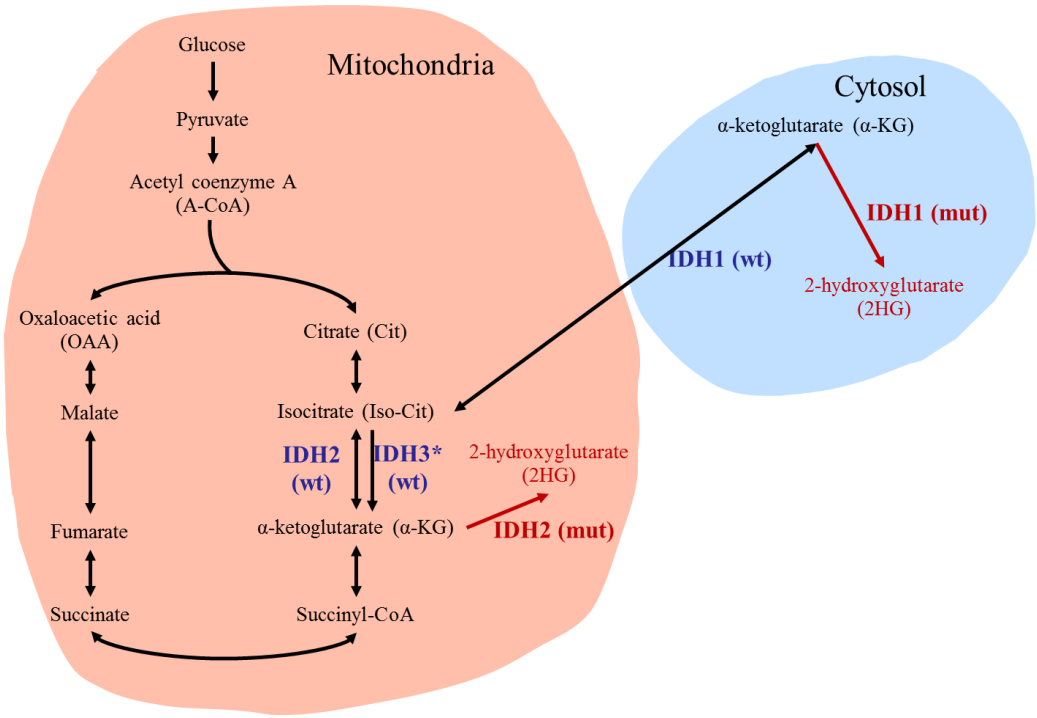

Figure 4-1 Metabolic pathways of wild type and mutated IDH.
Oncogenic mutations in IDH1 and IDH2 produce 2HG.

4.2.3 MR Spectroscopy acquisition details at 3T

Slice-selective RF pulses included 90° RF pulse (9.8 ms, bandwidth = 4.2 kHz) and 180° RF pulse (13.2 ms, bandwidth = 1.3 kHz) at an RF field intensity of 13.5 μT. ^{1}H MR spectroscopic imaging (SI) data were obtained using phase encoding gradients within a PRESS sequence for spatial localization. The volume of interest (VOI) was prescribed by the PRESS sequence with TE = 97 ms (TE_1 = 32 ms and TE_2 = 65 ms). The MR protocol included survey imaging followed by T_2-weighted fluid attenuated inversion recovery (T_2w-

FLAIR) imaging (TR/TE/TI = 11000/125/2800 ms, FOV = 230 × 230 mm^2, slice thickness of 5 mm, 28 slices along each of transverse and sagittal directions) for tumor identification.

For SI data acquisitions, a PRESS-prescribed transverse slice was positioned to cover the region of interest with spatial resolution of 10 × 10 mm^2 and slice thickness of 15 mm. In each SI scan, a 20 × 16 data matrix was obtained from a 200 × 160 mm^2 FOV. A vendor-supplied 2D elliptical k-space sampling scheme was used (109), to reduce the acquisition time by ~30%. Each k-space point with 1024 complex points was acquired with two averages at TR = 1.2 s and spectral width = 2000 Hz. The SI data were reconstructed with 2D Fourier transformation of the k-space data, after zero filling the non-acquired k-space points and zero-padding the data matrix to two fold along each phase encoding direction (*i.e.*, 40 × 32) to obtain spatial resolution of 5 × 5 mm^2. The PRESS RF pulses were tuned to 2.6 ppm which is halfway between the N-acetylaspartylglutamate 4.6 ppm and lactate 1.3 ppm resonances. Water suppression was performed using a four RF-pulse scheme (110). Four outer volume suppression bands were placed in the periphery of the VOI to minimize potential contamination from extracranial lipids and water outside the VOI. First- and second-order shimming was carried out on VOI using FASTMAP (85). To minimize motion artifacts, foam pads were placed to restrict head motions inside the reception coil. The scan time of a single SI acquisition was approximately 10 minutes.

4.2.4 MR Spectroscopy acquisition details at 7T

Slice-selective RF pulses included an 8.8 ms 90° RF pulse (bandwidth = 4.7 kHz) and an 11.9 ms 180° RF pulse (bandwidth = 1.4 kHz) at B_1 = 15 μT. ^{1}H MR spectroscopic

imaging (SI) data were obtained using phase encoding gradients within a PRESS sequence for spatial localization. The volume of interest (VOI) was prescribed by the PRESS sequence with TE = 78 ms (TE_1 = 58 ms and TE_2 = 20 ms). The MR protocol included survey imaging followed by T_2-weighted fluid attenuated inversion recovery (T_2w-FLAIR) imaging (TR/TE/TI = 11000/93/2800 ms, FOV = 230 × 200 mm^2, slice thickness of 5 mm, 16 slices along each of transverse) for tumor identification.

For SI data acquisitions, a PRESS-prescribed transverse slice was positioned to cover the region of interest with spatial resolution of 10 × 10 mm^2 and slice thickness of 15 mm. In each SI scan, a 20 × 16 data matrix was obtained from a 200 × 160 mm^2 FOV. A vendor-supplied 2D elliptical k-space sampling scheme was used (109), to reduce the acquisition time by ~30%. Each k-space point with 2048 complex points was acquired with two averages at TR = 1.8 s and spectral width = 5000 Hz. The SI data were reconstructed with 2D Fourier transformation of the k-space data, after zero filling the non-acquired k-space points and zero-padding the data matrix to two fold along each phase encoding direction (*i.e.*, 40 × 32) to obtain spatial resolution of 5 × 5 mm^2. The PRESS RF pulses were tuned to 2.6 ppm which is halfway between the N-acetylaspartylglutamate 4.6 ppm and lactate 1.3 ppm resonances. Water suppression was performed using a four RF-pulse scheme (110). Four outer volume suppression bands were placed in the periphery of the VOI to minimize potential contamination from extracranial lipids and water outside the VOI. First- and second-order shimming was carried out on VOI using FASTMAP (85). To minimize motion artifacts, foam pads were placed to restrict head motions inside the reception coil. An unsuppressed water SI data was also acquired using an RF carrier at the water resonance for

residual eddy current compensation. The scan time of water suppressed SI acquisition was approximately 15 minutes.

4.2.5 Human subjects with gliomas

Subject were screened and recruited by neuro-oncologist and neuro-surgeons at UT Southwestern Medical Center, Dallas. Subjects with well-defined tumors (hyper-intensities on T_2w-FLAIR images) were selected for acquiring MRSI data. Only subjects without metal implants in the body were selected for 7T study.

4.2.6 Reproducibility study

Five subjects with glioma were recruited to study the reproducibility of 2HG measures (two low grade oligodendroglioma, one anaplastic astrocytoma and two without any biopsy or surgery). Each subject had two MR examinations on the same day (Scan-1 and Scan-2) to evaluate the reproducibility. All the subjects had detectable 2HG signal. To evaluate the reproducibility, voxels from the tumor mass and contralateral were selected and Coefficient of Variance (CV) and Intraclass Correlation Coefficient (ICC) were calculated with multi-factorial random effects model from analysis of variance (ANOVA) (134,135).

4.2.7 Phantom studies at 3T

The performance of PRESS TE = 97 ms was validated on a phantom containing 2HG (8mM) and glycine (Gly) (10mM). Data were acquired with TR of 3.0 sec, spectral width of 2000 Hz and 1024 complex points per FID. Phantom SI data were obtained with a 32 × 32 data matrix with a field of view (FOV) of 160 × 160 mm^2, VOI of 50 × 50 mm^2 and four signal averages.

4.2.8 Phantom studies at 7T

The validati of PRESS TE = 78 ms was performed on a phantoms containing 2HG (8 mM) and Gly (10 mM). Data were acquired with TR of 3.0 sec, spectral width of 5000 Hz and 2048 complex points per FID. Data were obtained with a 32 × 32 data matrix with a field of view (FOV) of 160 × 160 mm^2, VOI of 50 × 50 mm^2 and four signal averages.

4.2.9 Post-processing, analysis and quantification of SI data

During post-processing, residual water signals were further minimized using a singular value decomposition algorithm in jMRUI (5,6,41,111). A 1-Hz exponential function was multiplied to FIDs prior to Fourier transformation, in order to suppress potential distortions in the later part of the FIDs. Correction for spatial B_0 was performed using in-house programs written in MATLAB® (MathWorks Inc., Natick, MA, USA). The FIDs were zero filled to 4096 points and spectra were analyzed with LCModel (Version 6.3) (86,112) using numerically simulated basis sets, which were calculated according to a published method (6). The basis function included simulated spectra of sixteen brain metabolites; 2HG, tCr, tNAA, tCho, Glu, Gln, GABA, Gly, mIns, glutathione, lactate, alanine, taurine, scyllo-inositol, aspartate, phosphoethanolamine, and serine. Spectral fitting was undertaken between 0.5 - 4.1 ppm. For validation purpose, additional LCModel fitting was performed without 2HG in the basis sets. For estimation of Glu, NAA, tCr, and tCho concentrations, the transverse relaxation effects were corrected using published T_2 values of 180, 250, 150, and 230 ms, respectively (5,113) for data at 3T. The T_2s of 2HG, Gln and GABA were assumed

to be equal to the Glu T_2. Metabolite estimates in molar concentrations (mM) were then obtained with reference to tCr in white matter regions at 6.4 mM (114-118), ignoring potential difference in T_1 saturation effects between metabolites in healthy brain and tumors. The linewidth (FWHM) estimates were obtained from the LCModel output. Maps of metabolite estimates and Cramér-Rao lower bounds (CRLB) for the VOI were generated. The maps (e.g. matrix of size 16 × 16) were then interpolated 10 fold (e.g. 160 × 160) using the nearest neighbor method. The correction for the chemical shift displacement effects was performed by shifting the metabolite matrix grid according to the ratio of the chemical shift difference of metabolite resonances from the PRESS RF carrier frequency (2.6 ppm) with respect to the PRESS RF pulse bandwidths. For this, a major resonance was chosen for each metabolite based on the highest signal selectivity. The major resonance used was 2.25, 2.35, 2.45, 3.21, 3.03, and 2.02 ppm for 2HG, Glu, Gln, tCho, tCr, and tNAA respectively. For 2HG, the chemical shift displacement of the VOI was 1% and 3.5% along the anterior-posterior (selected by the 90° pulse) and left-right directions (selected by the 180° pulse), respectively. After the shift, the matrix grid was reduced to the original matrix size by averaging over 10 × 10 pixels.

4.3 RESULTS

4.3.1 Numerical simulations results at 3T

A 2HG molecule has five nonexchangeable scalar-coupled protons, resonating at 4.02 ppm, 2.27, 2.22, 1.98, and 1.83 ppm, giving rise to multiplets at approximately three locations at 3 T; that is, 4.02 ppm (H2), ~2.25 ppm (H4 and H4′) and ~1.9 ppm (H3 and H3′)

(6). The 2HG resonances are all scalar coupled, and, consequently, the spectral pattern and signal strength vary with changing echo time of MRS sequence (6). Figure 4-2 shows the numerically calculated spectra of the 2HG H4 resonances for various PRESS TE_1 and TE_2 values at 3T. At an echo time of 97 ms (TE_1 = 32ms and TE_2 = 65 ms), the 2HG signal is temporally maximum and well separated from Glu, and Gln signals. The maximum signals of 2HG, Glu, and Gln (H4 resonances) appear at 2.25 ppm, 2.35 ppm and 2.45 ppm, respectively.

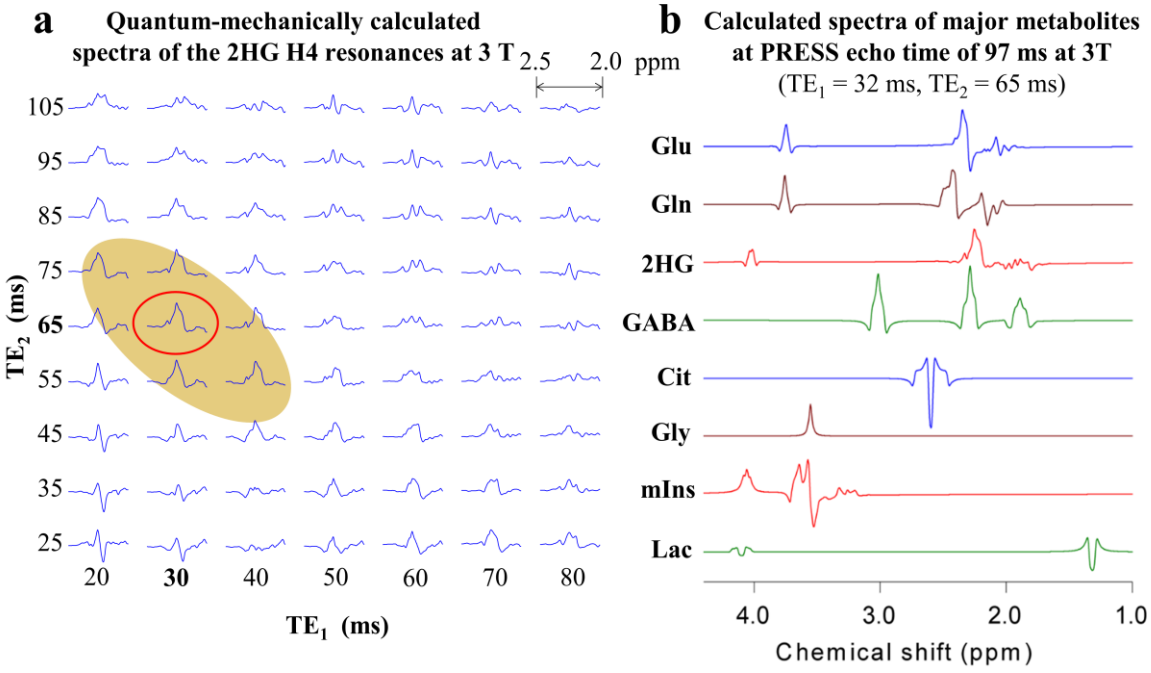

Figure 4-2 Numerically simulated metabolite spectra at 3T.
(a) The 2HG H4 signal at 3T is shown versus the first and second echo times, TE_1 and TE_2, of PRESS. (b) The signals of Glu, Gln, 2HG, GABA, Cit, Gly, mIns, and Lac are shown for PRESS TE = 97 ms (TE1 = 32 ms, TE2 = 65 ms).

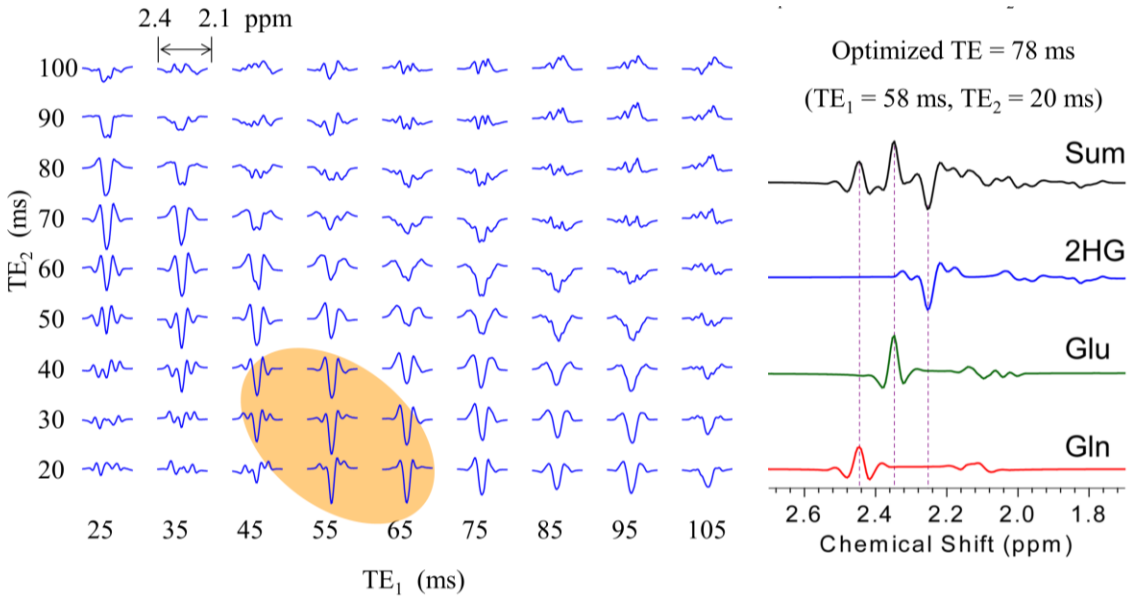

Figure 4-3 Numerically simulated metabolite spectra at 7T.
(a) The 2HG H4 signal at 7T is shown versus the first and second echo times, TE_1 and TE_2, of PRESS. (b) The signals of Glu, Gln, and 2HG are shown for PRESS TE = 78 ms (TE_1 = 58 ms, TE_2 = 65 ms).

4.3.2 Numerical simulations results at 7T

Figure 4-3 shows the numerically calculated spectra of the 2HG H4 resonances for various PRESS TE_1 and TE_2 values at 7T. At an echo time of 78 ms (TE_1 = 58 ms and TE_2 = 20 ms), the 2HG signal is temporally maximum and well separated from Glu, and Gln signals. 2HG signal at 2.25 ppm appears as an inverted peak. The maximum signals of Glu, and Gln (H4 resonances) appear at 2.35 ppm and 2.45 ppm, respectively.

4.3.3 Phantom studies at 3T

The performance of PRESS TE = 97 ms was validated on a phantom containing 2HG (8mM) and glycine (Gly) (10mM) (Figure 4-4). Spectra and LCModel fits were consistent with the simulated 2HG spectral pattern.

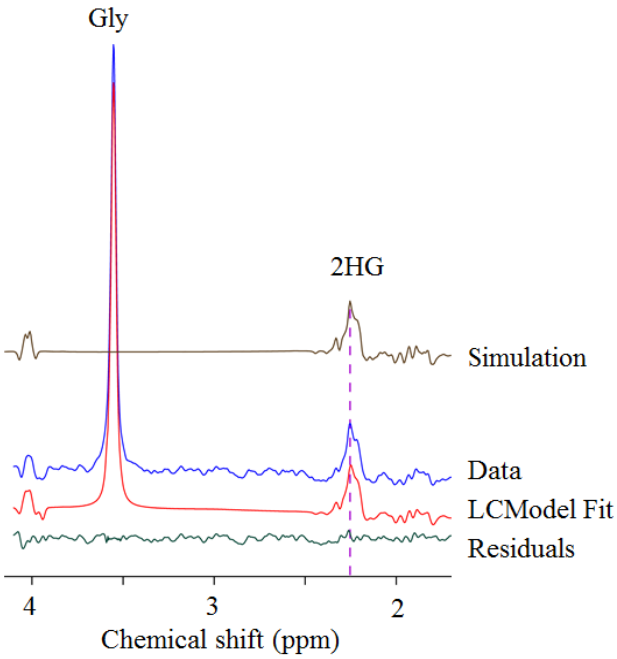

Figure 4-4 Phantom SI data from PRESS TE = 97 ms.
SI data from a phantom containing 2HG (8 mM) and Gly (10 mM). Spectra (blue), LCModel fit (red) are consistent with the simulated data (brown).

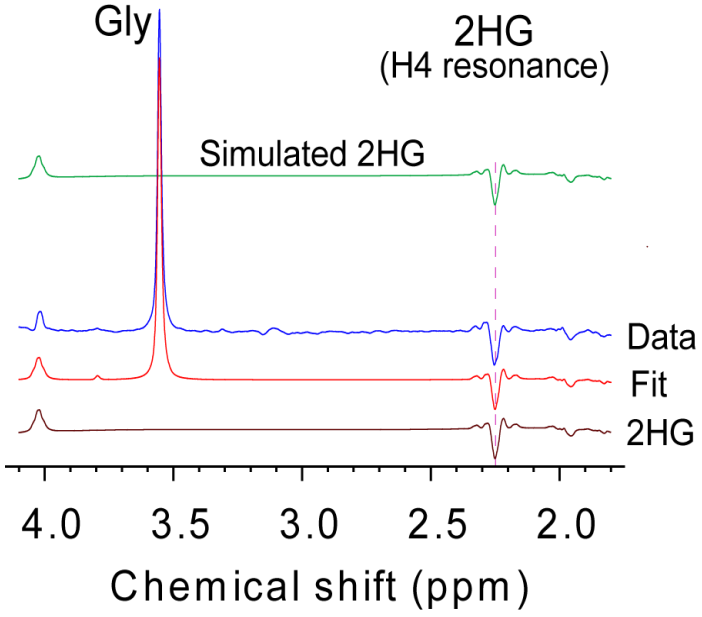

Figure 4-5 Phantom SI data from PRESS TE = 78 ms.
SI data from a phantom containing 2HG (8 mM) and Gly (10 mM). Spectra (blue), LCModel fit (red) are consistent with the simulated data (green).

4.3.4 Phantom studies at 7T

Spectra from phantom containing 2HG and Gly show an inverted peak of 2HG at 2.25 ppm, in excellent agreement with the simulation results (Figure 4-5). Spectra and LCModel fits were consistent with the simulated 2HG spectral pattern.

4.3.5 *In vivo* detection of 2HG at 3T

Figure 4-6 shows the SI grid overlaid on top of FLAIR images and spectra from subject with oligodendroglioma. Spectra from the voxel within tumor region showed elevated tCho, reduced tCr and tNAA. A large signal at ~2.25 ppm was observed, attributable most to the 2HG peak at 2.25 ppm. LCModel analysis of the spectra gave a 2HG, Glu and Gln estimates of 7, 2 and 2 mM, respectively. The CRLB of the metabolites were 4 %, 9 % and 26 %, respectively.

4.3.6 Reproducibility of 2HG detection in IDH-mutated gliomas at 3T

Figure 4-7 shows the Scan-1 and Scan-2 data from five subjects with gliomas. The spectra shown were selected from voxels within the tumor regions identified by T_2w-FLAIR. The spectra in Scan-1 and Scan-2 showed similar spectral pattern, over 1.8 – 4.1 ppm region. Figure 4-8 shows the Scan-1 and Scan-2 spectra from voxels located in tumor and normal-appearing brain regions of a low grade oligodendroglioma subject. Spectra were selected from voxels located in normal appearing and tumor brain regions on the T_2W-FLAIR images. Spectra from Scan-1 were identical to the spectra from Scan-2, indicating excellent reproduction of 2HG MRS. This was observed in both spectra from tumor and normal appearing brain regions. The metabolite estimates were similar between the two scans.

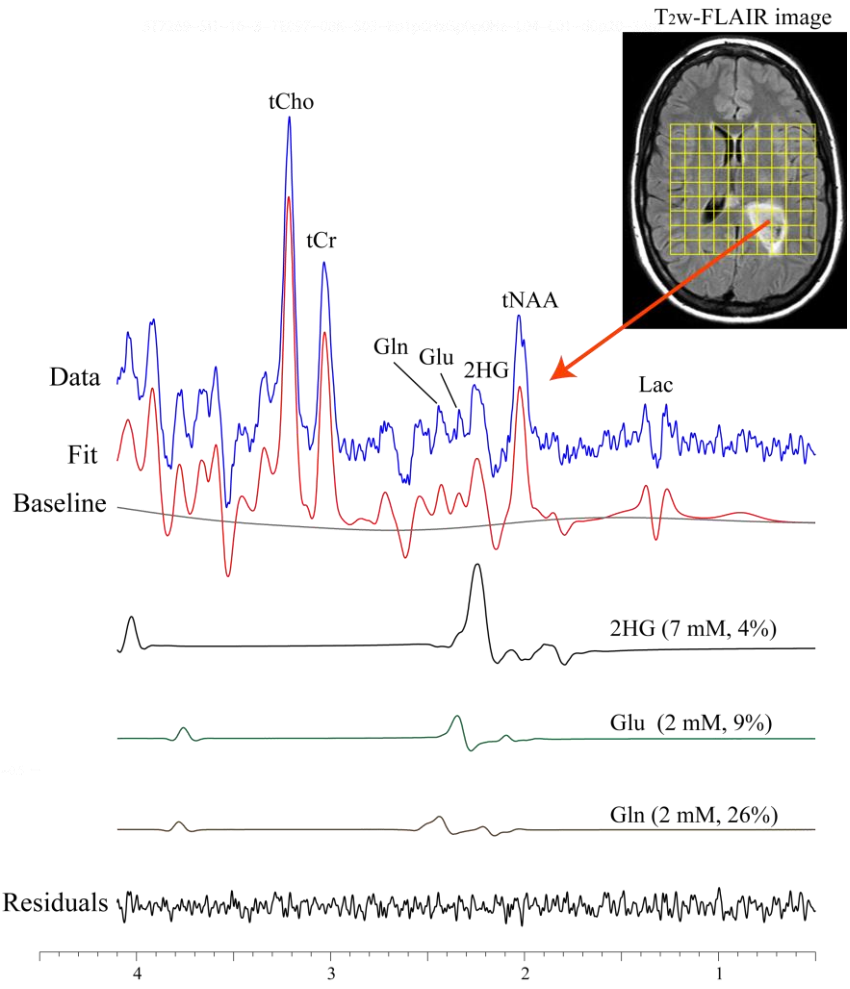

Figure 4-6 Spectra and metabolite estimates from a oligodendroglioma subject at 3T
Spectra (blue), LCModel fit (red) from a voxel selected from tumor regions (shown in the axial T_2w-FLAIR image). CRLB values of the fitting are mentioned in parentheses.

	No surgery	No surgery	Low grade oligodendroglioma	Low grade oligodendroglioma	Anaplastic Oligoastrocytoma		ICC	CV
2HG	2.6	3.1	3.2	3.3	7.7		0.77	0.29
Glu	2.3	4.6	2.2	4.9	2.4		0.84	0.19
Gln	2.3	2.4	4.1	3.1	2.1		0.81	0.24
tCho	2.3	2.1	2.2	2.6	3.2		0.93	0.06
tNAA	2.3	5.2	3.1	7.2	2.9		0.98	0.01

Table 4-1 Mean estimates of 2HG, Glu, Gln, tCho and tNAA along with ICC and CV estimates.
The metabolite estimates are shown in mM. Coefficient of Variance (CV) and Intraclass Correlation Coefficient (ICC) across the scans are shown.

Figure 4-9 shows the comparison of the metabolite estimates from the Scan-1 to those from the Scan-2 for all five glioma subjects for 2HG, tCho, tNAA, Glu, and Gln in tumor region. The mean 2HG levels over the tumor mass in five subjects were 2.6, 3.1, 3.2, 3.3 and 7.7 mM. The mean metabolites estimates, ICCs and CVs are shown in Table 4-1. ICC was for 2HG was 0.77, very similar to the values of Glu prior studies (136), indicating excellent reproducibility. ICC of Glu, Gln, tCho and tNAA was higher (0.81 – 0.98) in the present tumor study when compared to previous healthy volunteer study (136). CVs for tCho and tNAA were similar to previously reported studies at 3T (136). CVs for Glu, Gln are ~4 fold higher than previously reported studies at 3T, but the previous studies were performed on healthy volunteers (136).

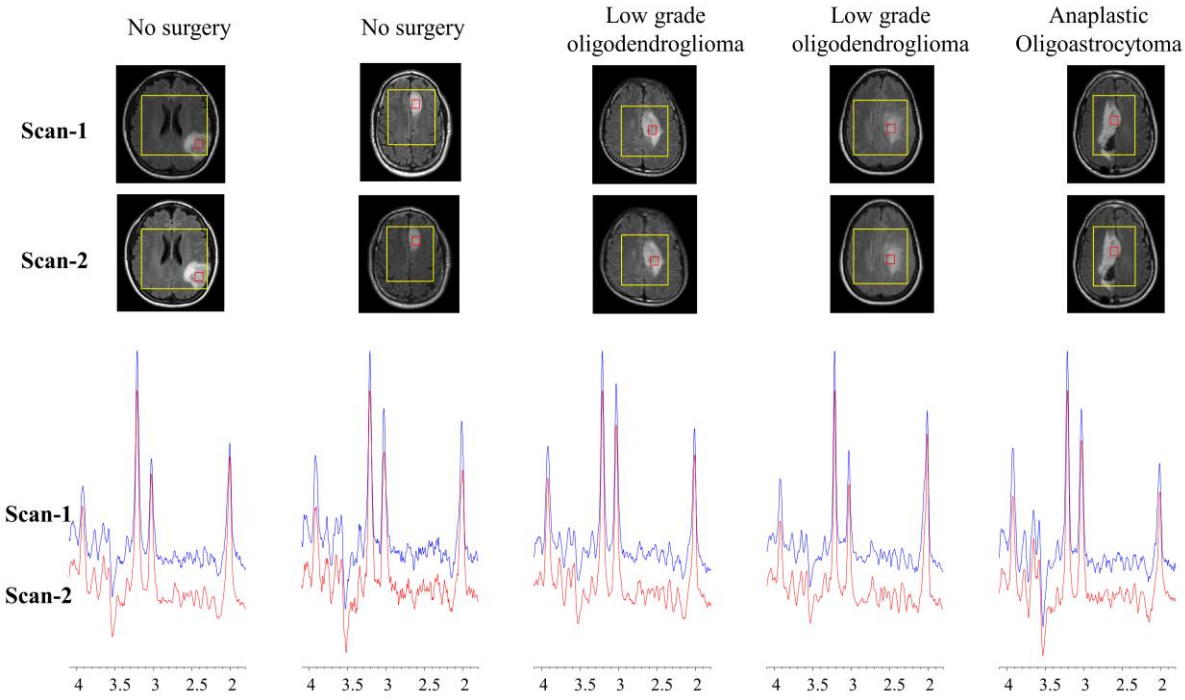

Figure 4-7 *In vivo* spectroscopic Scan-1 and Scan-2 data from five gliomas subjects.

Spectra were selected from the tumor regions shown on the T_2w-FLAIR image. Spectra in blue and red were obtained in Scan-1 and Scan-2, respectively.

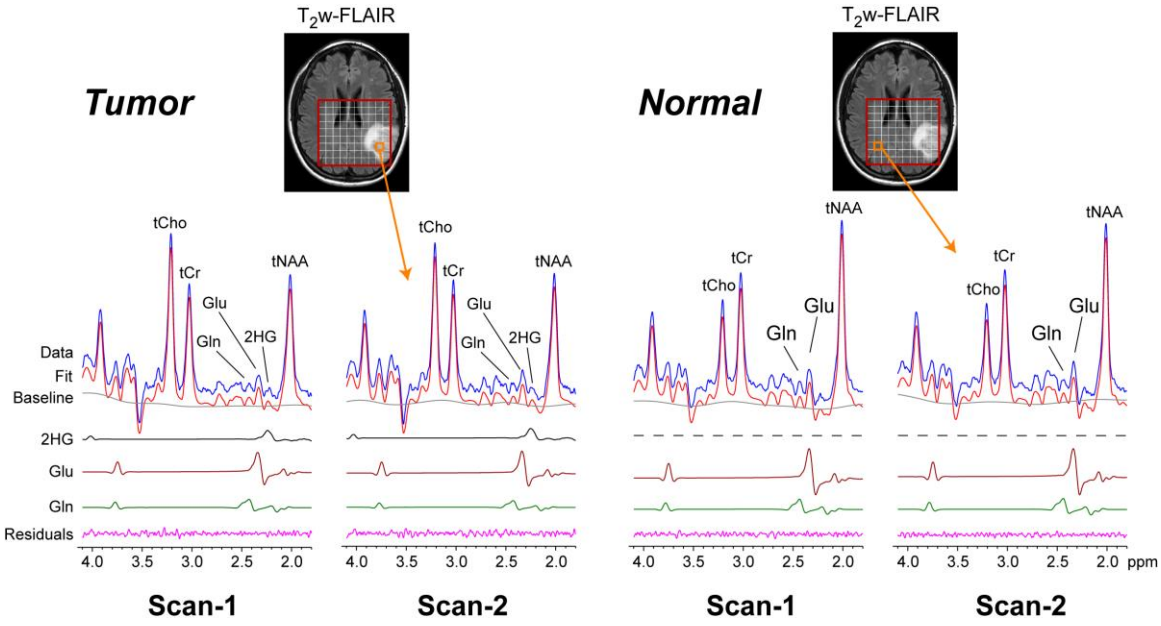

Figure 4-8 *In vivo* Scan-1 and Scan-2 data from a low grade oligodendroglioma subject. Spectra, LCModel fittings, residuals along with 2HG, Glu and Gln signals from two voxels selected from normal and tumor regions in a low grade oligodendroglioma.

4.3.7 Diagnostic utility of 2HG measures in gliomas

2HG MRS may provide a noninvasive diagnostic tool for IDH mutated gliomas. This utility is especially useful for the lesions where surgical biopsy is challenging due to the risks of permanent neurologinal injury. T_2w-FLAIR identified a lesion in the brainstem (Figure 4-10). An initial experiment presented large 2HG signal at 2.25 ppm, which indicated that the tumor may be an IDH-mutated glioma. In the light of these findings, the decision was made to follow the subject without surgery or treatment and to monitor the 2HG level in serial scans. We have been following the subject for the last 30 months and the 2HG level was

stable during that time period. Figure 4-10 shows the location of the tumor mass, and the concentration maps of 2HG, and tCho/tNAA ratio.

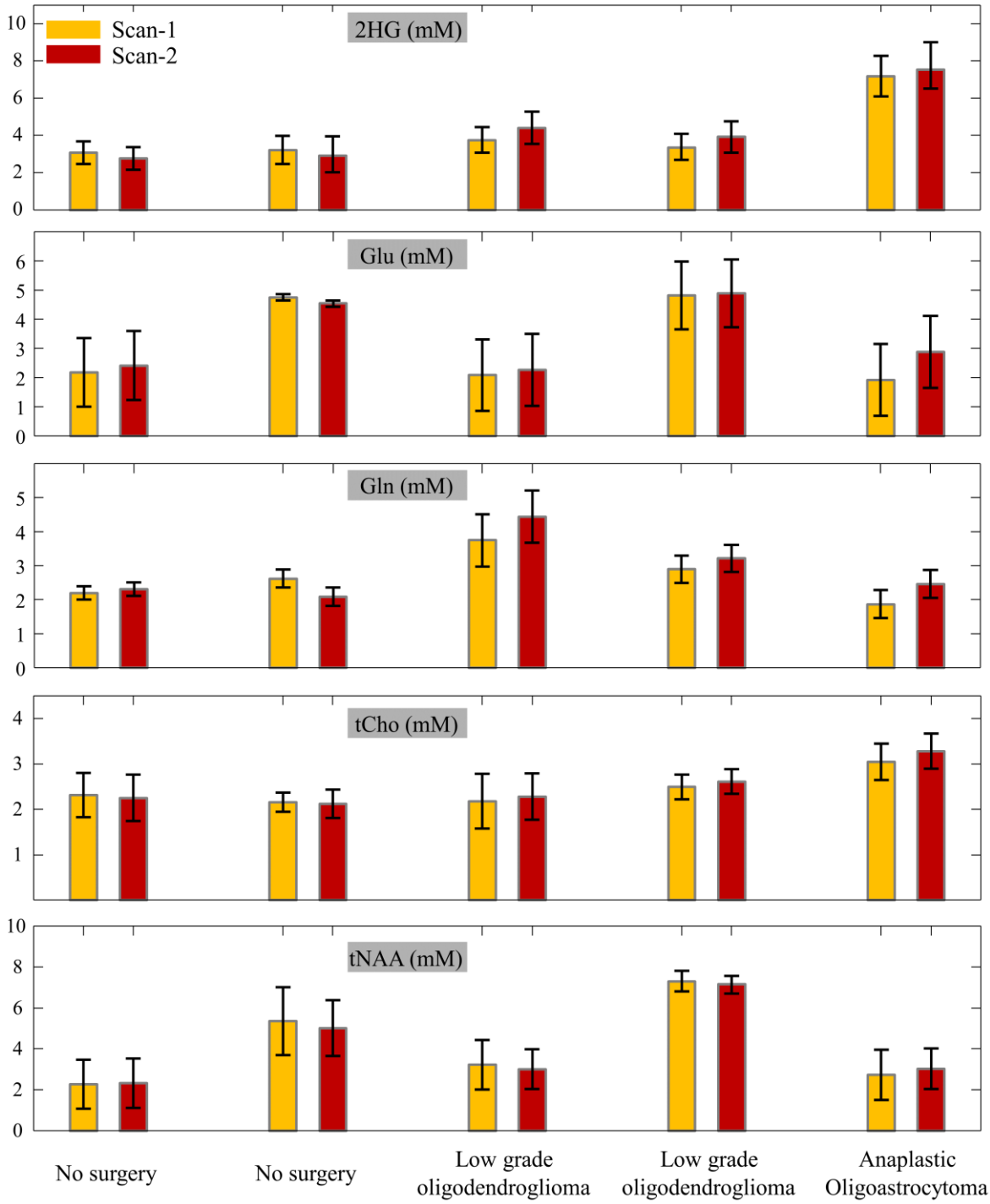

Figure 4-9 Reproducibility plots of 2HG, Glu, Gln, tCho and tNAA in five subjects.
The metabolite estimates were obtained from voxels located in the tumor regions. The metabolite estimates are shown in mM

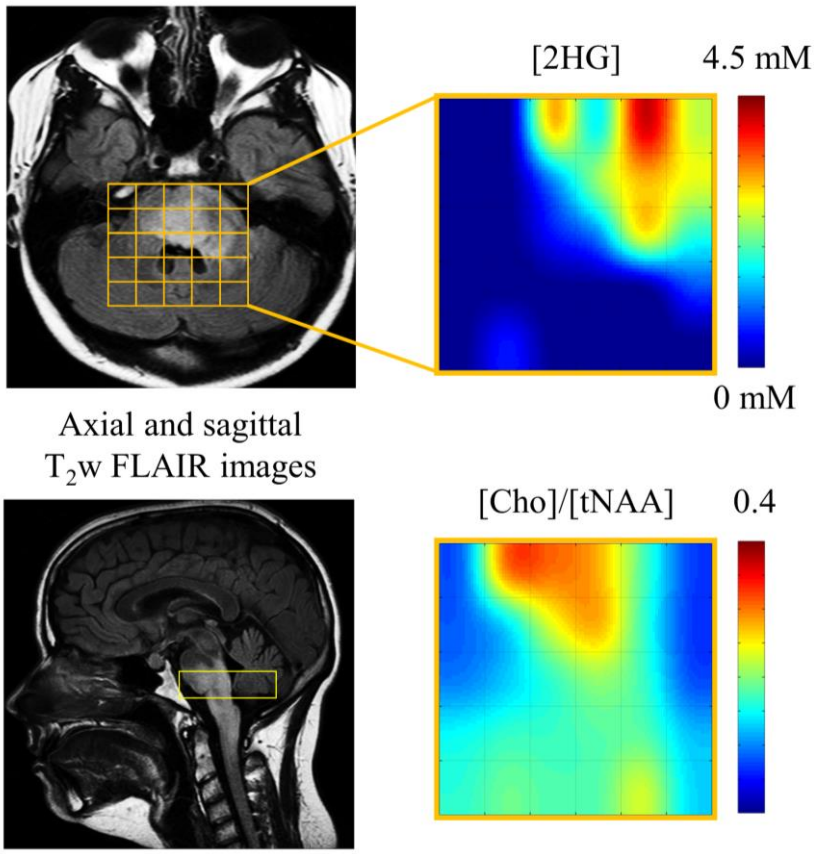

Figure 4-10 Subject with hyper-intensity in brain stem on a T_2w-FLAIR image.
The SI grid was placed in the brain stem covering the pons, and cerebellum regions. The mean 2HG was estimated to be ~3 mM.

4.3.8 Prognostic and therapeutic monitoring with 2HG

Figure 4-11 shows a case of an oligodendroglioma patient followed over the course of ~20 months. The patient came in with clinical symptoms such as seizures, left-leg weakness after 5 months being enrolled in the study. The clinical imaging showed no significant enlargement of area with T_2w-FLAIR hyper-intensity. MRS data indicated more than 4 fold

elevation in the 2HG levels across the tumor mass when compared to the scan at 0 month (~2 mM vs ~9 mM). The patient underwent chemotherapy over the course of next 10 months and the 2HG levels were monitored with MRS. Post-treatment the clinical symptoms subsided and 2HG levels reduced to pre-progression levels (~2 mM).

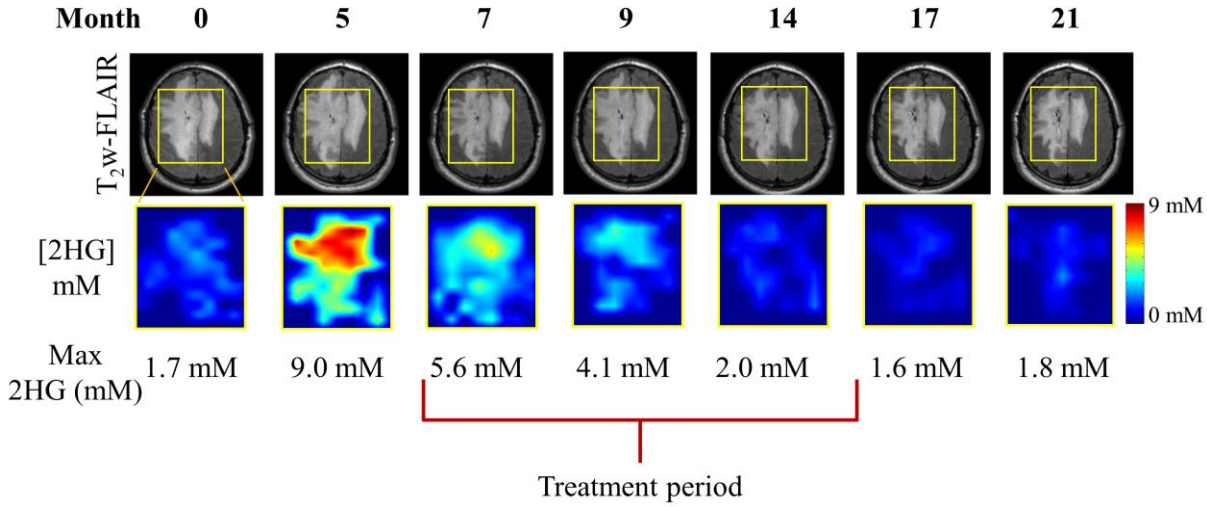

Figure 4-11 Longitudinal monitoring of a subject with oligodendroglioma.
The 2HG levels were estimated in mM over the VOI. T_2w-FLAIR did not show significant changes.

4.3.9 Three-dimensional imaging of 2HG over the tumor mass

In cases where the tumor size was large, we explored the possibility of acquiring multiple slices of SI to create 3D mapping of metabolites. Figure 4-12 shows the data from three SI slices in a subject with oligodendroglioma. 2HG levels were different across slices, with largest 2HG concentration in SI slice-3 at ~15 mM. Elevation in tCho and tNAA also varied across the three SI slices, consistent with the hyper-intensity region in T_2w-FLAIR images. In a subject with anaplastic oligodendroglioma (grade III), we acquired two SI-slices to cover the tumor region (Figure 4-13). Similar regional variation of 2HG levels was observed in the two SI-slices.

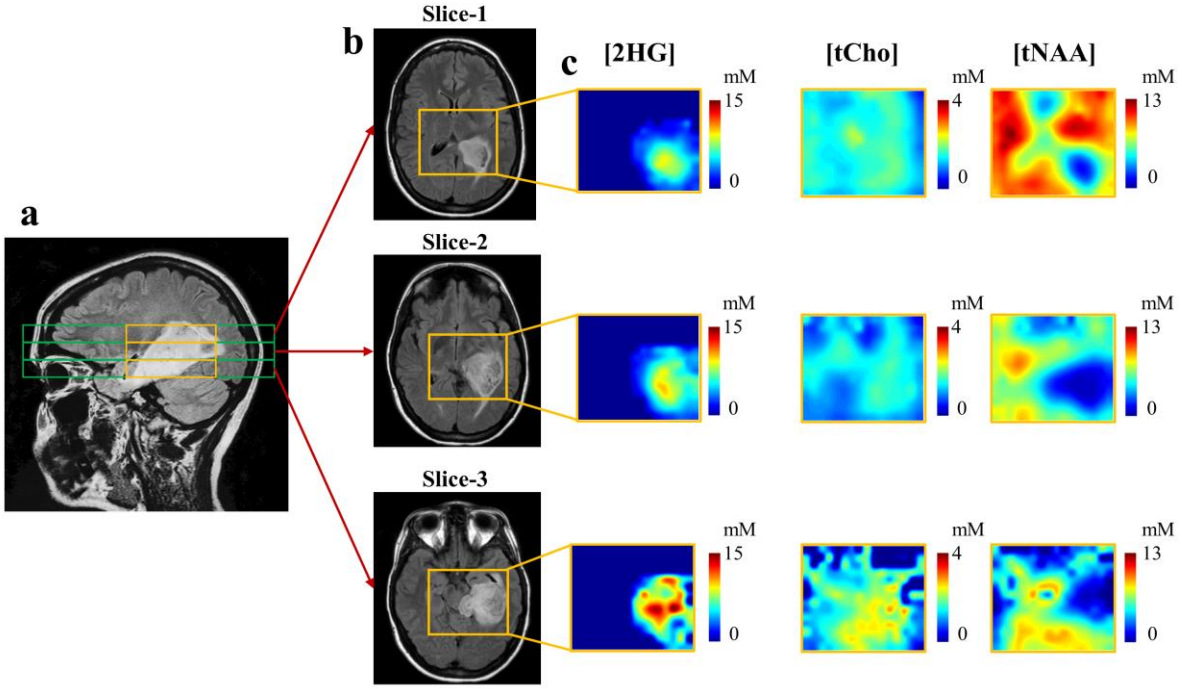

Figure 4-12 Three SI slices data from a subject with oligodendroglioma at 3T.
(**a, b**) Sagittal and axial T_2w-FLAIR images with the positions of the three SI slices. (**c**) 2HG, tCho, tNAA concentration maps over VOI in mM.

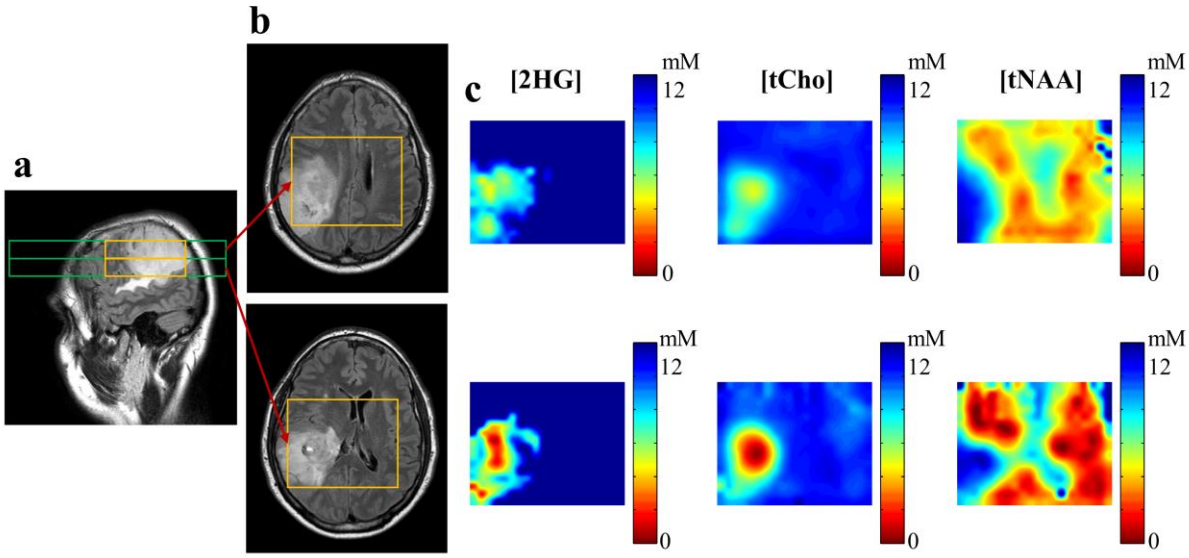

Figure 4-13 Two SI slices data from a subject with anaplastic oligodendroglioma at 3T.
(**a, b**) Sagittal and axial T_2w-FLAIR images with the positions of the two SI slices. (**c**)

Concentration maps of 2HG, tCho, tNAA (in mM).

4.3.10 *In vivo* detection of 2HG at 7T

Figure 4-14 shows spectra and metabolite maps from a WHO grade II subject at 7T. The spectra shown were selected from the region which showed hyper-intensity on T_2w-FLAIR image and contralateral normal appearing brain region. The residuals obtained using basis sets without 2HG simulated spectrum in Figure 4-14b show an inverted signal at 2.25 ppm which is not present in the residuals obtained using basis sets with 2HG simulated spectrum (Figure 4-14a). No differences were observed in other spectral regions. Spectral fitting without 2HG signal also changed the metabolite estimates of Glu and Gln (estimates in Figures 4-14a, 4-14b)). The 2HG, Glu and Gln were estimated at 4 mM, 2 mM and 5.8 mM, respectively in the tumor spectra (Figure 4-14a). GABA was not measurable in either tumor or normal brain regions. In case of the spectra from normal brain region (Figures 4-14c, 4-14d), 2HG signal was not observed in LCModel fits with and without 2HG in the basis set, whereas the Glu and Gln concentrations remained similar (6.4 mM and 1.9 mM, respectively). Figures 4-14e and 4-14f shows the concentration maps of 2HG and Glu.

4.4 DISCUSSION AND CONCLUSION

The project was aimed for spectroscopic imaging of 2HG noninvasively by optimized ^{1}H-MRS methods in subjects with gliomas. The signal overlaps of 2HG with Glu and Gln, which occur in short-echo-time standard data acquisitions, were overcome with multiplet narrowing by sequence optimization and spectral fitting with numerically simulated basis functions (30). The spectroscopic imaging was performed using phase encoding gradients

within PRESS prescribed volume (6). Several tumor with elevated 2HG were observed and the concentrations were from 2 – 15 mM.

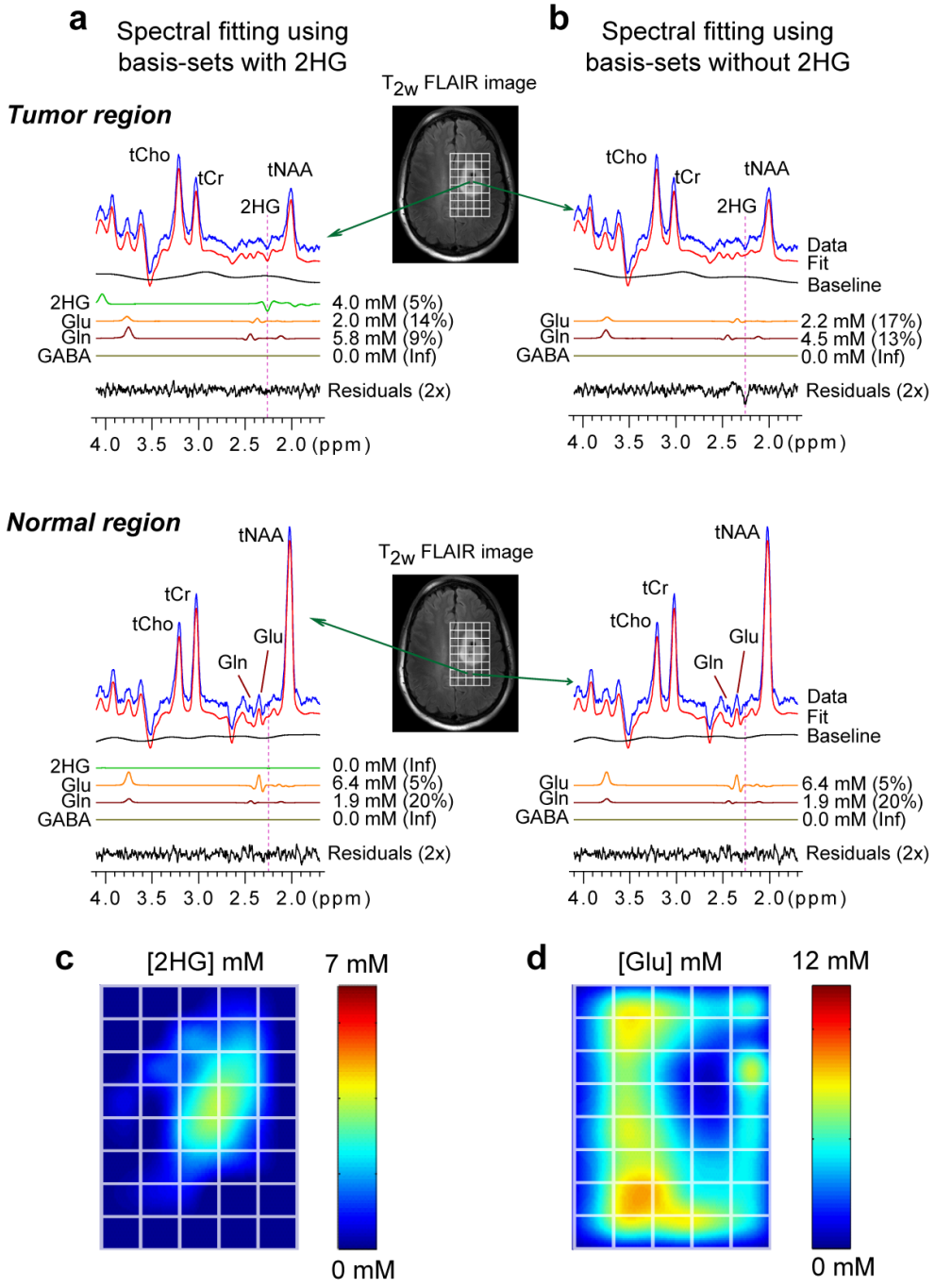

Figure 4-14 *In vivo* data from WHO grade II tumor at 7T.
(**a**, **b**) Tumor region spectra (blue), LCModel metabolite fits (red) and residuals (black) using

basis-sets with and without 2HG signal. (**c**, **d**) Normal brain region spectra (blue), LCModel metabolite fits (red) and residuals (black) using basis-sets with and without 2HG signal. 2HG, Glu, Gln and GABA estimates in mM are also shown (CRLB values in presented in parentheses). (**e**, **f**) represent the 2HG and Glu concentration maps over VOI.

The T_2s of 2HG, Gln and GABA were assumed to be identical to T_2 of Glu (180 ms) (113), and this assumption may introduce small errors their estimation. We believe that there may not be substantial differences in their T_2s when compared to Glu, as all of them exist under similar environmental conditions inside the cells. In the present study, TE of 97 ms at 3T and 78 ms at 7T are longer compared to the majority of prior MRSI (119,137-139). A recent study showed that the 2HG-optimized PRESS sequence at TE = 97 ms provides enhanced signal selectivity and specificity for 2HG when compared to standard short-TE PRESS methods at 3T (30). In addition, the T_1 saturation effects in tumors were assumed to be equal. This assumption may not be applicable in all tumors i.e. tumors with necrotic cores.

While phase encoding based spectroscopic imaging gives higher SNR, the acquisition time is longer compared to other MRSI techniques. Several methods were proposed to speed-up the MRSI acquisitions and improve the localization, such as echo-planar MR spectroscopic imaging (140-142), steady-state free precession and echo planar spectroscopic imaging (143), slice-selective FID acquisitions (144,145), editing MRSI (146), adiabatic spiral 3D MRSI (147), J-refocused coherence transfer imaging (148). The major drawbacks of these techniques are complicated data analysis, difficulty with clinical implementation, and use of vendor specific capabilities. Our current MRSI was built on commonly available PRESS localized spectroscopic imaging. The echo times of 97 and 78 ms at 3T and 7T,

respectively, can be implemented readily. The spectral fitting is simpler due to the acquisition under a dual spin echo sequence i.e. PRESS.

The ability to image 2HG, Glu and Gln in gliomas may have important applications in the diagnosis and management of gliomas (6,30,49,63,130,132,149). Mapping 2HG distribution over the tumor mass may provide a tool for monitoring IDH-mutated glioma's response to therapy (130). Currently several groups are developing and testing inhibitors for mutated IDH gliomas and have shown encouraging results in pre-clinical studies (150,151). Hence the capability to monitor the changes in 2HG levels noninvasively by means of spectroscopic imaging would help monitor the inhibiting characteristics of these drugs without the need of a biopsy. Also longitudinal monitoring of 2HG in serial measurements in patients may provide a noninvasive tool for early detection of transformation in tumor from low to high grade.

CHAPTER FIVE
Measurement of regional variation of γ-aminobutyric acid (GABA) at 7T

5.1 INTRODUCTION

5.1.1 Literature review

The *in vivo* measurement of γ-aminobutyric acid (GABA), the primary inhibitory neurotransmitter in the mammalian brain, has considerable potential for the investigation of a wide variety of neuropsychiatric disorders (4). The proton magnetic resonances of GABA are all proximate to the resonances of other abundant metabolites (82) and thus precise measurement of this low-concentration metabolite is challenging. At low or intermediate field strengths, since direct measurement of GABA is very difficult, spectral editing approaches are commonly used to detect GABA. For instance, the 3.01 ppm resonance of GABA can be edited by means of difference editing (57,152-154) and double-quantum filtering (23,155), utilizing the J coupling of the 3.01 ppm resonance to the resonance at 1.89 ppm. At high fields, spectral resolution of coupled resonances is notably improved (156) because the coupling strength which governs the overall linewidth of the multiplets is independent of field strength while the chemical shift differences (in Hz) increases with field strength. With this increase in spectral resolution and signal gain at high fields, several studies reported MRS measures of many brain metabolites, including GABA, using conventional sequence schemes with short echo times at 7T (117,157,158). Despite the presence of substantial macromolecule (MM) signals (159,160), many small signals were

well resolved with good shimming and GABA in medial occipital brain was measured with good precision in these previous studies.

GABA has six non-exchangeable protons from $^{2}CH_2$, $^{3}CH_2$, and $^{4}CH_2$ groups, which resonate at 2.284, 1.888, and 3.012 ppm respectively, with J coupling strengths of 6.4 - 8.1 Hz (154,161). While the C3- and C4-proton signals of GABA are extensively obscured by the large signals of N-acetylaspartate (NAA) and total creatine (tCr), the C2-proton resonance at 2.28 ppm is relatively distant from the neighboring resonance of glutamate (Glu) at 2.35 ppm. The GABA C2 and Glu C4 proton signals, which are 18 Hz apart from each other at 7T, are both triplets with an overall width > 14 Hz, and thus the GABA multiplet appears largely overlapped with the Glu signal in short TE spectra. Since the spectral pattern of J coupled resonances varies with inter-RF (radio frequency) pulse timings, the selectivity of the GABA signal against the Glu resonance can be improved with modification of the sequence timings, with an additional advantage that the MM signals are suppressed at long TE, as demonstrated with STEAM (stimulated echo acquisition mode) in a prior study at 3T (162).

5.1.2 Aim of the project

To measure GABA at 7T with intermediate-TE PRESS approach, to achieve good selectivity of the GABA 2.28 ppm signal against Glu. To measure the GABA concentrations in frontal and occipital brain and to evaluate the GABA levels in gray and white matter *via* linear regression analysis of the measures with respect to fractional gray matter contents.

5.2 MATERIALS AND METHODS

5.2.1 Experimental setup

MR experiments were carried out in a 7T whole-body scanner (Philips Medical Systems), equipped with quadrature birdcage RF transmission and 16-channel signal reception.

5.2.2 Numerical simulations

Numerical density-matrix simulations were carried out to optimize the subecho times of a PRESS sequence to improve the spectral resolution between the GABA 2.28 ppm and Glu 2.35 ppm resonances. 3D-volume localized spectra were calculated for various subecho times, TE_1 and TE_2, incorporating the experimental RF and gradient pulse waveforms, according to a product-operator based transformation-matrix method described in a prior study (6). The simulations were programmed with Matlab (The MathWorks, Inc.).

5.2.3 MR Spectroscopy acquisition details

Slice-selective RF pulses included an 8.8 ms 90° RF pulse (bandwidth = 4.7 kHz) and an 11.9 ms 180° RF pulse (bandwidth = 1.4 kHz) at B_1 = 15 μT. PRESS acquisition parameters included TR = 2.5 s, acquisition bandwidth = 5 kHz, and 2048 sampling points. The voxel size ranged from 10 to 15 mL. The number of signal averages (NSA) was 192 - 256, depending on the voxel size and brain regions (256 averages for the scans in left frontal and occipital regions). The carrier frequencies of the slice selective RF pulses were set to 2.5 ppm. An unsuppressed water signal was acquired from each voxel using an RF carrier at the

water resonance for residual eddy current compensation. An unsuppressed short-TE (13 ms) water signal was acquired using TR = 2.5 s from the same voxel.

5.2.4 Phantom studies

The GABA-optimized PRESS sequence was validated in a phantom solution with GABA (2 mM), Glu (20 mM) and creatine (Cr) (16 mM).

5.2.5 *In vivo* studies

In vivo single-voxel localized ^{1}H MR spectra were obtained from four brain regions in each of the 9 subjects; namely, medial prefrontal, left frontal, medial occipital and left occipital brain. The voxel size ranged from 10 to 15 mL. The number of signal averages (NSA) was 192 - 256, depending on the voxel size and brain regions (256 averages for the scans in left frontal and occipital regions). 3D sagittal T_1-weighted image was acquired with TR/TE/TI = 2500/3.7/1300 ms, flip angle = 8°, field of view = 240 × 240 mm, and 150 slices (slice thickness = 1.0 mm). Metabolite T_2 measurement was conducted for the medial occipital brain in a subject, with NSA = 32 at each of 11 TEs (75 - 275 ms; increments of 20 ms) and TR = 2.5 s.

5.2.6 Analysis and quantification of MRS data

The data from the 16 channels were combined off-line, using an in-house Matlab script which was developed according to a published algorithm (163). The combined data were then zero filled to 8192 points prior to Fourier transformation. Spectral fitting was performed with LCModel software (Ver 6.2) (86), using numerically-calculated basis spectra

of 16 metabolites; GABA, Glu, Gln, GSH, NAA, NAAG, tCr (creatine + phosphorouscreatine), tCho (glycerophosphocholine + phosphocholine), myo-inositol, glycine, taurine, scyllo-inositol, aspartate, phosphoethanolamine, ethanolamine, and lactate. Published chemical shift and J coupling constants were used for calculating the basis function; Kaiser *et al*. (154) for GABA, Choi *et al*. (33) for GSH, and Govindaraju *et al*. (82) for other metabolites. The spectral fitting was performed between 0.5 and 4.2 ppm. Cramer-Rao lower bound (CRLB), which is the measure of precision (164), computed from the Cramer-Rao Theorem that uses the diagonal elements of the least-squares variance-covariance matrix (86), was returned as a percentage standard deviation (SD) by LCModel. The fractions of gray and white matter (GM and WM) and cerebrospinal fluids (CSF) within the MRS voxels were obtained from segmentation of the T_1-weighted images using Statistical Parametric Mapping software (SPM5) (165). The tissue segmentation was undertaken incorporating the chemical shift displacement effect. A major resonance was chosen for each metabolite based on the highest signal selectivity and used to calculate the voxel displacement according to the spectral difference of the resonance from the RF carrier (2.5 ppm). The major resonance used was 2.01, 2.045, 2.28, 2.35, 2.44, 2.54, 3.03 and 3.21 for NAA, NAAG, GABA, Glu, Gln, GSH, tCr and tCho, respectively. The metabolite signal estimates from LCModel were normalized with respect to the water signal from GM and WM. Metabolite concentrations were then calculated by setting the mean value of the tCr estimates from the medial occipital brain at 8 mM (117,157). The T_2 relaxation effect on the metabolite signal was corrected using experimental T_2 values obtained within the study. To obtain the metabolite concentrations in pure GM and WM, the metabolite estimates from the

brain regions were fitted with a linear function of fractional GM matter content, f_{GM} = GM/(GM+WM). Prism 5 (GraphPad Software, Inc.) was used for the linear regression and relevant statistical analyses. Paired t-test was performed for comparison of metabolite estimates and regression outputs between brain regions. Statistical significance was declared at p value < 0.05. Data are presented in mean±SD.

5.3 RESULTS

5.3.1 Numerical simulations and phantom experiments

We performed numerical simulations and obtained a PRESS subecho time set (TE_1, TE_2) = (31, 61) ms for detection of GABA and Glu at 7T, where TE_1 and TE_2 are the subecho times of the first and second slice-selective 180° RF pulses respectively. At this PRESS TE = 92 ms, the GABA and Glu multiplets between 2.2 and 2.4 ppm were narrow and completely separated up to singlet linewidth (FWHM) of 14 Hz, as indicated by simulation results in Figure 5-1a. The overall widths of the GABA 2.28 ppm and Glu 2.35 ppm multiplets were smaller by ~2 fold compared to 90°-acquisition for potential *in vivo* singlet FWHM of 8 - 12 Hz. Of note, the multiplet widths at TE = 92 ms were comparable to singlet linewidth; for instance, for singlet FWHM of 10 Hz, the GABA and Glu multiplet widths were 10 -10.5 Hz at the level of (positive amplitude + negative amplitude)/2, whilst the GABA and Glu multiplet widths of 90°-acquisition were 18.5 - 19 Hz. Ignoring T_2 relaxation effects, the signal strengths of GABA and Glu were 72% and 58% with respect to the 90°-acquisition. As a result, when the GABA and Glu multiplets were summed for a GABA-to-Glu concentration ratio of 1:10, the GABA 2.28 ppm signal, which was not

discernible in 90°-acquisition for singlet FWHM > 8 Hz, became clearly differentiable from Glu at PRESS TE = 92 ms. For the same concentration ratio, the calculated composite signal pattern of PRESS TE = 92 ms was closely reproduced in phantom experiment (Figure 5-1b). The zero-TE calculated composite signals of GABA and Glu were very similar to phantom spectra obtained with STEAM (TE, TM) = (8, 14) ms, in which the J evolution effects may be negligible.

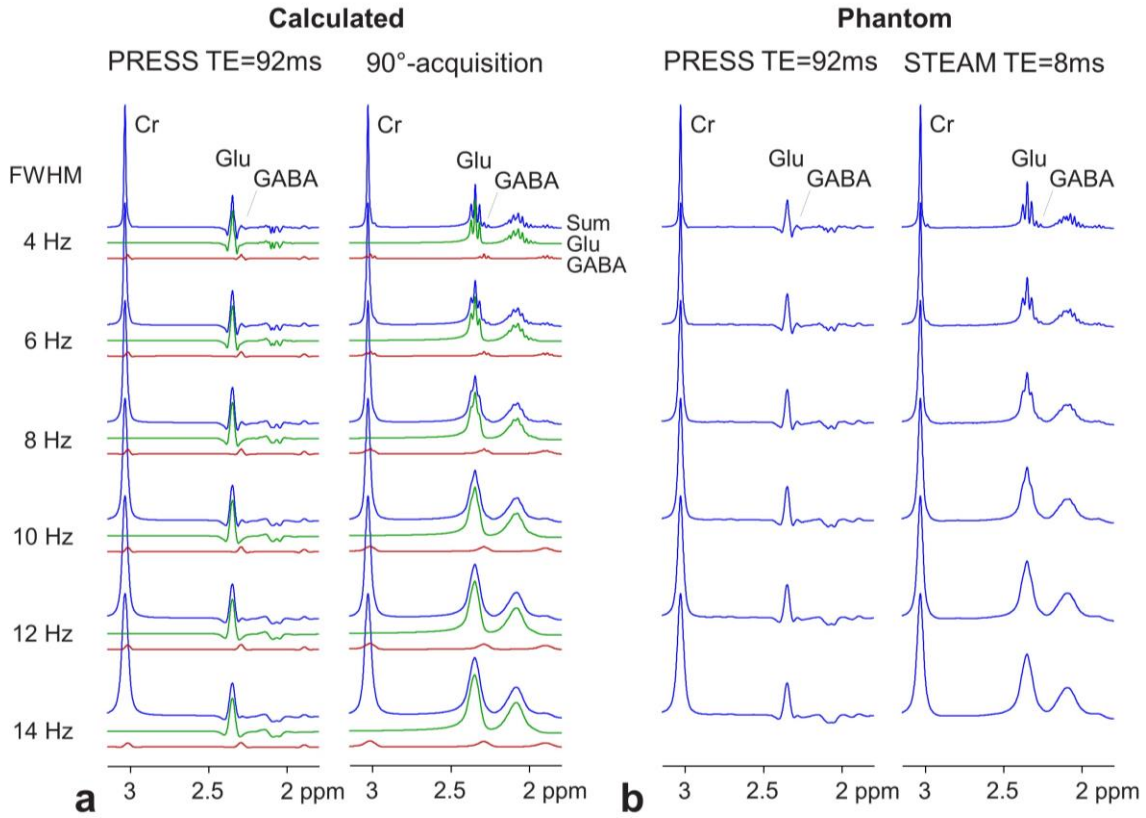

Figure 5-1 Numerically-calculated and phantom spectra at 7T.
(a) Spectra of GABA, Glu and Cr, calculated for PRESS (TE_1, TE_2) = (31, 61) ms and 90°-acquisition, are shown for singlet FWHM of 4 - 14 Hz. The concentration ratio is GABA:Glu:Cr = 1:10:8. (b) Spectra from a aqueous solution with GABA (2 mM), Glu (20 mM) and Cr (16 mM), obtained with PRESS TE = 92 ms and STEAM (TE, TM) = (8, 14) ms, are shown for singlet FWHM of 4 - 14 Hz. Spectra are normalized with respect to the Cr peak amplitude.

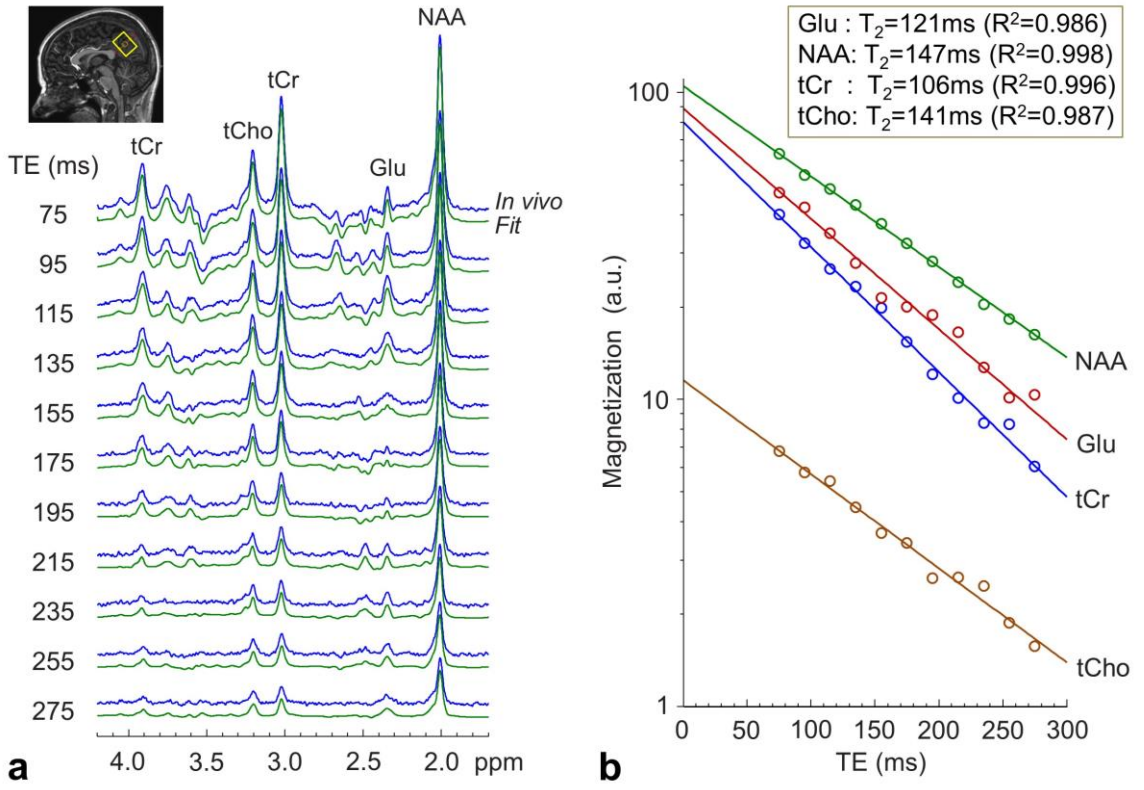

Figure 5-2 T_2 measurements for Glu, NAA, tCr and tCho at 7T *in vivo*.
(a) A stack of medial occipital brain spectra at 11 TEs are shown together with LCModel fits (voxel size = 23×23×23 mm^3; NSA = 32). (b) LCModel estimates of the metabolite signals at the eleven TEs were fitted with a mono-exponential function of TE. The estimated T_2 values and the coefficients of determination (R^2) are shown in a box.

5.3.2 T_2 relaxation measurement of Glu, NAA, tCr and tCho

T_2 relaxation times of Glu, NAA, tCr and tCho in the medial occipital brain were measured for use to correct for the transverse relaxation effects. The singlets of NAA, tCr and tCho at TE = 275 ms were 26%, 15% and 23% relative to those at TE = 75 ms, respectively (Figure 5-2a). With increasing TE, the intensity and pattern of the Glu multiplet at 2.35 ppm were both altered due to the T_2 relaxation and J coupling effects. The Glu signal was relatively well defined at TE = 75 - 115 ms and 215 - 255 ms. From mono-exponential

fitting of the LCModel estimates of the signals as a function of TE, the T_2's of Glu, NAA, tCr and tCho were estimated to be 121, 147, 106 and 141 ms, respectively. The T_2 estimates of NAA and tCr agreed well with prior measures by PRESS at 7T (75). The T_2 values of Glu, NAA, tCr and tCho were used for subsequent data analysis for metabolite quantification. The T_2's of GABA, Gln and GSH were assumed to be identical to the Glu T_2.

5.3.3 *In vivo* spectra at PRESS TE = 92 ms

Figure 5-3 presents *in vivo* spectra from the medial frontal (MF) and left frontal (LF) brain of a healthy volunteer, together with spectral analysis results. The fractional GM content was 78% and 18%, respectively. With the substantial attenuation of MM signals at TE = 92 ms, the spectra had fairly flat baselines and were well reproduced by the fit with minimal variations in residuals between 0.5 and 4.2 ppm (Figure 5-3b). As predicted by the simulation and phantom data, the GABA signal at 2.28 ppm was resolved from the large Glu 2.35 ppm peak (Figure 5-3c). The GABA signal was clearly discernible in the spectrum from the MF voxel (GM dominant), whilst the spectrum from the WM-rich, LF region showed a small signal at 2.28 ppm. The GABA concentration estimate was higher by > 2 fold in GM- than in WM-dominant regions. The GABA CRLB was 5% and 9% in spectra from GM and WM regions, respectively. The Glu signal at 2.35 ppm was also greater in GM- than in WM-dominant region. The Glu CRLB was 1 - 2% in both spectra. The spectrum from the LF showed a small Gln signal at 2.44 ppm compared to the MF spectrum. The NAAG singlet at 2.045 ppm was unequivocally discernible in the spectrum from LF,

indicating higher NAAG in WM than in GM. The 2.18 ppm multiplet of the NAAG glutamate moiety was also larger in LF than in MF.

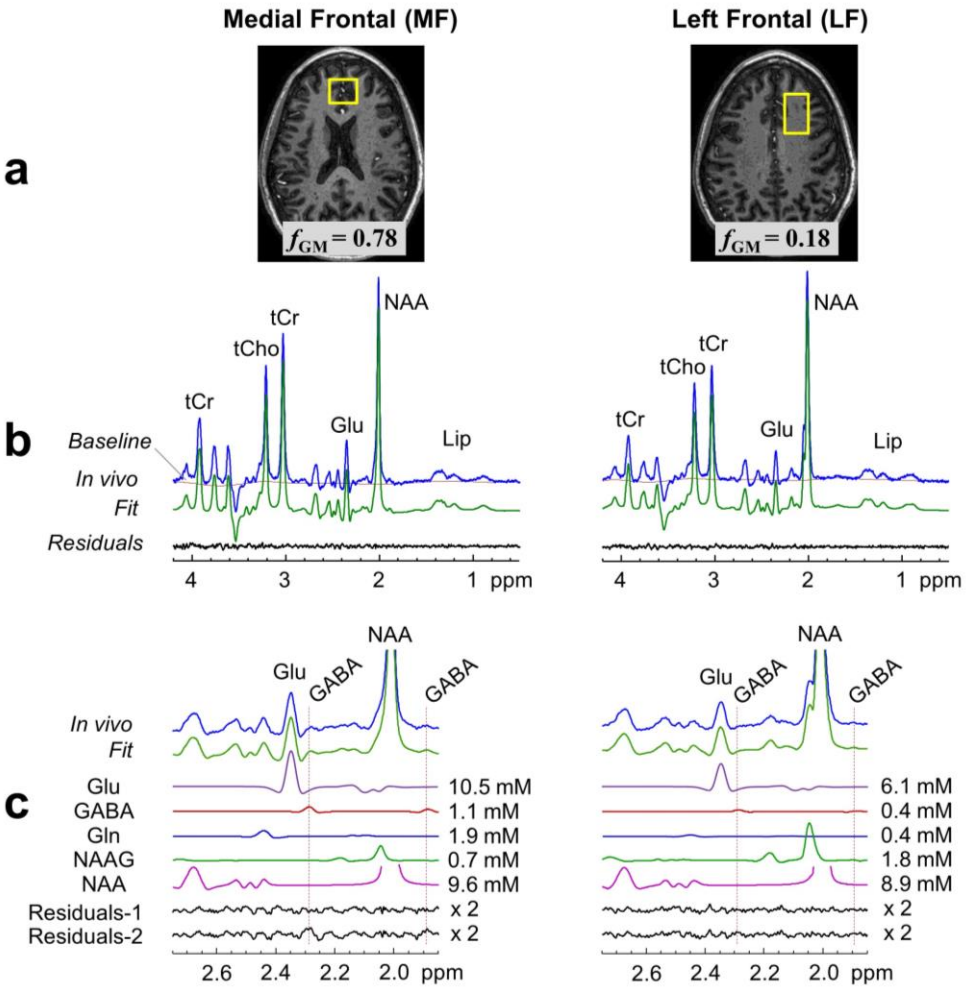

Figure 5-3 Spectral analyses of *in vivo* PRESS TE = 92 ms spectra from four two brain regions.

(a) Voxel positioning is shown in T1-weighted images, together with the fractional GM contents (fGM) within the voxels (size 20×23×23 and 35×20×15 mm3 for medial frontal and left frontal brain respectively). (b) Spectra are shown with LCModel fits, residuals and baseline between 1.8 and 4.2 ppm. Data were acquired with NSA = 128 for medial frontal and 256 for left frontal. Spectra are normalized to GM+WM water. (c) *In vivo* spectra and LCModel fits are shown between 1.85 and 2.75 ppm together with metabolite signals and concentration estimates. Residual-1 and -2 (both two-fold magnified) were obtained from spectral fittings using basis sets with and without GABA, respectively. Dotted lines are drawn at 2.28 and 1.89 ppm (GABA resonances), at which large residual signals were discernible in Residuals-2 from medial frontal.

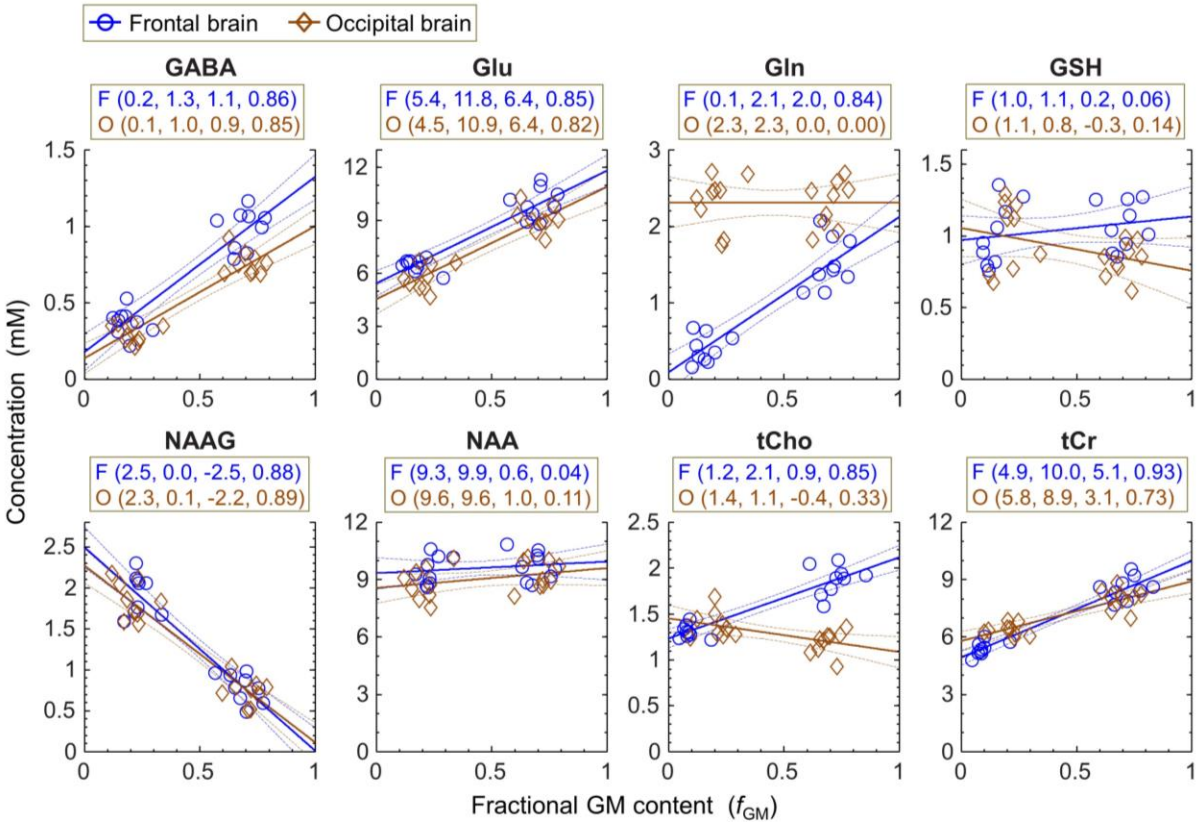

Figure 5-4 Linear regression of metabolite estimates with respect to fractional GM contents (fGM).
The regression was performed for 8 metabolites, separately for frontal brain data (18 circles in blue) and occipital brain data (18 diamonds in brown). Shown in a bracket (within a box) for frontal (F) or occipital (O) brain is, left to right, Y-axis intercepts at fGM = 0 and 1, slope, and R2 (coefficient of determination). Dashed lines indicate 95% confidence intervals of the linear fits.

For validation of GABA detection, LCModel fitting was undertaken with and without GABA in the basis set. In the spectral fitting with GABA, the *in vivo* spectra were well reproduced by the fits, leading to noise-level residuals at GABA resonances (Figure 5-3c, Residuals-1). When GABA was excluded from the basis set, large residuals at the GABA

2.28 and 1.89 ppm resonances resulted (Figure 5-3c, Residuals-2), supporting that the signals at 2.28 and 1.89 ppm in the *in vivo* spectra were primarily attributable to GABA. The residuals from without-GABA fitting were larger in spectra from GM regions than in spectra from WM regions.

The signal-to-noise ratio (SNR) and linewidth were quite similar between the 36 data sets from 9 subjects (4 voxels in each). For spectra from the MF, LF, MO (medial occipital), and LO (left occipital) regions, the mean SNR of NAA (2.01 ppm) was 304±37, 296±25, 313±36 and 302±37, and the mean linewidth of tCr (3.03 ppm) was 10.1±0.9, 9.2±0.7, 9.6±0.6 and 9.9±0.8, respectively. Here, the SNR was the ratio of the tNAA singlet amplitude with respect to the SD of the residuals between 1.7 and 3.3 ppm. As shown in Table 1, the fractional GM content was approximately 70% for the voxels in the MF and MO regions and about 20% for the voxels in the LF and LO regions.

GABA was measurable with CRLB < 16% in all 36 spectra. The concentration of GABA was estimated to be 1.0±0.1, 0.4±0.1, 0.8±0.1, and 0.3±0.1 mM for the MF, LF, MO and LO regions, respectively (Table 1). The estimate was significantly different between MF and LF and between MO and LO ($p < 2\times10–6$). Also, the GABA estimate was significantly different between MF and MO regions ($p = 9\times10–4$) while the fGM was about the same between the regions ($p = 0.5$). Linear regression of the GABA estimates with respect to fGM showed slightly stronger correlation of the concentration with fGM in frontal brain than in occipital brain (slope = 1.1 vs. 0.9), but the difference in the slopes was not significant ($p = 0.06$) (Figure 5-4). The GABA level in pure GM (i.e., Y-axis intercept at fGM = 1) was estimated to be 1.3 and 1.0 mM for frontal and occipital brain respectively, which were

significantly different from each other (p = 0.001). The GABA concentration in pure WM (i.e., Y-axis intercept at fGM = 0) was about the same between frontal and occipital brain (~0.15 mM). The ratio of the Y-axis intercepts was 7.5±2.7 and 7.5±2.9 for frontal and occipital brain, respectively. The GABA CRLB ranged from 4% to 7% in the data from the MF and MO regions, while it was relatively large (8 - 16%) in the data from the LF and LO regions.

	f_{GM} (%)				Concentration (mM)				CRLB (%)			
	MF	LF	MO	LO	MF	LF	MO	LO	MF	LF	MO	LO
GABA	69±6	18±5	70±6	21±6	1.0±0.1	0.4±0.1	0.8±0.1	0.3±0.1	5.1±0.6	9.8±2.6	5.4±0.9	12±2
Glu	69±6	17±5	70±6	21±6	9.9±0.9	6.5±0.4	9.1±0.7	5.8±0.7	1.1±0.3	1.6±0.5	1.3±0.5	1.6±0.5
Gln	70±6	17±5	70±6	21±6	1.5±0.3	0.4±0.2	2.3±0.3	2.3±0.3	4.7±1.2	17±7	3.1±0.3	2.7±0.5
GSH	70±7	16±5	70±6	21±6	1.1±0.2	1.0±0.2	0.8±0.1	1.0±0.2	5.0±0.7	4.8±0.7	6.0±0.7	4.7±0.9
NAAG	68±6	24±4	70±6	21±6	0.8±0.2	1.9±0.2	0.7±0.2	1.8±0.2	5.1±1.2	2.3±0.5	5.0±1.0	2.3±0.7
NAA	68±6	24±4	70±6	21±6	9.7±0.7	9.5±0.7	9.3±0.7	8.8±0.8	1	0.9±0.3	0.9±0.3	0.7±0.5
tCho	72±7	10±4	69±5	20±6	1.9±0.2	1.3±0.1	1.2±0.1	1.4±0.1	1	1	1	1
tCr	72±7	11±5	69±5	20±6	8.6±0.6	5.4±0.4	8* (±0.6)	6.4±0.3	1	1	0.9±0.3	0.6±0.5

Table 5-4 Fractional GM contents (f_{GM}), concentration estimates (mM), and CRLB (%) of metabolites from nine subjects.
Fractional GM contents (f_{GM}), concentration estimates (mM), and CRLB (%) are tabulated for eight metabolites for the medial frontal (MF), left frontal (LF), medial occipital (MO), and left occipital (LO) brain in nine subjects. Metabolite concentrations in the four regions were calculated with reference to the mean tCr of the MO region at 8 mM (indicated by an asterisk) following the normalization of LCModel estimates to the GM+WM water signal for individual spectra. Data are mean ± SD (n = 9).

The Glu estimate was significantly different between the MF and LF regions and between the MO and LO regions ($p < 2\times10^{-6}$) (Table 5-1). Linear regression showed that the correlation of Glu with f_{GM} was about the same between frontal and occipital brain (slope =

6.4). Glu showed significant difference between MF and MO regions and between LF and LO regions ($p < 0.02$) (Fig. 5). The Glu CRLB was ≤ 2% in all data. For Gln, the GM and WM dependence of the estimate was markedly different between frontal and occipital brain. While the mean Gln level was similar between the MO and LO regions (~2.3 mM), the data from the MF and LF regions showed drastically different Gln levels (1.5 and 0.4 mM respectively; $p = 3\times10^{-5}$), giving a correlation slope of 2.0, which was significantly different from the (essentially) zero slope in the occipital-brain data ($p = 10^{-9}$). The Gln difference between MF and LF remained significant ($p = 2.4\times10^{-4}$) following a Bonferroni correction, which was done by multiplying the uncorrected p value by the number of metabolites, 8. The Gln CRLB of the LF region was distinctly larger than those of other regions (9 - 31% *vs.* 2 - 6%). For GSH, the concentration was estimated to be more or less 1 mM in the four regions. The estimates from the MF and MO were significantly different from each other (1.1 and 0.8 mM respectively; $p = 0.01$). Linear regression analysis suggested that the GSH concentration may be higher in frontal GM than in occipital GM ($p = 0.02$). In contrast to many other metabolites, NAAG showed negative correlation with f_{GM}. The NAAG estimate was very similar between frontal and occipital brain. The mean concentration of the LF and LO regions was ~2.5 times higher than that of the MF and MO regions (1.9 *vs.* 0.8 mM). A linear regression of the entire 36 estimates of NAAG gave the ratio of the Y-axis intercepts at $f_{GM} = 0$ and 1 as 33±42. The concentration of NAA was estimated to be fairly constant between the four regions (9 - 10 mM), without an indication of significant difference between GM and WM or between frontal and occipital brain. For tCho, the concentration from the MF region was distinctly larger than those from other regions (1.9 *vs.* ~1.3 mM)

(Table 5-1). The concentration was significantly different between GM- and WM-dominant regions ($p = 6\times10^{-5}$ in frontal and 0.01 in occipital). The correlation with f_{GM} was quite different between frontal and occipital brain, the slope being positive (0.9) in frontal brain and negative (–0.4) in occipital brain, which were both significantly different from zero ($p = 4\times10^{-8}$ and 0.01 respectively). The tCr estimates from the MF, LF, MO, and LO regions were 8.6, 5.4, 8, and 6.4 mM, respectively. The tCr level was significantly different between GM- and WM-rich regions ($p < 4\times10^{-6}$). The GM tCr levels in frontal and occipital brain (10.0 and 8.9 mM respectively) were significantly different from each other ($p = 0.02$).

5.4 DISCUSSION AND CONCLUSION

Although, at 7T, short-TE MRS gives large signals with minimal T_2 signal loss, the spectral overlaps between the broad multiplets and interference of MM signals could make GABA estimation from short-TE data difficult, as in our prior study (33). Given the spectral complexities at short TEs, simplification of spectra *via* suppression of MM signals and manipulation of the J evolution at an optimized intermediate TE can provide an alternative tool for measuring small metabolite signals. The current paper reports regional variations of GABA, Glu, Gln, GSH and NAAG, together with those of NAA, tCho and tCr, using PRESS (TE_1, TE_2) = (31, 61) ms, which was tailored for improving the spectral resolution of the J coupled resonances between 2.1 and 2.6 ppm, particularly for GABA. This PRESS TE = 92 ms method gave substantial narrowing of the GABA 2.28 ppm and Glu 2.35 ppm multiplets and allowed improved differentiation of the small GABA signal from the adjacent Glu peak compared to our previously-reported TE = 100 ms method (33). The Glu signal amplitude

was slightly suppressed to increase the GABA selectivity, but this is not detrimental to Glu detection given the overall small CRLB of Glu in the present study (2% or less). In particular, acquisition of *in vivo* data that show a visually discernible GABA peak at 2.28 ppm may be a major achievement of the present study. The GABA CRLB was reduced compared to our prior study (i.e., ~5% vs. ~15% for medial frontal brain), indicating improved precision. Additionally, spectral fitting without GABA resulted in noticeable residuals at the GABA resonances, indicating good selectivity of GABA by the optimized MRS. In addition, it is noteworthy that the GABA signal strength from the PRESS TE = 92 ms method is substantially larger than the GABA 3.01 ppm signal obtainable by J difference editing. A computer simulation indicated that, for a GABA-to-Cr concentration ratio of 1:8, a GABA 2.28 ppm to Cr 3.03 ppm signal amplitude ratio is 3.7% in PRESS TE = 92 ms whereas J difference editing can give a GABA 3.01 ppm signal only up to 2% of the Cr signal depending on the slice-selective RF pulse bandwidth.

Several prior 7T MRS studies reported GABA measures together with other brain metabolites, obtained with conventional MRS sequence schemes at relatively short TEs (6 and 35 ms) (117,157,158). The tCr concentration estimates of the present study and the prior studies are similar for medial occipital brain (8 mM *vs.* 8 - 8.7 μmol/g). For this brain region, our GABA estimate is somewhat smaller than the estimates in the prior studies (0.8 mM *vs.* 1 - 1.5 μmol/g). The GABA CRLB was quite smaller in our study (5 - 6%) compared to the prior studies (7 - 15%). For Glu, our estimate of 9.1 mM agrees well with the prior studies (9 - 10 μmol/g), with mean CRLBs $\leq$ 2% in all the studies. Gln was measured at various levels (1.5 - 3 μmol/g) in the prior studies, among which our Gln

estimate of 2.3 mM is close to the measurements (2.2 - 3 μmol/g) at TE = 6 ms (117,157). Published concentrations of GSH are between 0.9 and 1.4 μmol/g while our estimation is 0.8 mM. The mean CRLBs of Gln and GSH are slightly lower in the current study (3 and 6% respectively) than in the prior studies (4 - 13%).

At 7T, while GABA may be measurable by means of uniform excitation over the entire resonances as demonstrated in the present and aforementioned prior studies (117,157,158), some studies measured GABA using spectral editing such as difference editing or polarization transfer methods (166-168), which edited the GABA 3.01 ppm C4-proton resonance utilizing its J coupling to the 1.9 ppm C3-proton resonance. A notable difference between the uniform excitation and spectral editing methods is homocarnosine contamination. Due to the close proximity of the homocarnosine C4 and C3 proton resonances to the free GABA C4 and C3 proton resonances, the homocarnosine C4 proton resonance will be fully co-edited in GABA editing and consequently the edited signal at ~3 ppm will be representative of the concentrations of GABA plus homocarnosine (assuming no other contamination). In contrast, the performance of a uniform excitation method may be largely dependent on the selectivity of the GABA 2.28 ppm C2-proton resonance. Generating a well-defined GABA 2.28 ppm signal against the neighboring abundant Glu signal would therefore be essential for reliable estimation of GABA. Since the homocarnosine 2.35 ppm C2-proton resonance (162,169) is relatively distant from the GABA C2-proton resonance, GABA estimation by uniform excitation may be quite immune to homocarnosine contamination. Interestingly, our GABA estimates of 0.8 - 1.0 mM in medial frontal and occipital brain are in good agreement with prior spectrally-edited free

GABA estimates that were obtained with a correction for homocarnosine contamination (166,169) assuming a homocarnosine-to-free GABA concentration ratio of 1/3 (170). In biopsies from frontal, temporal and cerebellar cortices of the human brain, the homocarnosine concentration was measured to be about 50% of the free GABA level (171).

GM and WM dependence of GABA was evaluated in several prior MRS studies, mostly 3T, which all performed regression analyses to obtain the GABA levels in pure GM and WM (23,155,172,173). In the current study, the GM-to-WM GABA concentration ratio was about the same between frontal and occipital brain (~7.5). This value is in good agreement with a prior measure (~8) by spectroscopy imaging, in which the GABA 3.01 ppm was measured with double-quantum editing and a nonlinear regression was undertaken on point-spread-function corrected estimates of GABA/tCr, mostly from posterior brain (155). Our estimate for occipital-GM GABA is lower by ~30% compared to this prior study (1.0 *vs.* 1.3 mM) in which homocarnosine was likely included in GABA estimates. A similar GM-to-WM GABA concentration ratio (8.7) was obtained from a linear regression in a prior single-voxel MRS study in sensorimotor cortex (173), in which the GM GABA estimate was quite large (2.8 mM). However, the GM-to-WM GABA concentration ratio from the present study is much larger than those (2 - 3) from other prior studies (23,172). For regional variations in GABA, our observation of higher GABA in MF than in MO agrees with a recent 3T study which reported GABA levels in four regions in anterior and posterior cingulate cortices (174). In this prior study, GABA was measured to be significantly higher in anterior cingulate cortex than in posterior cingulate cortex while the fractional GM content within the voxel in the anterior region was lower than that in the posterior. In contrast, GABA was

measured to be higher in posterior brain than in anterior brain in other 3T study (175). The cerebellar GABA level was measured to be lower than the anterior cingulate GABA level in another prior 3T study (176). It may be that the GABA concentration and its dependence on tissue composition vary from one anatomical location to another and the GABA measures of the current study could be specific to the locations investigated.

Several prior spectroscopic imaging and single-voxel MRS studies evaluated Glu in GM and WM with regression analyses (80,141,148,177). The GM-to-WM ratio of Glu is in good agreement between the present and prior studies (2 - 2.5) most likely because of the relatively high concentration and consequently large signal. In contrast, there is paucity in literature for regional variations in Gln and GSH, perhaps due to the presence of technical challenges in measuring these relatively low concentration metabolites. While in our study Gln was estimated to be substantially higher in GM than in WM in frontal brain and to be about the same between GM and WM in occipital brain, a prior spectroscopic imaging study at 7T (148) showed that Gln is about 2 fold higher in GM than in WM in the supplementary motor area. Compared to a single-voxel MRS study at 7T (178), which reported metabolite ratios (/tCr) from MRS voxels (~15 mL) in medial frontal and right frontal brain (without regression), the $(Gln/tCr)_{MF}$-to-$(Gln/tCr)_{LF}$ ratio of the present study (calculated from Table 1) is quite large compared to the $(Gln/tCr)_{MF}$-to-$(Gln/tCr)_{Right\text{-}Frontal}$ ratio of the prior study (2.4 *vs.* 1.3). For GSH, the GM-to-WM concentration ratio of ~1.2 (frontal brain) in the present study is slightly smaller than a value (1.5) from a prior spectroscopic imaging study (difference editing of the GSH 2.95 ppm resonance) (179), in which the GSH level was estimated to be 3.2 and 2.2 mM for GM and WM, respectively. Our observation of higher

GSH in frontal GM than in occipital GM agrees with the result from this prior study. For NAAG, our measures of the concentrations in the GM- and WM-dominant voxels (~1 and ~2 mM respectively) agree well with the reported values in prior MRS studies (91,117,180). The NAAG-to-NAA ratios in the GM and WM voxels of the present study, which were respectively ~0.1 and ~0.2 for both frontal and occipital brain, show slight discrepancy compared to some previous studies (92,179), but are in good agreement with recent 3T and 7T studies (181,182).

Several weaknesses and sources of errors may be present in the present study. First, while spectral simplification by the use of a relatively long TE (92 ms) may be beneficial, quantification of metabolite levels requires correction for T_2 relaxation effects. Since the T_2 effects in GABA, Gln and GSH were corrected using the Glu T_2 value, uncertainties may be present in the estimation of GABA, Gln and GSH, depending on the differences in their T_2's from the Glu T_2. Second, slice displacements due to the limited bandwidth of the 180° RF pulse were quite large (~10% of the slice thickness per 0.5 ppm), preventing estimation of metabolites in an identical volume. Third, although the NAA CH_2 multiplet at ~2.5 ppm was substantially suppressed with PRESS TE = 92 ms, the residual signal was not negligible compared to the C4-proton multiplets of Gln and GSH and thus could interfere with estimation of these metabolites. It appears that the NAA multiplet at ~2.5 ppm can be further suppressed by applying an additional RF pulse between the PRESS 180° pulses (178), although this may require additional echo time optimization. In the present study, a short-TE (13 ms) STEAM water signal was obtained from a single voxel and used for metabolite estimation. As shown in Table 1, the fractional GM contents within the NAA 2.01 ppm and

tCho 3.21 ppm resonance voxels in left frontal brain differed by ~7% from that of the ~2.5 ppm resonance voxel. It is expected however that, with published water concentrations in GM and WM (81% and 71% relative to the bulk water concentration respectively (183)), the GM+WM water signals from the shifted voxels may differ by ~1% from the acquired water signal. This is within the experimental errors *in vivo*. Also, errors could be introduced due to the difference in the slice profiles of the STEAM 90° and PRESS 180° RF pulses, whose ratios of the transition width to the bandwidth at half amplitude were 10% and 12% respectively. The discrepancy between the STEAM and PRESS voxel shapes was ignored in this study. Lastly, presence of potential residual MM signals near 2.28 ppm could influence estimation of GABA by the proposed method. Although the MM resonance at ~2.3 ppm may undergo very rapid T_2 relaxation (*i.e.*, ~10 fold faster compared to the Cr CH_3 resonance (184)) and consequently the signals are extensively attenuated at TE = 92 ms at 7T, precise evaluation of the MM 2.3 ppm multiplet resonance (159) would be required for ensuring GABA detection without MM interferences. However, it is likely that, given similar MM concentrations between GM and WM regions (23), the notable difference in the 2.28 ppm signal strengths in our spectra from medial frontal and left frontal voxels (see Fig. 3) may be primarily due to the regional difference in GABA, implying that our GABA estimates may not contain substantial MM contaminations.

In conclusion, we have measured GABA and other challenging metabolites in several regions in healthy human brain, using a GABA-optimized PRESS method at 7T *in vivo*. Linear regression of the GABA estimates with respect to the fractional GM content indicated that GABA is 7 - 8 fold higher in GM than in WM. The concentrations of Glu and tCr were

about 2 fold higher in GM than in WM while NAAG was notably higher in WM than in GM. The dependence of Gln and tCho on tissue composition was markedly different between frontal and occipital brain. These results suggest that evaluation of potential alterations in the metabolites in disease conditions may require comparison of the estimates from matched brain regions and/or interpretation of the metabolite measures together with the tissue contents.

APPENDIX A
Numerical quantum-mechanical simulations by the product-operator-based transformation matrix algorithm

Quantum-mechanical simulations were carried out to numerically simulate spectra of metabolites and generate modeled spectra fo LCModel spectral fitting. The time evolution of the density operator was calculated numerically incorporating the shaped 90° and 180° RF and gradient pulses. The product-operator-based transformation matrix method was employed to calculate the spectra at numerous echo times (14,31). The density matrix simulations were programmed with Matlab (The MathWorks Inc., Natick, MA, USA). Published chemical shift and coupling constants were used in the simulation (82,185,186).

The time evolution of the density operator ρ is described by the Liouville-von Neumann equation

$$\partial\rho/\partial t = -i\,[H, \rho], \qquad \text{Equation 1}$$

which has a solution

$$\rho = exp(-iHt)\,\rho_0\,exp(iHt), \qquad \text{Equation 2}$$

for a time-independent Hamiltonian H. The Hamiltonian H may include the chemical shift (CS) and scalar coupling (J) terms and the radio-frequency (RF) and gradient (G) pulse terms,

$$H = H_{CS} + H_J + H_{RF} + H_G, \qquad \text{Equation 3}$$

in the rotating frame.

For a spin system with *N* coupled protons (spin = 1/2), 4^N product operators (PO) can constitute a complete set in Liouville space (133). The density matrix ρ may be written as a linear sum of the PO terms α,

$$\rho = \sum_{i=1}^{4^N} c_i \alpha_i \quad \text{Equation 4}$$

where ρ and α are $2^N \times 2^N$ square matrices with complex entries, and the coefficient *c* is real. The density operator can be expressed as a column vector σ which is composed of the coefficients *c*,

$$\sigma = \begin{pmatrix} c_1 \\ c_2 \\ \vdots \\ c_{4^N} \end{pmatrix}. \quad \text{Equation 5}$$

The density operator evolution during an RF pulse can be put in terms of a single matrix multiplication (14),

$$\sigma' = \begin{pmatrix} c_1' \\ c_2' \\ \vdots \\ c_{4^N}' \end{pmatrix} = \begin{pmatrix} T_{1,1} & T_{1,2} & \cdots & T_{1,4^N} \\ T_{2,1} & T_{2,2} & \cdots & T_{2,4^N} \\ \vdots & \vdots & \cdots & \vdots \\ T_{4^N,1} & T_{4^N,2} & \cdots & T_{4^N,4^N} \end{pmatrix} \begin{pmatrix} c_1 \\ c_2 \\ \vdots \\ c_{4^N} \end{pmatrix} = T\,\sigma \quad \text{Equation 6}$$

where the transformation matrix *T* is a $4^N \times 4^N$ square matrix with real entries. The *T*-matrix was constructed for each spatially/spectrally-selective shaped RF pulse and used for calculating the time evolution of the density operator during the MRS sequences for each metabolite.

For a time-dependent RF pulse whose envelope consists of *n* numbers as a function of time, H_{RF} and consequently *H* may be constant during each time period Δt. The density operator following the RF pulse was calculated using a (total) time evolution operator V_{total},

$$\rho = V_{total}^{-1}\, \rho_0\, V_{total}, \qquad \text{Equation 7}$$

where

$$V_{total} = V_1 V_2 \cdots V_i \cdots V_n. \qquad \text{Equation 8}$$

The time evolution operator for the *i*-th period of the RF pulse, V_i, was obtained using

$$V_i = U\, exp(-i\, H_i^{diag}\, \Delta t)\, U^{-1}, \qquad \text{Equation 9}$$

where H_i^{diag} (= $U^{-1}H_iU$) and U are the diagonalized matrix and the unitary matrix of the Hamiltonian of the *i*-th period, H_i, respectively.

When a gradient pulse was applied during an RF pulse for slice selection, since H_G and consequently H are position dependent, the space was divided into small segments and the calculation of Eq. [7] was undertaken for individual segments, assuming uniform H_G within each segment. The simulation for slice selection was conducted on a 20 mm thick slice at the center of a 30 mm sample. The sample space was divided into 150 segments, the spatial resolution being 1% with respect to the slice thickness (*i.e.*, 0.01 = 30/150/20). The 90° and 180° slice-selective RF pulse envelopes consisted of 500 and 200 digits for RF amplitude/phase variations, respectively. With an RF carrier at 3 ppm, the slices of resonances between 1 – 5 ppm were all included within the sample dimension for both 90° and 180° RF pulses. For the 180° pulse, two density matrices were calculated with two orthogonal RF phases (*i.e.*, 0 and $\pi/2$), and the slice-localized density matrix was obtained *via* subtraction between the matrices,

$$\rho_{slice} = (\rho_{\phi=0} - \rho_{\phi=\pi/2})/2. \qquad \text{Equation 10}$$

The square matrix ρ_{slice} was then converted to a column vector σ, whose *i*-th element was calculated from

$$c_i = trace(\alpha_i \rho_{slice}), \qquad \text{Equation 11}$$

where α_i is the normalized *i*-th PO term of the spin system and $i = 1, 2, \ldots, 4^N$. A single-column matrix was calculated from each PO term as an initial density operator prior to the RF pulse, and placed in the corresponding column of the *T*-matrix. For a metabolite with n coupled spins, a $4^n \times 4^n$ transformation matrix was constructed from the 4^{5n} column vectors, each from each PO term. The *T*-matrix calculation time for the PRESS 90° RF pulse was relatively minimal (~1 min) because the calculation was to be done only for a single PO term (*i.e.*, I_z). For calculating a spectrum following a PRESS sequence

ss90 – TD_1 – ss180 – TD_2 – ss180 – TD_3 – Acquisition Equation 12

|← TE_1 →|← TE_2 →|,

the simulation began with the calculated density matrix of the slice-selective 90° pulse (ss90). The time evolution during the inter-RF pulse delay (TD_1) was calculated using

$$\rho = V^{-1} \rho_0 V, \qquad \text{Equation 13}$$

where $V = U\, exp(-i\, H^{diag}\, TD_1)\, U^{-1}$, and H^{diag} and U were formed from $H = H_{CS} + H_J$. After this, the square density ρ matrix was converted to a column matrix σ using Eq.[11] and multiplied by the ss180 *T*-matrix (Eq. [6]), giving a column matrix at the end of the ss180. This column matrix was then converted to a square matrix ρ for calculating the density operator evolution during the subsequent time delay (TD_2). The calculation of the density operator evolution was continued to obtain the density operator ρ at the end of the sequence.

The expectation values of single-quantum coherences were then extracted from the ρ, using $trace(I_{-}\rho)$, to construct a time-domain signal, which was Fourier transformed to obtain a spectrum in the frequency domain. The spoiling gradients symmetric about the PRESS 180° pulses were omitted in the simulation because the 2-step phase cycling in the *T*-matrix calculation eliminated the outer-band magnetization completely.

BIBLIOGRAPHY

1. Kreis R. Quantitative localized 1H MR spectroscopy for clinical use. Prog Nucl Magn Reson Spectrosc 1997;31(2-3):155-195.
2. Williams S. Cerebral amino acids studied by nuclear magnetic resonance spectroscopy in vivo. Prog Nucl Magn Reson Spectrosc 1999;34(3–4):301-326.
3. Howe FA, Opstad KS. ^{1}H MR spectroscopy of brain tumours and masses. NMR Biomed 2003;16(3):123-131.
4. Barker P. B., Bizzi A., DeStefano N., Gullapalli R., M. LDD. Clinical MR Spectroscopy: Techniques and Applications: Cambridge University Press; 2009.
5. Choi C, Ganji SK, DeBerardinis RJ, Dimitrov IE, Pascual JM, Bachoo R, Mickey BE, Malloy CR, Maher EA. Measurement of glycine in the human brain in vivo by ^{1}H-MRS at 3 T: application in brain tumors. Magn Reson Med 2011;66(3):609-618.
6. Choi C, Ganji SK, DeBerardinis RJ, Hatanpaa KJ, Rakheja D, Kovacs Z, Yang XL, Mashimo T, Raisanen JM, Marin-Valencia I, Pascual JM, Madden CJ, Mickey BE, Malloy CR, Bachoo RM, Maher EA. 2-hydroxyglutarate detection by magnetic resonance spectroscopy in IDH-mutated patients with gliomas. Nature medicine 2012;18(4):624-629.
7. Bottomley PA. Selective volume method for performing localized NMR spectroscopy. Google Patents; 1984.
8. Gordon R, Ordidge R. Volume selection for high resolution NMR studies. 1984.
9. Frahm J, Merboldt K-D, Hänicke W. Localized proton spectroscopy using stimulated echoes. J Magn Reson 1987;72(3):502-508.
10. Hanstock CC, Rothman DL, Prichard JW, Jue T, Shulman RG. Spatially localized 1H NMR spectra of metabolites in the human brain. Proc Natl Acad Sci USA 1988;85(6):1821-1825.
11. Webb P, Spielman D, Macovski A. A fast spectroscopic imaging method using a blipped phase encode gradient. Magn Reson Med 1989;12(3):306-315.
12. Macomber RS. A complete introduction to modern NMR spectroscopy. Nova York 1998.
13. Levitt MH. Spin dynamics: basics of nuclear magnetic resonance: John Wiley & Sons; 2008.
14. Ernst RR, Bodenhausen G, Wokaun A. Principles of nuclear magnetic resonance in one and two dimensions: Clarendon Press; 1987.
15. Abraham A. The Principles of Nuclear Magnetism, 1963, 313. Oxford University Press, London.
16. De Graaf RA. In vivo NMR spectroscopy: principles and techniques: John Wiley & Sons; 2008.
17. Bloembergen N, Purcell EM, Pound RV. Relaxation Effects in Nuclear Magnetic Resonance Absorption. Physical Review 1948;73(7):679-712.
18. Katz-Brull R, Lenkinski RE. Frame-by-frame PRESS 1H-MRS of the brain at 3 T: The effects of physiological motion. Magn Reson Med 2004;51(1):184-187.

19. Pattany PM, Massand MG, Bowen BC, Quencer RM. Quantitative Analysis of the Effects of Physiologic Brain Motion on Point-Resolved Spectroscopy. AJNR Am J Neuroradiol 2006;27(5):1070-1073.
20. Öz G, Alger JR, Barker PB, Bartha R, Bizzi A, Boesch C, Bolan PJ, Brindle KM, Cudalbu C, Dinçer A, Dydak U, Emir UE, Frahm J, González RG, Gruber S, Gruetter R, Gupta RK, Heerschap A, Henning A, Hetherington HP, Howe FA, Hüppi PS, Hurd RE, Kantarci K, Klomp DWJ, Kreis R, Kruiskamp MJ, Leach MO, Lin AP, Luijten PR, Marjańska M, Maudsley AA, Meyerhoff DJ, Mountford CE, Nelson SJ, Pamir MN, Pan JW, Peet AC, Poptani H, Posse S, Pouwels PJW, Ratai E-M, Ross BD, Scheenen TWJ, Schuster C, Smith ICP, Soher BJ, Tkáč I, Vigneron DB, Kauppinen RA. Clinical Proton MR Spectroscopy in Central Nervous System Disorders. Radiology 2014;270(3):658-679.
21. Barbin G, Pollard H, Gaïarsa JL, Ben-Ari Y. Involvement of GABAA receptors in the outgrowth of cultured hippocampal neurons. Neuroscience Letters 1993;152(1–2):150-154.
22. Cherubini E, Gaiarsa JL, Ben-Ari Y. GABA: an excitatory transmitter in early postnatal life. Trends Neurosci 1991;14(12):515-519.
23. Choi C, Bhardwaj PP, Kalra S, Casault CA, Yasmin US, Allen PS, Coupland NJ. Measurement of GABA and contaminants in gray and white matter in human brain in vivo. Magn Reson Med 2007;58(1):27-33.
24. McCormick DA. GABA as an inhibitory neurotransmitter in human cerebral cortex. J Neurophysiol 1989;62(5):1018-1027.
25. Sivilotti L, Nistri A. GABA receptor mechanisms in the central nervous system. Prog Neurobiol 1991;36(1):35-92.
26. Howe FA, Opstad KS. ^{1}H MR spectroscopy of brain tumours and masses. NMR Biomed 2003;16(3):123-131.
27. Pope W, Prins R, Albert Thomas M, Nagarajan R, Yen K, Bittinger M, Salamon N, Chou A, Yong W, Soto H, Wilson N, Driggers E, Jang H, Su S, Schenkein D, Lai A, Cloughesy T, Kornblum H, Wu H, Fantin V, Liau L. Non-invasive detection of 2-hydroxyglutarate and other metabolites in IDH1 mutant glioma patients using magnetic resonance spectroscopy. J Neurooncol 2012;107(1):197-205.
28. Choi C, Ganji SK, Madan A, Hulsey KM, An Z, Zhang S, Pinho MC, DeBerardinis RJ, Bachoo RM, Maher EA. In vivo detection of citrate in brain tumors by 1H magnetic resonance spectroscopy at 3T. Magn Reson Med 2013:72(2):316-323.
29. Maudsley AA, Govindaraju V, Young K, Aygula ZK, Pattany PM, Soher BJ, Matson GB. Numerical simulation of PRESS localized MR spectroscopy. J Magn Reson 2005;173(1):54-63.
30. Choi C, Ganji S, Hulsey K, Madan A, Kovacs Z, Dimitrov I, Zhang S, Pichumani K, Mendelsohn D, Mickey B, Malloy C, Bachoo R, DeBerardinis R, Maher E. A comparative study of short- and long-TE 1H MRS at 3 T for in vivo detection of 2-hydroxyglutarate in brain tumors. NMR Biomed 2013;26(10):1242-1250.

31. Thompson RB, Allen PS. Sources of variability in the response of coupled spins to the PRESS sequence and their potential impact on metabolite quantification. Magn Reson Med 1999;41(6):1162-1169.
32. Kim H, Thompson RB, Hanstock CC, Allen PS. Variability of metabolite yield using STEAM or PRESS sequences in vivo at 3.0 T, illustrated with myo-inositol. Magn Reson Med 2005;53(4):760-769.
33. Choi C, Dimitrov IE, Douglas D, Patel A, Kaiser LG, Amezcua CA, Maher EA. Improvement of resolution for brain coupled metabolites by optimized (1)H MRS at 7T. NMR Biomed 2010;23(9):1044-1052.
34. Legendre P. The glycinergic inhibitory synapse. Cell Mol Life Sci 2001;58(5-6):760-793.
35. Eulenburg V, Armsen W, Betz H, Gomeza J. Glycine transporters: essential regulators of neurotransmission. Trends Biochem Sci 2005;30(6):325-333.
36. Lamers Y, Williamson J, Theriaque DW, Shuster JJ, Gilbert LR, Keeling C, Stacpoole PW, Gregory JF. Production of 1-Carbon Units from Glycine Is Extensive in Healthy Men and Women. J Nutr 2009;139(4):666-671.
37. Bruhn H, Michaelis T, Merboldt KD, Hänicke W, Gyngell ML, Hamburger C, Frahm J. On the interpretation of proton NMR spectra from brain tumours in vivo and in vitro. NMR Biomed 1992;5(5):253-258.
38. Gabis L, Parton P, Roche P, Lenn N, Tudorica A, Huang W. In Vivo 1H Magnetic Resonance Spectroscopic Measurement of Brain Glycine Levels in Nonketotic Hyperglycinemia. J Neuroimaging 2001;11(2):209-211.
39. Gambarota G, Xin L, Perazzolo C, Kohler I, Mlynarik V, Gruetter R. In vivo ^{1}H NMR measurement of glycine in rat brain at 9.4 T at short echo time. Magn Reson Med 2008;60(3):727-731.
40. Gambarota G, Mekle R, Xin L, Hergt M, van der Zwaag W, Krueger G, Gruetter R. In vivo measurement of glycine with short echo-time ^{1}H MRS in human brain at 7 T. MAGMA 2009;22(1):1-4.
41. Hattingen E, Lanfermann H, Quick J, Franz K, Zanella FE, Pilatus U. ^{1}H MR spectroscopic imaging with short and long echo time to discriminate glycine in glial tumours. MAGMA 2009;22(1):33-41.
42. Davies NP, Wilson M, Natarajan K, Sun Y, MacPherson L, Brundler MA, Arvanitis TN, Grundy RG, Peet AC. Non-invasive detection of glycine as a biomarker of malignancy in childhood brain tumours using in-vivo ^{1}H MRS at 1.5 Tesla confirmed by ex-vivo high-resolution magic-angle spinning NMR. NMR Biomed 2010;23(1):80-87.
43. Righi V, Andronesi OC, Mintzopoulos D, Black PM, Tzika AA. High-resolution magic angle spinning magnetic resonance spectroscopy detects glycine as a biomarker in brain tumors. Int J Oncol 2010;36(2):301-306.
44. Banerjee A, Ganji S, Hulsey K, Dimitrov I, Maher E, Ghose S, Tamminga C, Choi C. Measurement of glycine in gray and white matter in the human brain in vivo by ^{1}H MRS at 7.0 T. Magn Reson Med 2012;68(2):325-331.

45. Maudsley AA, Gupta RK, Stoyanova R, Parra NA, Roy B, Sheriff S, Hussain N, Behari S. Mapping of Glycine Distributions in Gliomas. AJNR Am J Neuroradiol 2014.
46. Bergström J, Fürst P, Norée LO, Vinnars E. Intracellular free amino acid concentration in human muscle tissue. J Appl Physiol 1974;36(6):693-697.
47. DeBerardinis RJ, Cheng T. Q's next: the diverse functions of glutamine in metabolism, cell biology and cancer. Oncogene 2009;29(3):313-324.
48. DeBerardinis RJ, Mancuso A, Daikhin E, Nissim I, Yudkoff M, Wehrli S, Thompson CB. Beyond aerobic glycolysis: Transformed cells can engage in glutamine metabolism that exceeds the requirement for protein and nucleotide synthesis. Proc Natl Acad Sci USA 2007;104(49):19345-19350.
49. Hensley CT, Wasti AT, DeBerardinis RJ. Glutamine and cancer: cell biology, physiology, and clinical opportunities. J Clin Invest 2013;123(9):3678-3684.
50. Lunt SY, Vander Heiden MG. Aerobic Glycolysis: Meeting the Metabolic Requirements of Cell Proliferation. Annu Rev Cell Dev Biol 2011;27(1):441-464.
51. Medina M, Sánchez-Jiménez F, Márquez J, Rodríguez Quesada A, Núñez I. Relevance of glutamine metabolism to tumor cell growth. Mol Cell Biochem 1992;113(1):1-15.
52. Medina MÁ. Glutamine and Cancer. J Nutr 2001;131(9):2539S-2542S.
53. Koglin N, Mueller A, Berndt M, Schmitt-Willich H, Toschi L, Stephens AW, Gekeler V, Friebe M, Dinkelborg LM. Specific PET Imaging of xC− Transporter Activity Using a 18F-Labeled Glutamate Derivative Reveals a Dominant Pathway in Tumor Metabolism. Clinical Cancer Research 2011;17(18):6000-6011.
54. Lieberman BP, Ploessl K, Wang L, Qu W, Zha Z, Wise DR, Chodosh LA, Belka G, Thompson CB, Kung HF. PET Imaging of Glutaminolysis in Tumors by 18F-(2S,4R)4-Fluoroglutamine. J Nucl Med 2011;52(12):1947-1955.
55. Petroff OAC. Book Review: GABA and Glutamate in the Human Brain. The Neuroscientist 2002;8(6):562-573.
56. Petroff OAC, Errante LD, Rothman DL, Kim JH, Spencer Dennis D. Glutamate–glutamine Cycling in the Epileptic Human Hippocampus. Epilepsia 2002;43(7):703-710.
57. Mullins PG, McGonigle DJ, O'Gorman RL, Puts NAJ, Vidyasagar R, Evans CJ, Edden RAE. Current practice in the use of MEGA-PRESS spectroscopy for the detection of GABA. NeuroImage 2014;86(0):43-52.
58. Ting Wong CG, Bottiglieri T, Snead OC. GABA, γ-hydroxybutyric acid, and neurological disease. Annals of Neurology 2003;54(S6):S3-S12.
59. Schaller B, Rüegg SJ. Brain Tumor and Seizures: Pathophysiology and Its Implications for Treatment Revisited. Epilepsia 2003;44(9):1223-1232.
60. van Breemen MSM, Wilms EB, Vecht CJ. Epilepsy in patients with brain tumours: epidemiology, mechanisms, and management. The Lancet Neurology 2007;6(5):421-430.
61. Dang L, White DW, Gross S, Bennett BD, Bittinger MA, Driggers EM, Fantin VR, Jang HG, Jin S, Keenan MC, Marks KM, Prins RM, Ward PS, Yen KE, Liau LM, Rabinowitz JD, Cantley LC, Thompson CB, Vander Heiden MG, Su SM.

Cancer-associated IDH1 mutations produce 2-hydroxyglutarate. Nature 2009;462(7274):739-744.

62. Parsons DW, Jones S, Zhang X, Lin JC, Leary RJ, Angenendt P, Mankoo P, Carter H, Siu IM, Gallia GL, Olivi A, McLendon R, Rasheed BA, Keir S, Nikolskaya T, Nikolsky Y, Busam DA, Tekleab H, Diaz LA, Jr., Hartigan J, Smith DR, Strausberg RL, Marie SK, Shinjo SM, Yan H, Riggins GJ, Bigner DD, Karchin R, Papadopoulos N, Parmigiani G, Vogelstein B, Velculescu VE, Kinzler KW. An integrated genomic analysis of human glioblastoma multiforme. Science 2008;321(5897):1807-1812.
63. Ward PS, Cross JR, Lu C, Weigert O, Abel-Wahab O, Levine RL, Weinstock DM, Sharp KA, Thompson CB. Identification of additional IDH mutations associated with oncometabolite R(-)-2-hydroxyglutarate production. Oncogene 2012;31(19):2491-2498.
64. Yan H, Parsons DW, Jin G, McLendon R, Rasheed BA, Yuan W, Kos I, Batinic-Haberle I, Jones S, Riggins GJ, Friedman H, Friedman A, Reardon D, Herndon J, Kinzler KW, Velculescu VE, Vogelstein B, Bigner DD. IDH1 and IDH2 Mutations in Gliomas. N Engl J Med 2009;360(8):765-773.
65. Schubert F, Gallinat J, Seifert F, Rinneberg H. Glutamate concentrations in human brain using single voxel proton magnetic resonance spectroscopy at 3 Tesla. Neuroimage 2004;21(4):1762-1771.
66. Coupland NJ, Ogilvie CJ, Hegadoren KM, Seres P, Hanstock CC, Allen PS. Decreased Prefrontal Myo-Inositol in Major Depressive Disorder. Biol Psychiatry 2005;57(12):1526-1534.
67. Purdon SE, Valiakalayil A, Hanstock CC, Seres P, Tibbo P. Elevated 3T proton MRS glutamate levels associated with poor Continuous Performance Test (CPT-0X) scores and genetic risk for schizophrenia. Schizophrenia research 2008;99(1–3):218-224.
68. Frahm J, Bruhn H, Gyngell ML, Merboldt KD, Hänicke W, Sauter R. Localized proton NMR spectroscopy in different regions of the human brain in vivo. Relaxation times and concentrations of cerebral metabolites. Magn Reson Med 1989;11(1):47-63.
69. Kreis R, Ernst T, Ross BD. Development of the human brain: In vivo quantification of metabolite and water content with proton magnetic resonance spectroscopy. Magn Reson Med 1993;30(4):424-437.
70. Öngür D, Prescot AP, Jensen JE, Rouse ED, Cohen BM, Renshaw PF, Olson DP. T2 relaxation time abnormalities in bipolar disorder and schizophrenia. Magn Reson Med 2010;63(1):1-8.
71. Hetherington HP, Mason GF, Pan JW, Ponder SL, Vaughan JT, Twieg DB, Pohost GM. Evaluation of cerebral gray and white matter metabolite differences by spectroscopic imaging at 4.1T. Magn Reson Med 1994;32(5):565-571.
72. Posse S, Cuenod CA, Risinger R, Bihan DL, Balaban RS. Anomalous Transverse Relaxation in 1H Spectroscopy in Human Brain at 4 Tesla. Magn Reson Med 1995;33(2):246-252.

73. Barker PB, Hearshen DO, Boska MD. Single-voxel proton MRS of the human brain at 1.5T and 3.0T. Magn Reson Med 2001;45(5):765-769.
74. Mlynárik V, Gruber S, Moser E. Proton T1 and T2 relaxation times of human brain metabolites at 3 Tesla. NMR Biomed 2001;14(5):325-331.
75. Michaeli S, Garwood M, Zhu X-H, DelaBarre L, Andersen P, Adriany G, Merkle H, Ugurbil K, Chen W. Proton T2 relaxation study of water, N-acetylaspartate, and creatine in human brain using Hahn and Carr-Purcell spin echoes at 4T and 7T. Magn Reson Med 2002;47(4):629-633.
76. Träber F, Block W, Lamerichs R, Gieseke J, Schild HH. 1H metabolite relaxation times at 3.0 tesla: Measurements of T1 and T2 values in normal brain and determination of regional differences in transverse relaxation. J Magn Reson Imaging 2004;19(5):537-545.
77. Brief EE, Whittall KP, Li DKB, MacKay AL. Proton T2 relaxation of cerebral metabolites of normal human brain over large TE range. NMR Biomed 2005;18(1):14-18.
78. Tsai SY, Posse S, Lin YR, Ko CW, Otazo R, Chung HW, Lin FH. Fast mapping of the T2 relaxation time of cerebral metabolites using proton echo-planar spectroscopic imaging (PEPSI). Magn Reson Med 2007;57(5):859-865.
79. Zaaraoui W, Fleysher L, Fleysher R, Liu S, Soher BJ, Gonen O. Human brain-structure resolved T2 relaxation times of proton metabolites at 3 tesla. Magn Reson Med 2007;57(6):983-989.
80. Choi C, Coupland NJ, Bhardwaj PP, Kalra S, Casault CA, Reid K, Allen PS. T2 measurement and quantification of glutamate in human brain in vivo. Magn Reson Med 2006;56(5):971-977.
81. Xin L, Gambarota G, Mlynárik V, Gruetter R. Proton T2 relaxation time of J-coupled cerebral metabolites in rat brain at 9.4 T. NMR Biomed 2008;21(4):396-401.
82. Govindaraju V, Young K, Maudsley AA. Proton NMR chemical shifts and coupling constants for brain metabolites. NMR Biomed 2000;13(3):129-153.
83. Slotboom J, Mehlkopf AF, Bovee WMMJ. The Effects of Frequency-Selective RF Pulses on J-Coupled Spin-12 Systems. J Magn Reson A 1994;108(1):38-50.
84. Choi C, Dimitrov I, Douglas D, Zhao C, Hawesa H, Ghose S, Tamminga CA. In vivo detection of serine in the human brain by proton magnetic resonance spectroscopy ^{1}H-MRS at 7 Tesla. Magn Reson Med 2009;62(4):1042-1046.
85. Gruetter R. Automatic, localized in Vivo adjustment of all first-and second-order shim coils. Magn Reson Med 1993;29(6):804-811.
86. Provencher SW. Estimation of metabolite concentrations from localized in vivo proton NMR spectra. Magn Reson Med 1993;30(6):672-679.
87. Gottschalk M, Lamalle L, Segebarth C. Short-TE localised 1H MRS of the human brain at 3 T: quantification of the metabolite signals using two approaches to account for macromolecular signal contributions. NMR Biomed 2008;21(5):507-517.

88. Mullins PG, Chen H, Xu J, Caprihan A, Gasparovic C. Comparative reliability of proton spectroscopy techniques designed to improve detection of J-coupled metabolites. Magn Reson Med 2008;60(4):964-969.
89. Posse S, Cuenod CA, Le Bihan D. Human brain: proton diffusion MR spectroscopy. Radiology 1993;188(3):719-725.
90. Redpath TW, Smith FW. Use of a double inversion recovery pulse sequence to image selectively grey or white brain matter. Br J Radiol 1994;67(804):1258-1263.
91. Pouwels PJW, Frahm J. Differential distribution of NAA and NAAG in human brain as determined by quantitative localized proton MRS. NMR Biomed 1997;10(2):73-78.
92. Choi C, Ghose S, Uh J, Patel A, Dimitrov IE, Lu H, Douglas D, Ganji S. Measurement of N-acetylaspartylglutamate in the human frontal brain by 1H-MRS at 7 T. Magn Reson Med 2010;64(5):1247-1251.
93. de Graaf RA, Pan JW, Telang F, Lee J-H, Brown P, Novotny EJ, Hetherington HP, Rothman DL. Differentiation of Glucose Transport in Human Brain Gray and White Matter. J Cereb Blood Flow Metab 2001;21(5):483-492.
94. Ellegood J, Hanstock CC, Beaulieu C. Trace apparent diffusion coefficients of metabolites in human brain using diffusion weighted magnetic resonance spectroscopy. Magn Reson Med 2005;53(5):1025-1032.
95. Nicolay K, Braun KPJ, Graaf RAd, Dijkhuizen RM, Kruiskamp MJ. Diffusion NMR spectroscopy. NMR Biomed 2001;14(2):94-111.
96. Dreher W, Norris DG, Leibfritz D. Magnetization transfer affects the proton creatine/phosphocreatine signal intensity: In vivo demonstration in the rat brain. Magn Reson Med 1994;31(1):81-84.
97. Meyerhoff DJ. Proton magnetization transfer of metabolites in human brain. Magn Reson Med 1999;42(3):417-420.
98. Benarroch EE. Glycine and its synaptic interactions: Functional and clinical implications. Neurology 2011;77(7):677-683.
99. Eulenburg V, Armsen W, Betz H, Gomeza J. Glycine transporters: essential regulators of neurotransmission. Trends Biochem Sci 2005;30(6):325-333.
100. Davies NP, Wilson M, Natarajan K, Sun Y, MacPherson L, Brundler MA, Arvanitis TN, Grundy RG, Peet AC. Non-invasive detection of glycine as a biomarker of malignancy in childhood brain tumours using in-vivo ^{1}H MRS at 1.5 tesla confirmed by ex-vivo high-resolution magic-angle spinning NMR. NMR Biomed 2010;23(1):80-87.
101. Kinoshita Y, Yokota A. Absolute concentrations of metabolites in human brain tumors using in vitro proton magnetic resonance spectroscopy. NMR Biomed 1997;10(1):2-12.
102. Lehnhardt F-G, Bock C, Röhn G, Ernestus R-I, Hoehn M. Metabolic differences between primary and recurrent human brain tumors: a ^{1}H NMR spectroscopic investigation. NMR Biomed 2005;18(6):371-382.
103. Jain M, Nilsson R, Sharma S, Madhusudhan N, Kitami T, Souza AL, Kafri R, Kirschner MW, Clish CB, Mootha VK. Metabolite Profiling Identifies a Key Role

for Glycine in Rapid Cancer Cell Proliferation. Science 2012;336(6084):1040-1044.
104. Howe FA, Barton SJ, Cudlip SA, Stubbs M, Saunders DE, Murphy M, Wilkins P, Opstad KS, Doyle VL, McLean MA, Bell BA, Griffiths JR. Metabolic profiles of human brain tumors using quantitative in vivo ^{1}H magnetic resonance spectroscopy. Magn Reson Med 2003;49(2):223-232.
105. Kuesel AC, Donnelly SM, Halliday W, Sutherland GR, Smith ICP. Mobile lipids and metabolic heterogeneity of brain tumours as detectable by Ex Vivo ^{1}H MR spectroscopy. NMR Biomed 1994;7(4):172-180.
106. Ott D, Hennig J, Ernst T. Human brain tumors: assessment with in vivo proton MR spectroscopy. Radiology 1993;186(3):745-752.
107. Prescot AP, de BFB, Wang L, Brown J, Jensen JE, Kaufman MJ, Renshaw PF. In vivo detection of brain glycine with echo-time-averaged (1)H magnetic resonance spectroscopy at 4.0 T. Magn Reson Med 2006;55(3):681-686.
108. Choi C, Douglas D, Hawesa H, Jindal A, Storey C, Dimitrov I. Measurement of glycine in human prefrontal brain by point-resolved spectroscopy at 7.0 tesla in vivo. Magn Reson Med 2009;62(5):1305-1310.
109. Maudsley AA, Matson GB, Hugg JW, Weiner MW. Reduced phase encoding in spectroscopic imaging. Magn Reson Med 1994;31(6):645-651.
110. Ogg RJ, Kingsley RB, Taylor JS. WET, a T1- and B1-Insensitive Water-Suppression Method for in Vivo Localized ^{1}H NMR Spectroscopy. J Magn Reson B 1994;104(1):1-10.
111. Naressi A, Couturier C, Devos J, Janssen M, Mangeat C, Beer R, Graveron-Demilly D. Java-based graphical user interface for the MRUI quantitation package. MAGMA 2001;12(2):141-152.
112. Provencher SW. Automatic quantitation of localized in vivo ^{1}H spectra with LCModel. NMR Biomed 2001;14(4):260-264.
113. Ganji SK, Banerjee A, Patel AM, Zhao YD, Dimitrov IE, Browning JD, Sherwood Brown E, Maher EA, Choi C. T2 measurement of J-coupled metabolites in the human brain at 3T. NMR Biomed 2012;25(4):523-529.
114. Ganji SK, An Z, Banerjee A, Madan A, Hulsey KM, Choi C. Measurement of regional variation of GABA in the human brain by optimized point-resolved spectroscopy at 7 T in vivo. NMR Biomed 2014;27(10):1167-1175.
115. Natt O, Bezkorovaynyy V, Michaelis T, Frahm J. Use of phased array coils for a determination of absolute metabolite concentrations. Magn Reson Med 2005;53(1):3-8.
116. Schuff N, Ezekiel F, Gamst AC, Amend DL, Capizzano AA, Maudsley AA, Weiner MW. Region and tissue differences of metabolites in normally aged brain using multislice 1H magnetic resonance spectroscopic imaging. Magn Reson Med 2001;45(5):899-907.
117. Tkáč I, Öz G, Adriany G, Uğurbil K, Gruetter R. In vivo 1H NMR spectroscopy of the human brain at high magnetic fields: Metabolite quantification at 4T vs. 7T. Magn Reson Med 2009;62(4):868-879.

118. Wiebenga OT, Klauser AM, Nagtegaal GJA, Schoonheim MM, Barkhof F, Geurts JJG, Pouwels PJW. Longitudinal absolute metabolite quantification of white and gray matter regions in healthy controls using proton MR spectroscopic imaging. NMR Biomed 2014;27(3):304-311.
119. McLean MA, Woermann FG, Barker GJ, Duncan JS. Quantitative analysis of short echo time ^{1}H-MRSI of cerebral gray and white matter. Magn Reson Med 2000;44(3):401-411.
120. Bonekamp D, Smith MA, Zhu H, Barker PB. Quantitative SENSE-MRSI of the human brain. Magn Reson Imaging 2010;28(3):305-313.
121. Dydak U, Weiger M, Pruessmann KP, Meier D, Boesiger P. Sensitivity-encoded spectroscopic imaging. Magn Reson Med 2001;46(4):713-722.
122. Pan JW, Hetherington HP, Vaughan JT, Mitchell G, Pohost GM, Whitaker JN. Evaluation of multiple sclerosis by ^{1}H spectroscopic imaging at 4.1 T. Magn Reson Med 1996;36(1):72-77.
123. Posse S, Otazo R, Caprihan A, Bustillo J, Chen H, Henry PG, Marjanska M, Gasparovic C, Zuo C, Magnotta V, Mueller B, Mullins P, Renshaw P, Ugurbil K, Lim KO, Alger JR. Proton echo-planar spectroscopic imaging of J-coupled resonances in human brain at 3 and 4 Tesla. Magn Reson Med 2007;58(2):236-244.
124. Cao P, Wu EX. Accelerating phase-encoded proton MR spectroscopic imaging by compressed sensing. J Magn Reson 2014:n/a-n/a.
125. Geethanath S, Baek H-M, Ganji SK, Ding Y, Maher EA, Sims RD, Choi C, Lewis MA, Kodibagkar VD. Compressive Sensing Could Accelerate ^{1}H MR Metabolic Imaging in the Clinic. Radiology 2012;262(3):985-994.
126. Hanahan D, Weinberg Robert A. Hallmarks of Cancer: The Next Generation. Cell 2011;144(5):646-674.
127. Nikiforov MA, Chandriani S, O'Connell B, Petrenko O, Kotenko I, Beavis A, Sedivy JM, Cole MD. A Functional Screen for Myc-Responsive Genes Reveals Serine Hydroxymethyltransferase, a Major Source of the One-Carbon Unit for Cell Metabolism. Mol Cell Biol 2002;22(16):5793-5800.
128. Kohler BA, Ward E, McCarthy BJ, Schymura MJ, Ries LAG, Eheman C, Jemal A, Anderson RN, Ajani UA, Edwards BK. Annual Report to the Nation on the Status of Cancer, 1975–2007, Featuring Tumors of the Brain and Other Nervous System. J Natl Cancer Inst 2011;103(9):714-736.
129. Louis D, Ohgaki H, Wiestler O, Cavenee W, Burger P, Jouvet A, Scheithauer B, Kleihues P. The 2007 WHO Classification of Tumours of the Central Nervous System. Acta Neuropathologica 2007;114(2):97-109.
130. Schiff D, Purow B. Neuro-oncology: Five new things. Neurology Clinical practice 2013;3(4):326-333.
131. Jin G, Reitman ZJ, Duncan CG, Spasojevic I, Gooden DM, Rasheed BA, Yang R, Lopez GY, He Y, McLendon RE, Bigner DD, Yan H. Disruption of Wild-Type IDH1 Suppresses D-2-Hydroxyglutarate Production in IDH1-Mutated Gliomas. Cancer Research 2013;73(2):496-501.

132. Andronesi OC, Kim GS, Gerstner E, Batchelor T, Tzika AA, Fantin VR, Vander Heiden MG, Sorensen AG. Detection of 2-Hydroxyglutarate in IDH-Mutated Glioma Patients by In Vivo Spectral-Editing and 2D Correlation Magnetic Resonance Spectroscopy. Sci Transl Med 2012;4(116):116ra114.
133. Sørensen OW, Eich GW, Levitt MH, Bodenhausen G, Ernst RR. Product operator formalism for the description of NMR pulse experiments. Prog Nucl Magn Reson Spectrosc 1984;16(0):163-192.
134. Shrout PE, Fleiss JL. Intraclass correlations: uses in assessing rater reliability. Psychol Bull 1979;86(2):420.
135. Tedeschi G, Bertolino A, Campbell G, Barnett AS, Duyn JH, Jacob PK, Moonen CT, Alger JR, Di Chiro G. Reproducibility of proton MR spectroscopic imaging findings. AJNR Am J Neuroradiol 1996;17(10):1871-1879.
136. Gasparovic C, Bedrick EJ, Mayer AR, Yeo RA, Chen H, Damaraju E, Calhoun VD, Jung RE. Test-retest reliability and reproducibility of short-echo-time spectroscopic imaging of human brain at 3T. Magn Reson Imaging 2011;66(2):324-332.
137. Soher BJ, Vermathen P, Schuff N, Wiedermann D, Meyerhoff DJ, Weiner MW, Maudsley AA. Short TE in vivo ^{1}H MR spectroscopic imaging at 1.5 T: acquisition and automated spectral analysis. Magn Reson Imaging 2000;18(9):1159-1165.
138. Weis J, Ring P, Olofsson T, Ortiz-Nieto F, Wikstrom J. Short echo time MR spectroscopy of brain tumors: grading of cerebral gliomas by correlation analysis of normalized spectral amplitudes. J Magn Reson Imaging 2010;31(1):39-45.
139. Wijtenburg SA, Knight-Scott J. Very short echo time improves the precision of glutamate detection at 3T in 1H magnetic resonance spectroscopy. J Magn Reson Imaging 2011;34(3):645-652.
140. Posse S, DeCarli C, Le Bihan D. Three-dimensional echo-planar MR spectroscopic imaging at short echo times in the human brain. Radiology 1994;192(3):733-738.
141. Posse S, Otazo R, Caprihan A, Bustillo J, Chen H, Henry P-G, Marjanska M, Gasparovic C, Zuo C, Magnotta V, Mueller B, Mullins P, Renshaw P, Ugurbil K, Lim KO, Alger JR. Proton echo-planar spectroscopic imaging of J-coupled resonances in human brain at 3 and 4 Tesla. Magn Reson Med 2007;58(2):236-244.
142. Otazo R, Tsai SY, Lin FH, Posse S. Accelerated short-TE 3D proton echo-planar spectroscopic imaging using 2D-SENSE with a 32-channel array coil. Magn Reson Med 2007;58(6):1107-1116.
143. Dreher W, Erhard P, Leibfritz D. Fast three-dimensional proton spectroscopic imaging of the human brain at 3 T by combining spectroscopic missing pulse steady-state free precession and echo planar spectroscopic imaging. Magn Reson Med 2011;66(6):1518-1525.
144. Henning A, Schär M, Schulte RF, Wilm B, Pruessmann KP, Boesiger P. SELOVS: Brain MRSI localization based on highly selective T1- and B1-

insensitive outer-volume suppression at 3T. Magn Reson Imaging 2008;59(1):40-51.
145. Henning A, Fuchs A, Murdoch JB, Boesiger P. Slice-selective FID acquisition, localized by outer volume suppression (FIDLOVS) for 1H-MRSI of the human brain at 7 T with minimal signal loss. NMR Biomed 2009;22(7):683-696.
146. Zhu H, Edden RAE, Ouwerkerk R, Barker PB. High resolution spectroscopic imaging of GABA at 3 Tesla. Magn Reson Med 2011;65(3):603-609.
147. Andronesi OC, Gagoski BA, Sorensen AG. Neurologic 3D MR Spectroscopic Imaging with Low-Power Adiabatic Pulses and Fast Spiral Acquisition. Radiology 2012;262(2):647-661.
148. Pan JW, Avdievich N, Hetherington HP. J-refocused coherence transfer spectroscopic imaging at 7 T in human brain. Magn Reson Med 2010;64(5):1237-1246.
149. Elkhaled A, Jalbert LE, Phillips JJ, Yoshihara HAI, Parvataneni R, Srinivasan R, Bourne G, Berger MS, Chang SM, Cha S, Nelson SJ. Magnetic Resonance of 2-Hydroxyglutarate in IDH1-Mutated Low-Grade Gliomas. Sci Transl Med 2012;4(116):116ra115.
150. Rohle D, Popovici-Muller J, Palaskas N, Turcan S, Grommes C, Campos C, Tsoi J, Clark O, Oldrini B, Komisopoulou E, Kunii K, Pedraza A, Schalm S, Silverman L, Miller A, Wang F, Yang H, Chen Y, Kernytsky A, Rosenblum MK, Liu W, Biller SA, Su SM, Brennan CW, Chan TA, Graeber TG, Yen KE, Mellinghoff IK. An Inhibitor of Mutant IDH1 Delays Growth and Promotes Differentiation of Glioma Cells. Science 2013;340(6132):626-630.
151. Wang F, Travins J, DeLaBarre B, Penard-Lacronique V, Schalm S, Hansen E, Straley K, Kernytsky A, Liu W, Gliser C, Yang H, Gross S, Artin E, Saada V, Mylonas E, Quivoron C, Popovici-Muller J, Saunders JO, Salituro FG, Yan S, Murray S, Wei W, Gao Y, Dang L, Dorsch M, Agresta S, Schenkein DP, Biller SA, Su SM, de Botton S, Yen KE. Targeted Inhibition of Mutant IDH2 in Leukemia Cells Induces Cellular Differentiation. Science 2013;340(6132):622-626.
152. Rothman DL, Petroff OA, Behar KL, Mattson RH. Localized 1H NMR measurements of gamma-aminobutyric acid in human brain in vivo. Proc Natl Acad Sci USA 1993;90(12):5662-5666.
153. Mescher M, Merkle H, Kirsch J, Garwood M, Gruetter R. Simultaneous in vivo spectral editing and water suppression. NMR Biomed 1998;11(6):266-272.
154. Kaiser LG, Young K, Meyerhoff DJ, Mueller SG, Matson GB. A detailed analysis of localized J-difference GABA editing: theoretical and experimental study at 4 T. NMR Biomed 2008;21(1):22-32.
155. Choi I-Y, Lee S-P, Merkle H, Shen J. In vivo detection of gray and white matter differences in GABA concentration in the human brain. Neuroimage 2006;33(1):85-93.
156. Tkáč I, Andersen P, Adriany G, Merkle H, Uğurbil K, Gruetter R. In vivo 1H NMR spectroscopy of the human brain at 7 T. Magn Reson Med 2001;46(3):451-456.

157. Mekle R, Mlynárik V, Gambarota G, Hergt M, Krueger G, Gruetter R. MR spectroscopy of the human brain with enhanced signal intensity at ultrashort echo times on a clinical platform at 3T and 7T. Magn Reson Med 2009;61(6):1279-1285.
158. Marjańska M, Auerbach EJ, Valabrègue R, Van de Moortele P-F, Adriany G, Garwood M. Localized 1H NMR spectroscopy in different regions of human brain in vivo at 7 T: T2 relaxation times and concentrations of cerebral metabolites. NMR Biomed 2012;25(2):332-339.
159. Behar KL, Rothman DL, Spencer DD, Petroff OAC. Analysis of macromolecule resonances in 1H NMR spectra of human brain. Magn Reson Med 1994;32(3):294-302.
160. Seeger U, Mader I, Nägele T, Grodd W, Lutz O, Klose U. Reliable detection of macromolecules in single-volume 1H NMR spectra of the human brain. Magn Reson Med 2001;45(6):948-954.
161. Kreis R, Bolliger CS. The need for updates of spin system parameters, illustrated for the case of γ-aminobutyric acid. NMR Biomed 2012;25(12):1401-1403.
162. Hanstock CC, Coupland NJ, Allen PS. GABA X2 multiplet measured pre- and post-administration of vigabatrin in human brain. Magn Reson Med 2002;48(4):617-623.
163. Hall EL, Stephenson MC, Price D, Morris PG. Methodology for improved detection of low concentration metabolites in MRS: Optimised combination of signals from multi-element coil arrays. NeuroImage 2014;86(0):35-42.
164. Pfeuffer J, Tkáč I, Provencher SW, Gruetter R. Toward an in Vivo Neurochemical Profile: Quantification of 18 Metabolites in Short-Echo-Time ^{1}H NMR Spectra of the Rat Brain. J Magn Reson 1999;141(1):104-120.
165. Friston K, Ashburner J, Kiebel S, Nichols T, Penny W. Statistical parametric mapping: the analysis of functional brain images. 2007. London: Academic vii;647.
166. Terpstra M, Ugurbil K, Gruetter R. Direct in vivo measurement of human cerebral GABA concentration using MEGA-editing at 7 Tesla. Magn Reson Med 2002;47(5):1009-1012.
167. Andreychenko A, Boer VO, Arteaga de Castro CS, Luijten PR, Klomp DWJ. Efficient spectral editing at 7 T: GABA detection with MEGA-sLASER. Magn Reson Med 2012;68(4):1018-1025.
168. Pan JW, Duckrow RB, Spencer DD, Avdievich NI, Hetherington HP. Selective homonuclear polarization transfer for spectroscopic imaging of GABA at 7T. Magn Reson Med 2013;69(2):310-316.
169. Choi C, Coupland NJ, Hanstock CC, Ogilvie CJ, Higgins ACM, Gheorghiu D, Allen PS. Brain gamma-aminobutyric acid measurement by proton double-quantum filtering with selective *J* rewinding. Magn Reson Med 2005;54(2):272-279.
170. Petroff OAC, Hyder F, Mattson RH, Rothman DL. Topiramate increases brain GABA, homocarnosine, and pyrrolidinone in patients with epilepsy. Neurology 1999;52(3):473.

171. A. L. Handbook of Neurochemistry: Volume 1. Chemical and Cellular Architecture. A. L, editor: Plenum Press; 1982.
172. Jensen JE, deB. Frederick B, Renshaw PF. Grey and white matter GABA level differences in the human brain using two-dimensional, J-resolved spectroscopic imaging. NMR Biomed 2005;18(8):570-576.
173. Bhattacharyya PK, Phillips MD, Stone LA, Lowe MJ. In vivo magnetic resonance spectroscopy measurement of gray-matter and white-matter gamma-aminobutyric acid concentration in sensorimotor cortex using a motion-controlled MEGA point-resolved spectroscopy sequence. Magn Reson Imaging 2011;29(3):374-379.
174. Dou W, Palomero-Gallagher N, van Tol M-J, Kaufmann J, Zhong K, Bernstein H-G, Heinze H-J, Speck O, Walter M. Systematic Regional Variations of GABA, Glutamine, and Glutamate Concentrations Follow Receptor Fingerprints of Human Cingulate Cortex. J Neurosci 2013;33(31):12698-12704.
175. Veen JWvd, Shen J. Regional difference in GABA levels between medial prefrontal and occipital cortices. J Magn Reson Imaging 2013;38(3):745-750.
176. Waddell KW, Zanjanipour P, Pradhan S, Xu L, Welch EB, Joers JM, Martin PR, Avison MJ, Gore JC. Anterior cingulate and cerebellar GABA and Glu correlations measured by 1H J-difference spectroscopy. Magn Reson Imaging 2011;29(1):19-24.
177. Srinivasan R, Cunningham C, Chen A, Vigneron D, Hurd R, Nelson S, Pelletier D. TE-averaged two-dimensional proton spectroscopic imaging of glutamate at 3 T. Neuroimage 2006;30(4):1171-1178.
178. An L, Li S, Murdoch JB, J S. Detection of glutamate and glutamine by RF suppression and TE optimization at 7T. Proceedings of the 21st Annual Meeting ISMRMSalt Lake City, USA 2013; 3984.
179. Srinivasan R, Ratiney H, Hammond-Rosenbluth KE, Pelletier D, Nelson SJ. MR spectroscopic imaging of glutathione in the white and gray matter at 7 T with an application to multiple sclerosis. Magn Reson Imaging 2010;28(2):163-170.
180. Edden RAE, Pomper MG, Barker PB. In vivo differentiation of N-acetyl aspartyl glutamate from N-acetyl aspartate at 3 Tesla. Magn Reson Med 2007;57(6):977-982.
181. Zhang Y, Li S, Marenco S, Shen J. Quantitative measurement of N-acetyl-aspartyl-glutamate at 3 T using TE-averaged PRESS spectroscopy and regularized lineshape deconvolution. Magn Reson Med 2011;66(2):307-313.
182. An L, Li S, Wood ET, Reich DS, Shen J. N-acetyl-aspartyl-glutamate detection in the human brain at 7 Tesla by echo time optimization and improved Wiener filtering. Magn Reson Med 2014;72(4):903-912.
183. NORTON WT, PODUSLO SE, SUZUKI K. Subacute Sclerosing Leukoencephalitis: II. Chemical Studies Including Abnormal Myelin and An Abnormal Ganglioside Pattern. J Neuropathol Exp Neurol 1966;25(4):582-597.
184. Soher BJ, Pattany PM, Matson GB, Maudsley AA. Observation of coupled 1H metabolite resonances at long TE. Magn Reson Med 2005;53(6):1283-1287.
185. Bal D, Gryff-Keller A. 1H and 13C NMR study of 2-hydroxyglutaric acid and its lactone. Magn Reson Chem 2002;40(8):533-536.

186. Fan TWM. Metabolite profiling by one- and two-dimensional NMR analysis of complex mixtures. Prog Nucl Magn Reson Spectrosc 1996;28(2):161-219.